




2020

INVESTIGATION OF HOST NANOTUBE PARAMETERS FOR ENHANCING THE PERFORMANCE OF NANOSTRUCTURED CDS- CDTE SOLAR CELLS

Deepak Kumar

University of Kentucky, kr89.deepak@gmail.com

Author ORCID Identifier:

 <https://orcid.org/0000-0001-9801-8820>

Digital Object Identifier: <https://doi.org/10.13023/etd.2020.150>

[Right click to open a feedback form in a new tab to let us know how this document benefits you.](#)

Recommended Citation

Kumar, Deepak, "INVESTIGATION OF HOST NANOTUBE PARAMETERS FOR ENHANCING THE PERFORMANCE OF NANOSTRUCTURED CDS-CDTE SOLAR CELLS" (2020). *Theses and Dissertations--Electrical and Computer Engineering*. 150.
https://uknowledge.uky.edu/ece_etds/150

This Master's Thesis is brought to you for free and open access by the Electrical and Computer Engineering at UKnowledge. It has been accepted for inclusion in Theses and Dissertations--Electrical and Computer Engineering by an authorized administrator of UKnowledge. For more information, please contact UKnowledge@lsv.uky.edu.

STUDENT AGREEMENT:

I represent that my thesis or dissertation and abstract are my original work. Proper attribution has been given to all outside sources. I understand that I am solely responsible for obtaining any needed copyright permissions. I have obtained needed written permission statement(s) from the owner(s) of each third-party copyrighted matter to be included in my work, allowing electronic distribution (if such use is not permitted by the fair use doctrine) which will be submitted to UKnowledge as Additional File.

I hereby grant to The University of Kentucky and its agents the irrevocable, non-exclusive, and royalty-free license to archive and make accessible my work in whole or in part in all forms of media, now or hereafter known. I agree that the document mentioned above may be made available immediately for worldwide access unless an embargo applies.

I retain all other ownership rights to the copyright of my work. I also retain the right to use in future works (such as articles or books) all or part of my work. I understand that I am free to register the copyright to my work.

REVIEW, APPROVAL AND ACCEPTANCE

The document mentioned above has been reviewed and accepted by the student's advisor, on behalf of the advisory committee, and by the Director of Graduate Studies (DGS), on behalf of the program; we verify that this is the final, approved version of the student's thesis including all changes required by the advisory committee. The undersigned agree to abide by the statements above.

Deepak Kumar, Student

Dr. Vijay P. Singh, Major Professor

Dr. Aaron Cramer, Director of Graduate Studies

INVESTIGATION OF HOST NANOTUBE PARAMETERS FOR ENHANCING THE
PERFORMANCE OF NANOSTRUCTURED CDS-CDTE SOLAR CELLS

THESIS

A thesis submitted in partial fulfillment of the
requirements for the degree of Master of Science in Electrical
Engineering in the College of Engineering
at the University of Kentucky

By

Deepak Kumar

Lexington, Kentucky

Director: Dr. Vijay P. Singh, Professor of Electrical and Computer Engineering

Lexington, Kentucky

2020

Copyright © Deepak Kumar 2020
<https://orcid.org/0000-0001-9801-8820>

ABSTRACT OF THESIS

INVESTIGATION OF HOST NANOTUBE PARAMETERS FOR ENHANCING THE PERFORMANCE OF NANOSTRUCTURED CDS-CDTE SOLAR CELLS

Numerical simulations are performed to investigate the effects of host nanotube parameters (pore diameter and pitch for different CdS coverages) and CdTe doping density on device performance in nanowire CdS/ CdTe solar cells using SCAPS-1D. This research finds the optimum values for these parameters in order to achieve the highest efficiency. Experimentally the effect of anodization voltage and fluoride ion concentration on the pore diameter and the pitch are studied for the Titania nanotubes host. It is observed that in the range of 0.3 mL to 2 mL of ammonium fluoride content, pore diameter and the pitch of the Titania nanotube host matrix, fabricated in ethylene glycol-based electrolyte, is rather insensitive to the ammonium fluoride concentration. It is also shown that anodization voltage is the more effective parameter, which can be tailored and optimized to fabricate Titania Nanotube arrays of desired porosity. The bulk series resistance of the device, in addition to the CdTe doping density, varies upon varying the pore diameter and the pitch of the nanotubes for various fractions of CdS coverages. In this work, theoretical absorption profile was interpolated using the experimentally obtained absorption spectrum for various fractions of CdS coverages. The highest efficiency for this NW-CdS/CdTe solar cell structure at 300°K was found to be 25.93% with short circuit current of 28.3 mA cm^{-2} , open circuit voltage of 1.11 V and fill factor of 0.825; this was obtained when the pore diameter and the pitch of the host nanotube was in the range of 2.35nm – 23.48nm and 100nm – 1000nm respectively and the CdTe doping density was 10^{17} cm^{-3} . Thus, it is shown that the host nanotube parameters (pore diameter and pitch for different CdS coverages) and CdTe doping density can be tailored to give optimum device performance.

KEYWORDS: Nanowire Cadmium Sulfide, Cadmium Telluride, Nano porous Titania, SCAPS-1D, Simulation, Interface States

Deepak Kumar

02/03/2020

INVESTIGATION OF HOST NANOTUBE PARAMETERS FOR ENHANCING THE
PERFORMANCE OF NANOSTRUCTURED CDS-CDTE SOLAR CELLS

By
Deepak Kumar

Dr. Vijay P. Singh

Director of Thesis

Dr. Aaron Cramer

Director of Graduate Studies

02/03/2020

DEDICATION

To my parents, all my family members and friends for their encouragement and support.

ACKNOWLEDGMENTS

I would like to take this opportunity to express my sincere thanks and heartfelt gratitude to my academic advisor and thesis chair Dr. Vijay Singh for his invaluable guidance, encouragement and time during my Master's program and also for giving me an opportunity to work in his lab. I appreciate his support and motivation which inspired me to work hard throughout my thesis. In addition, he provided timely and instructive comments and evaluation at every stage of the thesis process, allowing me to complete this project on schedule.

I would like to extend my thanks to my thesis committee members Dr. Todd Hastings and Dr. Dan M. Ionel for their encouragement and valuable time for serving on my committee and for providing me with invaluable comments and suggestions.

Thanks, are also due to other members of our research group: Mr. Riasad Azim Badhan, Mr. Matthew Girard and Mr. Benjamin Williams for their technical assistance and support.

I am greatly indebted to my family members for their help and endless support. I would like to thank my father and mother for their support and blessings. Their support and blessings enabled me to stand confidently against all difficult times. I sincerely appreciate love and help from my friends especially Sandeep Rai, Richa Thakur, Kanakanagavalli Shravani Prakhya and Bhamiti Sharma without whose encouragement this work would not have been possible. Their confidence in my abilities has been a major motivating factor in completing my Master's study.

TABLE OF CONTENTS

ACKNOWLEDGMENTS	iii
LIST OF TABLES	vii
LIST OF FIGURES	viii
1 INTRODUCTION.....	1
1.1 Status of Solar Photovoltaics	1
1.2 Status of CdTe PV	3
1.3 Challenges in the CdTe technology	4
1.4 Objectives of this Research Work: Optimal Nanostructures in CdTe Solar Cells ..	5
2 Solar Cell Theory	7
2.1 Photovoltaic Effect.....	7
2.2 Solar cell	7
2.3 I-V Characteristics of a solar cell.....	10
2.4 p-n junction solar cell under illumination	11
2.5 Maximum Power delivered to the load	13
2.6 Solar cell Parameters	15
2.6.1 Open Circuit Voltage	15
2.6.2 Short Circuit Current density	16
2.6.3 Fill Factor	16
2.6.4 Power Conversion Efficiency	17
2.7 Resistance Calculations for Planar and Nanowire CdS/ CdTe device configuration.....	18
2.7.1 Resistance Calculation for Planar CdS/ CdTe device configuration	18
2.7.2 Resistance Calculation for Nanowire CdS/ CdTe device configuration.....	20
3 Experimental Procedures & Optical Characterization.....	23
3.1 Experimental Procedures.....	23
3.1.1 Substrate Cleaning	23
3.1.2 Microwave Induced Plasma Etch.....	23
3.1.3 RF Sputtering of Intrinsic Tin Oxide	23
3.1.4 DC Sputtering of Titanium	24
3.1.5 Titania Nanotubes formation	24
3.1.6 Annealing of as-anodized Titania Nanotubes	26

3.1.7	CdS Electrodeposition	26
3.2	<i>Optical Characterization</i>	28
3.2.1	Scanning Electron Microscopy	28
3.2.2	UV-Vis Spectroscopy	31
4	Host Nano-porous Template – Titania Nanotubes	32
4.1	<i>Nanoporous Titania</i>	32
4.2	<i>Parameters influencing the formation of Titania Nanotubes by anodic oxidation</i>	36
4.2.1	Effect of electrolyte on anodic oxidation of Titanium.....	36
4.2.2	Effect of water content on ethylene glycol based Titania nanotubes.....	37
4.2.3	Effect of anodization voltage	38
4.2.4	Effect of electrodes	39
4.2.5	Effect of aged electrolyte	39
4.2.6	Effect of anodization time.....	40
4.2.7	Effect of electrolyte temperature	40
4.2.8	Effect of electrolyte pH.....	41
5	Numerical Procedures and SCAPS Simulation	42
5.1	<i>The Physical Model</i>	43
5.2	<i>SCAPS 1-D Simulation Procedures</i>	46
6	Results and Discussion.....	66
6.1	<i>Nano porous Titania Template: Experimental results</i>	66
6.1.1.1	Effect of Fluoride ion concentration on pore diameter	74
6.1.1.2	Effect of anodization voltage on pore diameter	74
6.1.1.3	Effect of Fluoride ion concentration on the pitch	75
6.1.1.4	Effect of anodization voltage on pitch	75
6.2	<i>Numerical Results and Discussion</i>	77
6.2.1	Interpolation of absorption profile for various CdS coverages.....	77
6.2.2	Results and Discussion on SCAPS simulation	82
6.2.2.1	Short Circuit Current enhancement	84
6.2.2.2	Enhancement in the Open Circuit Voltage	88
6.2.2.3	Effect of decreasing CdS coverage on Fill Factor	92
6.2.2.4	Effect of decreasing CdS coverage on Efficiency	95
7	Conclusion and Future Work	100
7.1	<i>Solar Cell Device Performance</i>	100
7.2	<i>Titania Nanotubes Host Matrix</i>	102
7.3	<i>Suggestions for Future Work</i>	103

Appendix.....	104
References.....	161
Vita	169

LIST OF TABLES

Table 3.1 Tin Oxide and Titanium Sputtering Parameters	24
Table 3.2 Anodization conditions for Titania Nanotube formation.....	25
Table 5.1 Back contact material properties	53
Table 5.2 CdTe material properties	54
Table 5.3 Donor type defect parameters in CdTe	55
Table 5.4 Acceptor type defect parameters in CdTe	56
Table 5.5 CdTe / CdS Interface parameters.....	57
Table 5.6 CdS material properties	58
Table 5.7 Acceptor type defect parameters in CdS	59
Table 5.8 SnO ₂ material properties	60
Table 5.9 Neutral type defect parameters in SnO ₂	61
Table 5.10 FTO material properties.....	62
Table 5.11 Neutral type defect parameters in FTO	63
Table 5.12 Front contact material properties	64
Table 6.1 Effect of fluoride ion concentration and anodization voltage on pore diameter and interpore distance	67
Table 6.2 Effect of Effect of CdS Coverage on Voc, Jsc, FF and Efficiency for 10 ¹⁷ doping density	99

LIST OF FIGURES

Figure.2.1 I-V Characteristics of a solar cell under illumination	10
Figure 2.2 Equivalent Circuit of an ideal solar cell	11
Figure 2.3 Equivalent circuit of non-ideal device with finite series and shunt resistances	12
Figure 2.4 Equivalent circuit of ideal Solar cell under illumination with load R_L	13
Figure 2.5 Planar CdS/ CdTe device design (left) and Nanowire CdS/ CdTe device design (right) for deriving the bulk series resistance	18
Figure 2.6 Cross-Section view of the Nanowire CdS / Titania and CdTe interface.....	20
Figure 2.7 Top view of the Nanowire CdS and Titania Nanotube interface for bulk series resistance calculation	20
Figure 2.8 Top view of a single CdS Nanowire and Titania Nanotube Interface.....	21
Figure 3.1 LabView recorded - Anodization Current-time profile.....	26
Figure 3.2 Top view SEM image of TiO_2 Nanotube anodized at 60V	29
Figure 3.3 Cross Section SEM image of TiO_2 Nanotube anodized at 60V	29
Figure 3.4 1 st cross section SEM image of CdS Nanowires embedded in TiO_2 Nanotube array	30
Figure 3.5 2 nd cross section SEM image of CdS Nanowires embedded in TiO_2 Nanotube array	30
Figure 3.6 Absorption Curve generated from UV-Vis Spectroscopy data for Planar CdS and TiO_2 nanotubes with a porosity of 32%.	31

Figure 3.7 Transmission Curve generated from UV-Vis Spectroscopy data for Planar CdS and TiO ₂ nanotubes with a porosity of 32%.	31
Figure 5.1 Pauwells Vanhoutte Model for CdS/CdTe heterojunction.....	43
Figure 5.2 p-n heterojunction interface showing bending and discontinuities in bands...	43
Figure 5.3 Solar Cell Definition	46
Figure 5.4 SCAPS: Action Panel.....	47
Figure 5.5 SCAPS: Solar Cell Definition Panel	48
Figure 5.6 SCAPS: Layer Properties Panel	49
Figure 5.7 SCAPS: Defect Properties Panel.....	50
Figure 5.8 SCAPS: Contact Panel	51
Figure 5.9 SCAPS: Interface Panel.....	52
Figure 5.10 SCAPS: I-V Panel	65
Figure 6.1 Top view SEM image of Sample # 1 fabricated in a fresh electrolyte comprising of 98 mL of EG and 2 mL of NH ₄ F at an anodization voltage of 50 V.	68
Figure 6.2 Top view SEM image of sample # 2 fabricated in a fresh electrolyte comprising of 98 mL of EG and 2 mL of NH ₄ F at an anodization voltage of 60 V.	69
Figure 6.3 Top view SEM image of sample # 3 fabricated in a fresh electrolyte comprising of 98 mL of EG and 0.81 mL of NH ₄ F at an anodization voltage of 50 V.	70
Figure 6.4 Top view SEM image of sample # 4 fabricated in a fresh electrolyte comprising of 98 mL of EG and 0.3 mL of NH ₄ F at an anodization voltage of 40 V.	71
Figure 6.5 Top view SEM image of sample # 5 fabricated in a fresh electrolyte comprising of 98 mL of EG and 0.3 mL of NH ₄ F at an anodization voltage of 50 V.	72

Figure 6.6 Top view SEM image of sample # 6 fabricated in a used electrolyte comprising of 98 mL of EG and 0.3 mL of NH ₄ F at an anodization voltage of 60 V.	73
Figure 6.7 Absorption vs Wavelength for 32% CdS Coverage Experimental vs Theoretical	77
Figure 6.8 Theoretical absorption profile CdS Nanowires for 80% - 100% coverage	78
Figure 6.9 Theoretical absorption profile CdS Nanowires for 55% - 75% coverage	79
Figure 6.10 Theoretical absorption profile CdS Nanowires for 30% - 50% coverage	79
Figure 6.11 Theoretical absorption profile CdS Nanowires for 5% - 25% coverage	80
Figure 6.12 J _{sc} vs 1-100% CdS Coverage Interpore Distance 100nm	85
Figure 6.13 J _{sc} vs 0.0001-0.1% CdS Coverage Interpore Distance 100nm	87
Figure 6.14 V _{oc} vs 1-100% CdS Coverage Interpore Distance 100nm	90
Figure 6.15 V _{oc} vs 0.0001-0.1% CdS Coverage Interpore Distance 100nm	91
Figure 6.16 FF vs 1-100% CdS Coverage Interpore Distance 100nm	93
Figure 6.17 FF vs 0.0001-0.1% CdS Coverage Interpore Distance 100nm	94
Figure 6.18 Efficiency vs 0.0001-0.1% CdS Coverage Interpore Distance 100nm	96
Figure 6.19 Efficiency vs 1-100% CdS Coverage Interpore Distance 100nm	97

CHAPTER 1.INTRODUCTION

The photovoltaic effect was discovered by Edmund Becquerel in 1839. Becquerel while experimenting with an electrochemical cell consisting of a silver coated platinum electrode immersed in electrolyte observed the generation of a weak electrical current when the electrochemical cell was exposed to sunlight. However, it was not until 1954 when the first solar cell in the form of a diffused silicon p-n junction was developed by Bell Labs researchers Chapin, Fuller, and Pearson [1], quickly followed by the works of Reynolds, Leies, Antes, and Marburger [2] to develop cadmium sulfide (CdS) solar cell.

1.1 Status of Solar Photovoltaics

Conventional energy resources, such as fossil fuels, will be exhausted within the next century. In addition, the increasingly serious environmental problems all over the world have become a core driving force to promote renewable energy. The accelerated global warming and climate change is one of them, primarily due to the large carbon consumption from the burning of the fossil fuels since the Industrial Revolution. In 2016, the world just passed the symbolic 400 parts per million (PPM) threshold of CO₂ concentration, and the average temperature is also set to be the hottest year on record [3]. Therefore, renewable energy sources with low carbon emission is strongly desirable to rectify this situation.

Solar photovoltaics (PV) is a very attractive renewable energy source. According to one relevant study [4], PV installation on about 0.6% of the land in the US could be enough to meet the entire country's electricity need. Since the fabrication of PV modules consumes energy, some people have questioned PV's effectiveness on the reduction of

carbon emission. But this argument is not valid even for current PV technology. The average energy payback time (i.e., the module power output time needed to compensate the energy consumed for module production) of PV modules is ~ 1 years and decreasing with technology advances, but PV industry has widely guaranteed a 25-year product lifetime (i.e., producing 80% of its power over 25 years).

However, it must be admitted that the stimulation of government incentives and subsidies has been playing an important role in the PV market. To maintain a long-term and sustainable growth, and to have a more influential impact on climate change, the solar industry needs to rely less on the subsidies and develop economically competitive PV electricity. Many countries such as Spain, Italy, Germany, UK, and Japan, have encountered or are encountering a boom-bust cycle (i.e., with government subsidies, PV installation grows very fast in the first few years; but the installation sharply decreases once governments reduce or cut down the subsidies) due to a strong dependence of the subsidies [5].

The advancement of PV technology can contribute to reduce the PV system cost. That is to enable more efficient and durable PV products. For instance, First Solar, the world largest thin-film CdTe PV manufacturer, has reduced the CdTe module manufacturing cost from \$1.02/Watt in 2010 to \$0.51/Watt in 2015 [6] with its large investment on R&D. Within only 5 years, its cell and module efficiencies have been boosted from 16.5% to 22.1% and from 14.4% to 18.2% respectively [7]. The cost of PV systems can be further reduced by improving the reliability and decreasing the degradation rate of PV modules. The US National Renewable Energy Laboratory (NREL) has pointed

out that extending the PV system lifetime from a more standard expectation of 30 years to 50 years over long-term yields less PV system cost [8].

Overall, by taking its environment-friendly advantage, solar PV can play an important role in mitigating or even reversing the worsening climate change. With more efforts being made on technology improvements, it will possess more growth potential both economically and environmentally.

1.2 Status of CdTe PV

Since this thesis has a focus on CdTe solar cells, this section will give a brief summary of the current status and historic development of CdTe PV, and its advantages and disadvantages compared to the traditional Si PV technology (broadly including monocrystalline and polycrystalline Si). The research of CdTe-based PV devices began in the early 1960s, studied with a variety of device structures including homojunctions, heterojunctions, and Schottky barrier cells, and with efficiencies around 10% at that time [9]. By the middle of the 1990s, the cell efficiency increased to 15% for CdS/CdTe heterojunction configuration [10]. Recently, the cell efficiency has broken the 20% threshold by enhancing optical absorption and electrical properties [7]. As a result, the CdTe-based PV technology has become a mainstream PV technology in part due to a wealth of research advances. Today, First Solar has installed over 13.5 GW CdTe modules worldwide and continues to grow with ~3 GW of annual pipeline production [11].

Though the conventional Si PV technology occupies most of the PV market share, CdTe technology still possesses compelling advantages compared to Si and has the potential to increase the installation capacity. (1) The most obvious advantage of CdTe

over Si is a much lower material consumption due to its direct bandgap and thus high absorption coefficient. The typical CdTe absorber layers are usually 1-4 μm thick, while the crystalline Si wafers are over 100 μm thick. As a result, CdTe has a shorter energy payback time than Si cells (~ 2 years for silicon, but < 1 year for CdTe thin films) [12]. (2) CdTe has less strict material purity requirement (i.e., 100 times less than Si) and simpler manufacturing process than Si (i.e., the full process time: < 3.5 hours for CdTe but ~ 3 days for Si) [7]. (3) Since CdTe has a superior temperature coefficient, better spectral response, and better shading response, CdTe PV devices yield up to 12% higher energy density than Si in abundant sunshine region [7]. Because of these advantages, the current cost of CdTe module manufacturing is estimated to be $\$0.51/\text{W}$, cheaper than Si with $\$0.66\text{-}0.74/\text{W}$.

1.3 Challenges in the CdTe technology

CdTe based thin film solar cells are very attractive because of their low cost and relatively high efficiencies. CdTe has a close to optimal energy band gap of 1.5 eV for solar cell applications and a relatively high absorption coefficient (α) value of 10^5 cm^{-1} [13]. Therefore, it serves as the absorber layer in n-CdS/p-CdTe heterojunction solar cells, which is a leading thin-film solar cell technology today. Commercial CdTe cells have already achieved a Power Conversion Efficiency (PCE) of 22.1% [7]. This was achieved through increased scientific understanding and development of techniques including cadmium chloride treatment, thinning of the CdS window layer, incorporation of an interlayer between CdTe and the back electrode, and addition of a buffer layer between

CdS and the transparent electrode [14]. However, further improvements in PCE are needed to bring down the cost of solar power in dollars per watt.

In the past decade, improvement of efficiency has mostly been achieved by increasing short circuit current densities (J_{sc}). However, raising the V_{oc} beyond 900 mV has been a daunting challenge for the past two decades, due to several technical and fundamental material limitations associated with CdTe. Metzger et al. [15] has shown that, among the many characteristics of CdTe, including large lattice constant, low carrier concentration stemming from doping difficulties, and the lack of suitable II-VI hetero-partners to make ideal, lattice matched junctions, the most degrading is the excessively large interface state concentration at the CdTe-CdS heterojunction. They were able to demonstrate a V_{oc} of higher than 1 V by using single crystal CdTe for the absorber material in their cells. However, even though this single crystal technique is useful for research, it is not very practical for large-scale production as of now.

1.4 Objectives of this Research Work: Optimal Nanostructures CdTe Solar Cells

Advantages of using nanostructures in solar cell design have been described in the literature by the Ernst and Konnenkamp group [16], [17]. Also, earlier work in our Electronic Devices Research Laboratory (EDRL) by Dang et al [14] has shown that the performance output of CdS-CdTe solar cells can be enhanced by replacing the thin film CdS window layer in the traditional device design by CdS nanopillars. The above enhancement was demonstrated with CdS nanopillars of 60 nm diameter spaced to have a neighbor center to center distance of 105 nm. However, the parameters affecting the power conversion efficiency were not optimized because that was not the objective of their work.

In our research, an investigation was undertaken to study the various material and device parameters like CdTe doping level, diameter of the CdS nanopillars and the neighbor center to center distance for achieving the maximum solar cell power conversion efficiency in these devices.

More specifically, the ultimate objective of the work presented in this thesis is to study the effect of host nanotube parameters (pore diameter and pitch for different CdS coverages) and CdTe doping density on device performance in nanowire CdS/ CdTe solar cells using SCAPS-1D simulation, and to find the optimal set of conditions that will give the highest efficiency employing the nanowire CdS/ CdTe device design. An overview of the structure of the thesis is as follows:

- i. Chapter 2 includes a description of the simple p-n junction theory. Bulk series resistance formula for the case of planar and nanowire CdS device design have been derived.
- ii. Chapter 3 describes the experimental procedures and characterization techniques used. The pore diameter, the pitch and the porosity for the fabricated devices are investigated by SEM characterization. UV-VIS spectrophotometry measurements of the fabricated devices are also presented.
- iii. Chapter 4 reviews the nanoporous titania template and details the literature review to understand the effect of various parameters influencing the formation of Titania Nanotubes.
- iv. Chapter 5 gives the description of the working of SCAPS-1D package.
- v. Chapter 6 does the analysis of the results obtained.
- vi. Chapter 7 discusses the conclusions and provides the suggestions for future work.

CHAPTER 2.SOLAR CELL THEORY

2.1 Photovoltaic Effect

The Photovoltaic Effect was discovered in 1839 by French Experimental Physicist Edmund Becquerel. Becquerel while experimenting with an electrochemical cell consisting of a silver coated platinum electrode immersed in electrolyte observed the generation of a weak electrical current when the electrochemical cell was exposed to sunlight.

2.2 Solar cell

The fundamental elements of a solar cell required for the conversion of light energy into electrical energy owing to the photovoltaic effect are: (i) Junction, where the charge separation of light induced electrons and holes occurs; (ii) Absorber material, where the photons gets absorbed; and (iii) contacts, where the electrons and holes are collected to give electrical current to drive the load.

A solar cell comprises of a p-n junction. The junction formed can be homojunction or heterojunction. When the p-type and the n-type regions of the same semiconductor is brought together gives rise to a homojunction. The built-in potential across the p-type and the n-type semiconductor homojunction in thermal equilibrium is equal to the difference in the work functions and is given by

$$V_{bi} = \frac{kT}{q} \ln \left(\frac{N_A N_D}{n_i^2} \right) \quad (2.1)$$

Where N_A and N_D are the acceptor and the donor concentrations of the p-type and the n-type semiconductor respectively and n_i is the intrinsic carrier concentration of the semiconductor.

This built-in potential gives rise to the electric field, which in turn separates the light induced electrons and holes, when the solar cell is connected across the load.

The width of the depletion region which is a function of built-in potential, the acceptor concentration and the donor concentration. For a two-sided abrupt junction, the depletion width is given by

$$W = \left[\frac{2V_{bi}\epsilon_s}{q} \left(\frac{1}{N_A} + \frac{1}{N_D} \right) \right]^{\frac{1}{2}} \quad (2.2)$$

For a one-sided abrupt junction, the depletion width is given by

$$W = \left[\frac{2V_{bi}\epsilon_s}{qN_B} \right]^{\frac{1}{2}} \quad (2.3)$$

Where $N_B = N_A$ or N_D , depending on whether $N_A \gg N_D$ or $N_A \ll N_D$

When two semiconductor materials of different energy bandgaps are brought together, the junction formed is termed as heterojunction. The quality of heterojunction formed depends on (i) the electron affinities of the semiconductor materials, difference in electron affinities can result in energy discontinuities in the energy bands; (ii) lattice constant of the semiconductor materials; and (iii) the thermal expansion coefficients. Interfacial dislocations at the interface gives rise to interface states which acts as trapping centers, could result from the mismatch in lattice constant and thermal expansion coefficients of the two semiconductor materials.

The built-in potential across the p-type and the n-type semiconductor heterojunction in thermal equilibrium is equal to the difference in the work functions and is given by

$$V_{bi} = E_{g2} - (E_f - E_{c2}) + \chi_2 - \chi_1 - (E_{c1} - E_f) \quad (2.4)$$

Where E_g , E_f , E_c and χ are the energy bandgap, fermi level, conduction band and the electron affinity respectively for the semiconductor materials.

In a p-n junction diode in equilibrium, the net electron and hole current is zero. There are internal electron diffusion current and electron drift current, but they are equal and opposite. Therefore, the net electron current is zero. Similarly, net hole current is also zero.

The light generated current is contributed by: (i) Holes generated in the n-region by incident photons, (ii) Electrons generated in the p-region by incident photons and (iii) Electron-hole pairs (EHP) generated in the depletion region by incident photons. At the front surface the current is controlled by the surface recombination velocity, the surface recombination current balances out the diffusion current from the n-region. The photocurrent contribution from the electron-hole pairs in the depletion region is not affected by recombination, the electric field is so high that the photogenerated electrons and holes are immediately swept away by the electric field and there is no time for recombination.

2.3 I-V Characteristics of a solar cell

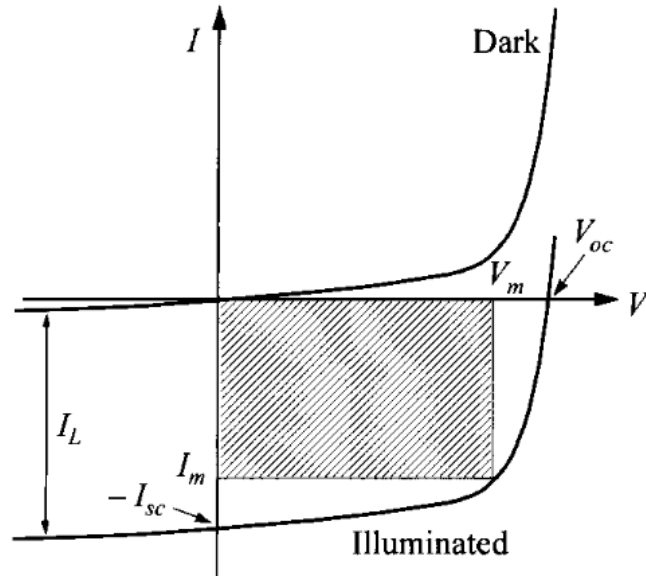


Figure.2.1 I-V Characteristics of a solar cell under illumination

Figure.2.1 shows the typical I-V Characteristics of a solar cell under illumination [19]. At higher illumination intensities the effect of high series resistance, R_s , becomes more pronounced while at lower illumination intensities the effect of poor shunt resistance, R_{sh} , is more predominant. The shunt resistance, R_{sh} , value can be readily obtained from the IV curve by taking the inverse of the slope of the IV curve in the third quadrant. The series resistance, R_s , can be estimated by finding the inverse of the slope of the IV curve at the open circuit voltage.

The dark I-V characteristics of the solar cell follow the ideal I-V characteristics of a diode

$$I = I_0 \left[\exp \frac{qV_F}{\eta kT} - 1 \right] \quad (2.5)$$

Under illumination from sunlight

$$I = I_0 \left[\exp \frac{qV_F}{\eta kT} - 1 \right] - I_L \quad (2.6)$$

Where I_L is the light generated current.

2.4 p-n junction solar cell under illumination

The equivalent circuit of an ideal solar cell consists of a constant current source and a diode.

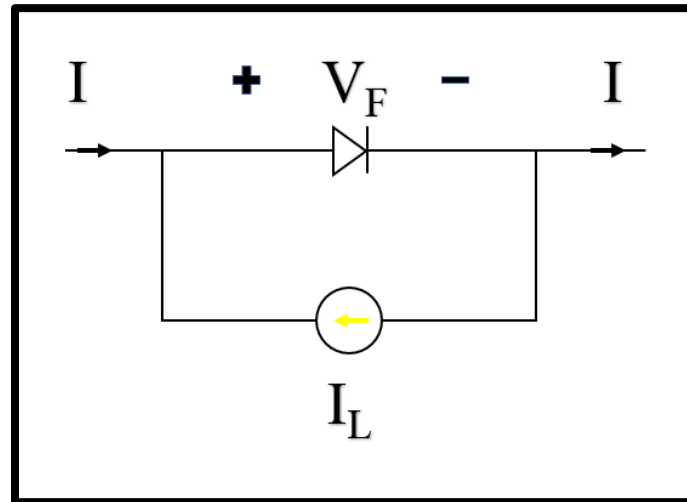


Figure 2.2 Equivalent Circuit of an ideal solar cell

The equivalent circuit of a solar cell consists of a constant current source, a diode, the series and shunt resistances associated with the diode.

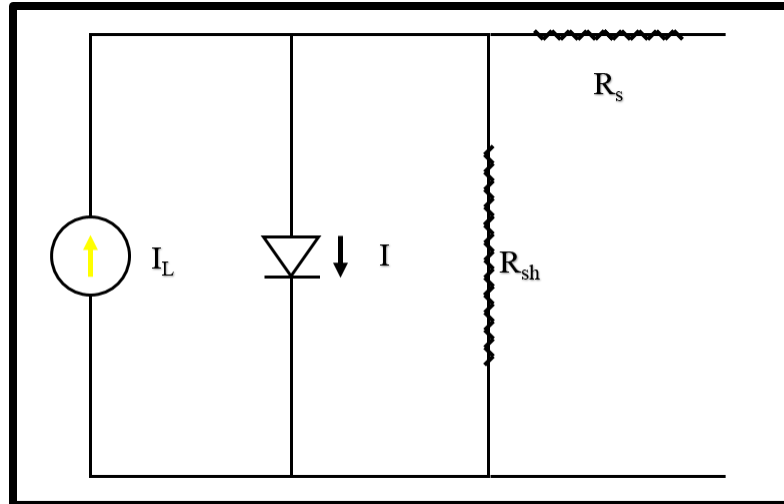


Figure 2.3 Equivalent circuit of non-ideal device with finite series and shunt resistances

Case I: Short Circuit

$V_F = 0$ gives

$$I_{SC} = I_L \quad (2.7)$$

Case II: Open Circuit

$I = 0$ gives

$$V_{OC} = \frac{\eta kT}{q} \ln \left(\frac{I_L}{I_0} + 1 \right) \quad (2.8)$$

Case III: At load

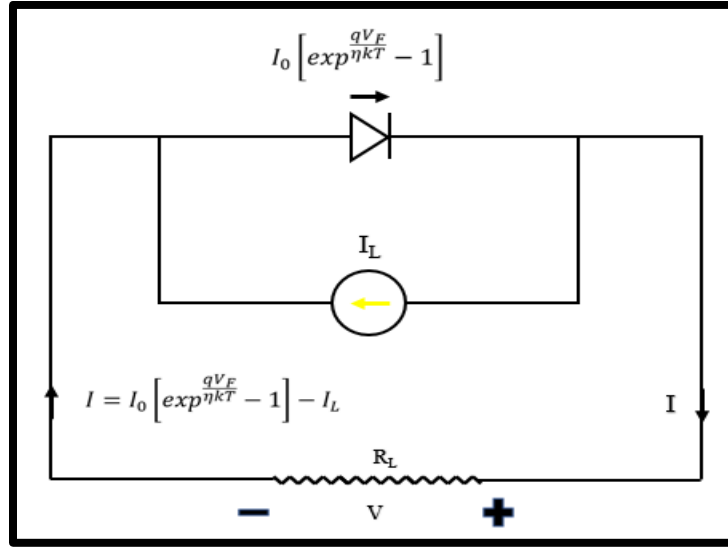


Figure 2.4 Equivalent circuit of ideal Solar cell under illumination with load R_L

$$I = I_0 \left[\exp \frac{qV_F}{\eta kT} - 1 \right] - I_L \quad (2.9)$$

and

$$V = \frac{\eta kT}{q} \ln \left(\frac{I_L}{I_0} + 1 \right) \quad (2.10)$$

2.5 Maximum Power delivered to the load

Power delivered to the load

$$P = -VI = \left(\frac{\eta kT}{q} \right) I \ln \left(\frac{I_L}{I_0} + 1 \right) \quad (2.11)$$

The power delivered would be maximum when

$$\frac{dP}{dI} = 0 \quad (2.12)$$

The maximum current and maximum voltage are given by:

$$I_m = I_0 \frac{qV_m}{kT} e^{\frac{qV_m}{\eta kT}} \approx I_L \left(1 - \frac{\eta kT}{qV_m} \right) \quad (2.13)$$

$$V_m = \frac{\eta kT}{q} \ln \left[\frac{\frac{I_L}{I_0} + 1}{1 + \frac{qV_m}{\eta kT}} \right] \approx V_{OC} - \frac{\eta kT}{q} \ln \left(1 + \frac{qV_m}{\eta kT} \right) \quad (2.14)$$

The above equation is a transcendental equation. Its numerical solution yields the value of V_m that needs to be calculated using iterative method. Then I_m is found by plugging in the value of V_m . Once the values of V_m and I_m are obtained, those can be used to calculate the maximum power delivered from the solar cell.

Maximum power obtained is given by:

$$P_m = V_m I_m = V_{OC} * I_{SC} * FF \quad (2.15)$$

$$\approx I_L \left[V_{OC} - \frac{q}{\eta kT} \ln \left(1 + \frac{qV_m}{\eta kT} \right) - \frac{\eta kT}{q} \right]$$

2.6 Solar cell Parameters

The performance of a solar cell is characterized in terms of open circuit voltage (V_{OC}), short circuit current (I_{SC}) and the fill factor (FF). The product of these three quantities gives the maximum power output of the device.

2.6.1 Open Circuit Voltage

The open-circuit voltage of a solar cell is given by

$$V_{OC} = \frac{\eta k T}{q} \ln \left(\frac{J_{SC}}{J_0} + 1 \right) \quad (2.16)$$

Where η is the diode ideality factor, k is the Boltzmann constant, T is the operating temperature, q is the electronic charge, J_{SC} is the short circuit current density and J_0 is the saturation current density.

The saturation current density is given by

$$J_0 = q N_C N_V \left(\frac{1}{N_A} \sqrt{\frac{D_n}{\tau_n}} + \frac{1}{N_D} \sqrt{\frac{D_p}{\tau_p}} \right) e^{-\frac{E_g}{kT}} \quad (2.17)$$

Where N_C is the density of states of the conduction band, N_V is the density of states of the valence band, N_A is the acceptor density, D_n is the diffusion length of electrons, τ_n is the carrier lifetime of electrons, N_D is the donor density, D_p is the diffusion length of holes, τ_p is the carrier lifetime of holes and E_g is the band gap of the absorber material.

2.6.2 Short Circuit Current density

The short-circuit current density over the entire solar spectrum is given by

$$J_{SC} = \int_{\lambda_{min}}^{\lambda_{max}} (J_n + J_p + J_d) d\lambda \cong q \int_{\lambda_{min}}^{\lambda_{max}} F(1 - R) d\lambda \quad (2.18)$$

Where λ_{min} is 0.3 μm for sunlight, λ_{max} is the wavelength corresponding to the absorption edge of the absorber material, J_n is the electron current density, J_p is the electron current density, J_d is the photocurrent density in the space charge region, F is the incident photon flux and R is the reflectivity of the light at the surface. The approximation in the above equation is valid when the diffusion length (L) is very large such that $\alpha L \gg 1$, where α is the absorption coefficient of the absorber material.

2.6.3 Fill Factor

Fill Factor represents how close the real solar cell is to ideal solar cell and is a measure of the "squareness" of the IV curve and represents the area of the largest rectangle that will fit the IV curve. FF is defined as the ratio of maximum power from the solar cell to the product of V_{OC} and I_{SC} .

$$FF = \frac{P_{mp}}{V_{OC} * I_{SC}} = \frac{V_{mp} * I_{mp}}{V_{OC} * I_{SC}} \quad (2.19)$$

Where P_{mp} is the maximum power delivered from the solar cell, V_{mp} is the voltage at the maximum power point and I_{mp} is the current at the maximum power point.

When the parasitic series resistance and shunt resistance, R_s and R_{sh} , both have negligible effect on the solar cell performance, the fill factor can be approximately expressed in terms of open-circuit voltage as [18]

$$FF = \frac{\frac{qV_{OC}}{kT} - \ln\left(0.72 + \frac{qV_{OC}}{kT}\right)}{1 + \frac{qV_{OC}}{kT}} \quad (2.20)$$

However, when either the series resistance or the shunt resistance has significant effect on the device performance the above equation may yield inaccurate results.

2.6.4 Power Conversion Efficiency

Power conversion efficiency (PCE): Power conversion efficiency is defined as the ratio of maximum power that the solar cell can deliver to the incident power from the incoming solar radiation.

$$\begin{aligned} PCE (\eta) &= \frac{P_m(\text{Maximum Power that the solar cell can deliver})}{\text{Incident Power from Sunlight}} \\ &= \frac{V_{OC} * I_{SC} * FF}{P_{inc}} \end{aligned} \quad (2.21)$$

Where P_{inc} is the incident power from the incoming solar radiation and is given by

$$P_{inc} = A \int_0^{\infty} F(\lambda) \left(\frac{hc}{\lambda}\right) d\lambda \quad (2.22)$$

A is the total device area, $F(\lambda)$ is the incident photon flux and $\left(\frac{hc}{\lambda}\right)$ is the energy associated with each photon.

2.7 Resistance Calculations for Planar and Nanowire CdS/ CdTe device configuration

2.7.1 Resistance Calculation for Planar CdS/ CdTe device configuration

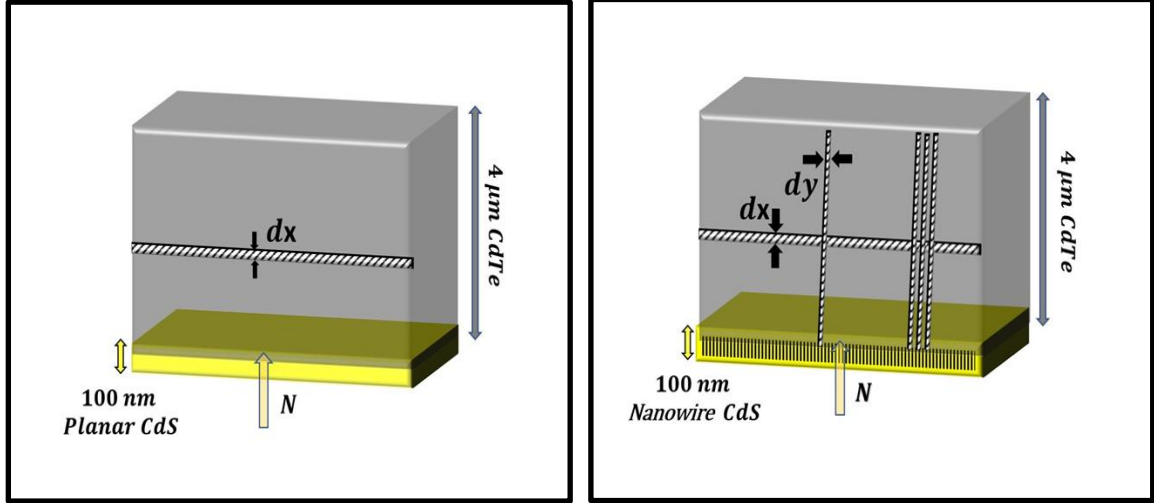


Figure 2.5 Planar CdS/ CdTe device design (left) and Nanowire CdS/ CdTe device design (right) for deriving the bulk series resistance

$$N_1(\lambda) = N_1[e^{-\alpha x} - e^{-\alpha(x+dx)}] \quad (2.23)$$

Where, $N_1(\lambda)$ is the # of photons per sec per cm^2 incident on CdTe, $N(x)dx$ is the # of photons absorbed in the strip (x) to $(x + dx)$ and α is the absorption coefficient.

Then,

$$\Delta i_e(x) = q\eta N_1 e^{-\alpha x} [1 - e^{-\alpha \Delta x}] \quad (2.24)$$

$$\cong q\eta N_1 e^{-\alpha x} (\alpha \Delta x)$$

Where, η is the quantum efficiency, R_1 is the Resistance encountered by $\Delta i_e(x)$ for reaching the CdS/ CdTe junction and q is the electronic charge.

for Area (A) = 1 cm^2

$$R_1 = \frac{\rho_p x}{\text{Area}} = \frac{x}{\sigma_p} = \frac{x}{q\mu_p p (1 \text{ cm}^2)} \quad (2.25)$$

Then the voltage drop due to $\Delta i_e(x)$

$$\Delta V_1 = \frac{q\eta N_1 e^{-\alpha x} (\alpha dx)}{q\mu_p p (1 \text{ cm}^2)} \quad (2.26)$$

Therefore, the total voltage drop

$$V_{eff} = \int \Delta V_1 = \int_0^{t_{CdTe}} \frac{q\eta N_1 e^{-\alpha x} (\alpha dx)}{q\mu_p p A} \quad (2.27)$$

The effective bulk series resistance for planar CdS/ CdTe cell will be given by

$$R_{eff \text{ planar}} = \frac{V_{eff}}{I_L} = \frac{\eta N_1 \alpha}{I_L \mu_p p A} \int_0^{t_{CdTe}} x e^{-\alpha x} dx \quad (2.28)$$

$$R_{eff \text{ planar}} = \frac{\eta N_1 \alpha}{I_L \mu_p p A} \left[\frac{x e^{-\alpha x}}{\alpha} - \frac{e^{-\alpha x}}{\alpha^2} \right]_0^{t_{CdTe}}$$

$$R_{eff \text{ planar}} = \frac{\eta N_1 \alpha}{I_L \mu_p p A} \left[\frac{t e^{-\alpha t}}{\alpha} - \frac{e^{-\alpha t}}{\alpha^2} + \frac{1}{\alpha^2} \right] \quad (2.29)$$

The expression above gives the effective bulk series resistance encountered by the window-absorber layer in the conventional CdS/ CdTe device configuration.

2.7.2 Resistance Calculation for Nanowire CdS/ CdTe device configuration

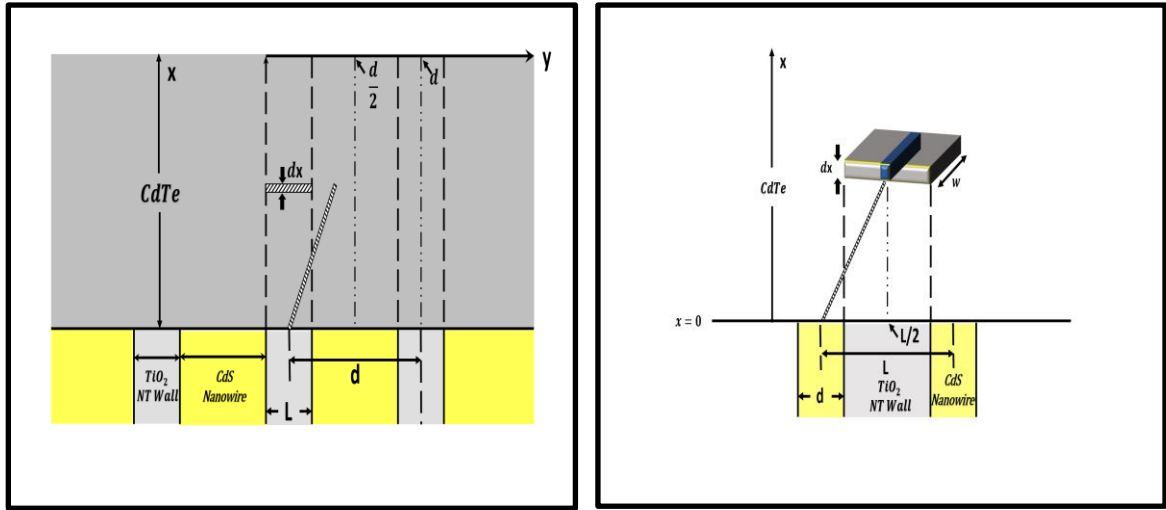


Figure 2.6 Cross-Section view of the Nanowire CdS / Titania and CdTe interface

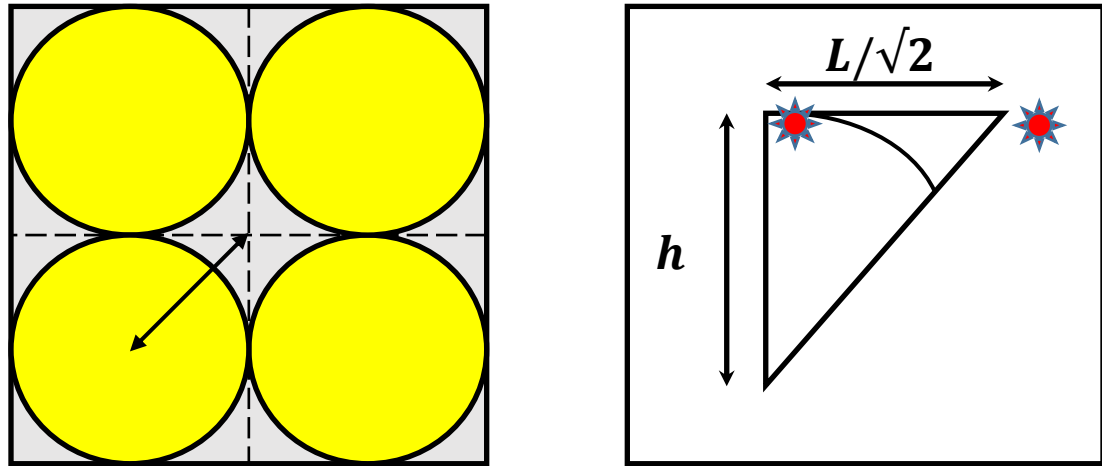


Figure 2.7 Top view of the Nanowire CdS and Titania Nanotube interface for bulk series resistance calculation

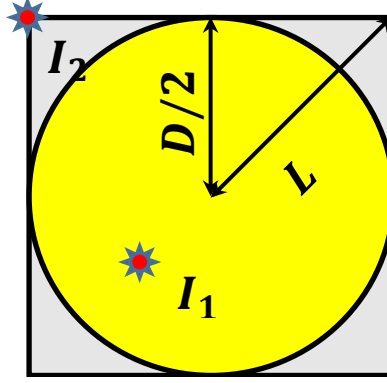


Figure 2.8 Top view of a single CdS Nanowire and Titania Nanotube Interface

The photons that are absorbed in CdTe in a region directly above the CdS nanopillars, do not pose any extra resistance in comparison to planar CdS, the electrons that contribute a current I_1 must travel 'h', here 'h' denotes the thickness of the CdTe layer, as shown in figure 5(b). However, electron-hole generated by the photons that are absorbed in CdTe in a region that doesn't lie directly above the CdS nanopillars will have to traverse a distance of $\frac{L}{\sqrt{2}} - \frac{D}{2}$ more, contributes a current I_2 . The total photo current generated will be sum of these two currents. Therefore,

$$I = I_1 + I_2 \quad (2.30)$$

The current I_1 will be proportional to area of the CdS nanopillars,

$$I_1 \propto \pi \frac{D^2}{4} \quad (2.31)$$

Similarly, the current I_2 will be proportional to the area of TiO_2 only, i.e., the difference in area of the square and the circle,

$$I_2 \propto L^2 - \pi \frac{D^2}{4} \quad (2.32)$$

Considering the resistance offered to the electron-hole pairs generated directly above the CdS nanopillar is R_1 . The extra resistance offered by the electron-hole pairs generated above the non-CdS region for travelling a distance $\frac{L}{\sqrt{2}} - \frac{D}{2}$ more will be

$$\Delta R = R_1 \left(\frac{L}{\sqrt{2}} - \frac{D}{2} \right) * \frac{1}{h} \quad (2.33)$$

The total effective resistance offered to the electron-hole pairs that are generated in a region that does not lie directly above the CdS nanopillar will be

$$R_2 = R_1 + \Delta R = R_1 \left(\frac{L}{\sqrt{2}} - \frac{D}{2} \right) * \frac{1}{h} \quad (2.34)$$

Now, the effective resistance offered by nanostructured configuration is given by

$$R_{eff \text{ nanowire}} = \frac{I_1 R_1 + I_2 R_2}{I_1 + I_2} \quad (2.35)$$

$$R_{eff \text{ nanowire}} = \frac{R_1 \left[1 + \frac{\pi D^2}{4 \left[L^2 - \frac{\pi D^2}{4} \right]} \right] * \left[1 + \left(\frac{L}{\sqrt{2}} - \frac{D}{2} \right) * \frac{1}{h} \right]}{\left[1 + \frac{\pi D^2}{4 \left[L^2 - \frac{\pi D^2}{4} \right]} \right]} \quad (2.36)$$

Therefore, the effective nanowire resistance will be given by

$$R_{eff \text{ nanowire}} = R_1 * \left[1 + \left(\frac{L}{\sqrt{2}} - \frac{D}{2} \right) * \frac{1}{h} \right] \quad (2.37)$$

$$\frac{R_{eff \text{ nanowire}}}{R_{eff \text{ Planar}}} = \left[1 + \left(\frac{L}{\sqrt{2}} - \frac{D}{2} \right) * \frac{1}{h} \right] \quad (2.38)$$

CHAPTER 3. EXPERIMENTAL PROCEDURES & OPTICAL CHARACTERIZATION

3.1 Experimental Procedures

3.1.1 Substrate Cleaning

Commercially available Indium Tin Oxide (ITO) Soda Lime Glass Substrate (MSE Supplies 80-85% Transmittance, sheet resistance 12-15 Ω /square, 25 x 25 x 1.1 mm) were ultrasonicated in Acetone (Alfa Aesar ACS 99.5+%) bath and Isopropyl Alcohol (Fisher Chemical, 2-Propanol Certified ACS Plus) bath for 30 minutes each. The samples were then rinsed in de-ionized water and dried in nitrogen flow before the microwave induced plasma etch cleaning.

3.1.2 Microwave Induced Plasma Etch

The ITO glass substrates post cleaning was subjected to microwave induced plasma etch for 1 minute at 100% power in Argon gas. The samples were then masked using Al foil, leaving out some area for ITO cathode, before sputtering.

3.1.3 RF Sputtering of Intrinsic Tin Oxide

100nm of Intrinsic Tin Oxide (SnO_2 , Goodfellow, 99.9%) was deposited by RF magnetron sputtering using AJA Phase II J Sputtering System at the Center of Advanced Materials (CAM) at the University of Kentucky. The deposition rate was maintained around 1.587nm/min. The deposition parameters used during sputtering are given in Table 3.1. Highly resistive Intrinsic Tin Oxide acts as the buffer layer as they are known to enhance the open circuit voltage (V_{OC}) and fill factor (FF) when very thin film of CdS window-layer is used in thin film CdTe solar cells [21].

3.1.4 DC Sputtering of Titanium

Titanium was also deposited using DC magnetron sputtering using AJA Phase II J Sputtering System at the Center of Advanced Materials at the University of Kentucky. Different deposition parameters used for depositing Titanium is shown in Table 3.1.

Table 3.1 Tin Oxide and Titanium Sputtering Parameters

Parameters	Intrinsic Tin Oxide	Titanium
Base Pressure	$3-7 \times 10^{-8}$ Torr	$3-7 \times 10^{-8}$ Torr
Deposition Pressure	3 mTorr	3 mTorr
Deposition Power	30 W	150 W
Deposition Time	63 minutes	36 minutes
Deposition Rate	1.58 nm/min	4.2 nm/min
Stage Temperature	24°C	300°C
Pre-Sputtering Time	2 minutes	2 minutes

3.1.5 Titania Nanotubes formation

The sputtered Titanium samples were used for converting Titanium to Titania Nanotube array using anodic oxidation. The anodization solution consisted of 98 mL Ethylene Glycol (Fisher, ACS Grade) and 0.3 mL Ammonium Fluoride (NH₄F, 40% by vol, JT Baker) in a PTFE beaker. PTFE beaker was first cleaned and dried in Nitrogen. Then a half-inch magnetic stirrer was placed in the beaker. 98 mL of Ethylene Glycol was measured and poured into the beaker. 0.3 mL of Ammonium Fluoride was mixed in Ethylene Glycol with the help of a pipette using forward pipetting method. The solution was mixed at 400 rpm for 30 minutes prior to performing any anodization of the Titanium samples.

Table 3.2 Anodization conditions for Titania Nanotube formation

Anodization Solution	98 mL EG + (0.3 - 2 mL) NH ₄ F
Anodization Voltage	40V-60V
Stirring speed during Anodization	200 rpm
Anodization Time	Varies from sample to sample, anodization can be stopped when the current approaches 0.3-0.5 mA
Solution Temperature	Room temperature

The solution preparation and the anodization were carried under the fume hood due to the fluoride ions. A 1"x1" Platinum electrode was used as the cathode. The Platinum Electrode was rinsed with DI Water thoroughly (front and back) 2-3 times and was dried in Nitrogen flow. The Platinum electrode was connected to the positive supply terminal and the Titanium sample was clipped on to the negative terminal of the supply.

Anodization was carried out using potentiostatic method, the parameters used are given in Table 3.2. Different anodization voltages between 40V-60V were applied to obtain Titania nanotubes of different pore diameters. The factors affecting the formation of Titania nanotubes has been discussed in detail in Chapter 4.

During anodization the color change of the sample in the solution was noticed from dark purple – blue – green – finally getting transparent. The voltage supply was turned off when the current approached a very low value of 0.3-0.5 mA, which indicates that the whole Titanium has been anodized. The sample was taken out of the solution, rinsed thoroughly in DI water and was dried in Nitrogen flow.

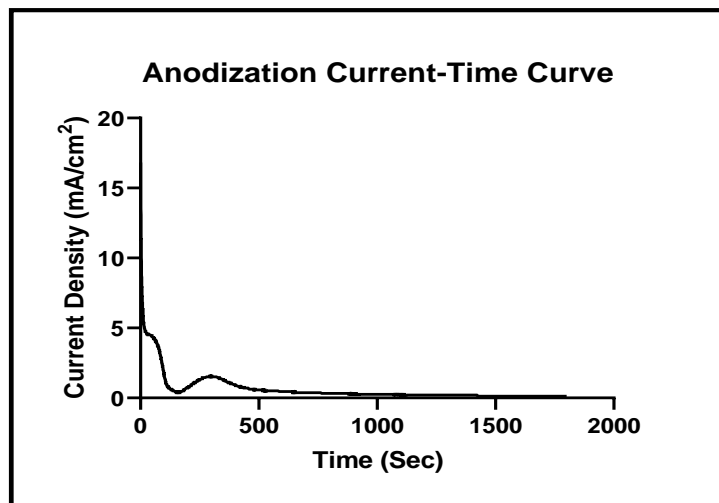


Figure 3.1 LabView recorded - Anodization Current-time profile

3.1.6 Annealing of as-anodized Titania Nanotubes

The as-anodized TiO₂ nanotube samples were annealed for 2 hours in Oxygen environment. The electrical and optical properties of Titania nanotubes are not influenced significantly by the anodization conditions but can strongly modified by proper heat treatment. The as-anodized Titania nanotubes are amorphous in nature and can be converted to anatase or rutile crystalline form by heat treating at a suitable temperature. Annealing between 350°C-450°C leads to predominant anatase form while annealing beyond 450°C leads to rutile phase [20]. An increase in peak intensities are observed with an increase in annealing time leading to better crystallized anatase or rutile structures [21]. Electrical conductivity of anatase phase is significantly higher than that of the rutile phase, significant increase in conductivity after crystallization to anatase [22].

3.1.7 CdS Electrodeposition

The solution was first prepared by taking 50mL of Dimethyl Sulfoxide (DMSO) into a beaker of suitable size. Prior to adding DMSO into the beaker half-inch magnetic

stirrer was cleaned and placed in the beaker. Then elemental Sulfur powder and Cadmium Chloride powder were measured 0.5 gm each and were poured in the beaker containing Dimethyl Sulfoxide. The beaker was placed on a hot plate and the hot plate was set to 150°C, close to the boiling point of DMSO. The temperature of the solution was monitored using infrared thermometer. The solution was stirred at 300 rpm so that the solution is mixed throughout.

Platinum electrodes which act as anode during electrodeposition was cleaned with DI water and dried in Nitrogen flow. After cleaning, the Platinum electrode was connected to the positive terminal of the supply. The TiO₂ nanotubes samples obtained from the previous step was connected to the negative terminal of the supply. The electrodes were then immersed in the saturated solution of Cadmium Sulfide, stirring was stopped. A current density of 7.5 mA/cm^2 was applied to the electrodes during electrodeposition. A constant DC current was applied for ~10 seconds to electrodeposit CdS into TiO₂ nanotube array.

When the deposition is complete the samples were taken out and rinsed with DI water and were dried in Nitrogen. To enhance the crystallinity of the nanowire CdS the electrodeposited CdS samples were heat treated in Argon environment at 385°C for 30 minutes.

3.2 Optical Characterization

3.2.1 Scanning Electron Microscopy

SEM images were taken using Hitachi S-4300 Scanning Electron Microscope and FEI Helios Nanolab 660 in the Electron Microscopy Center (EMC) located at the University of Kentucky.

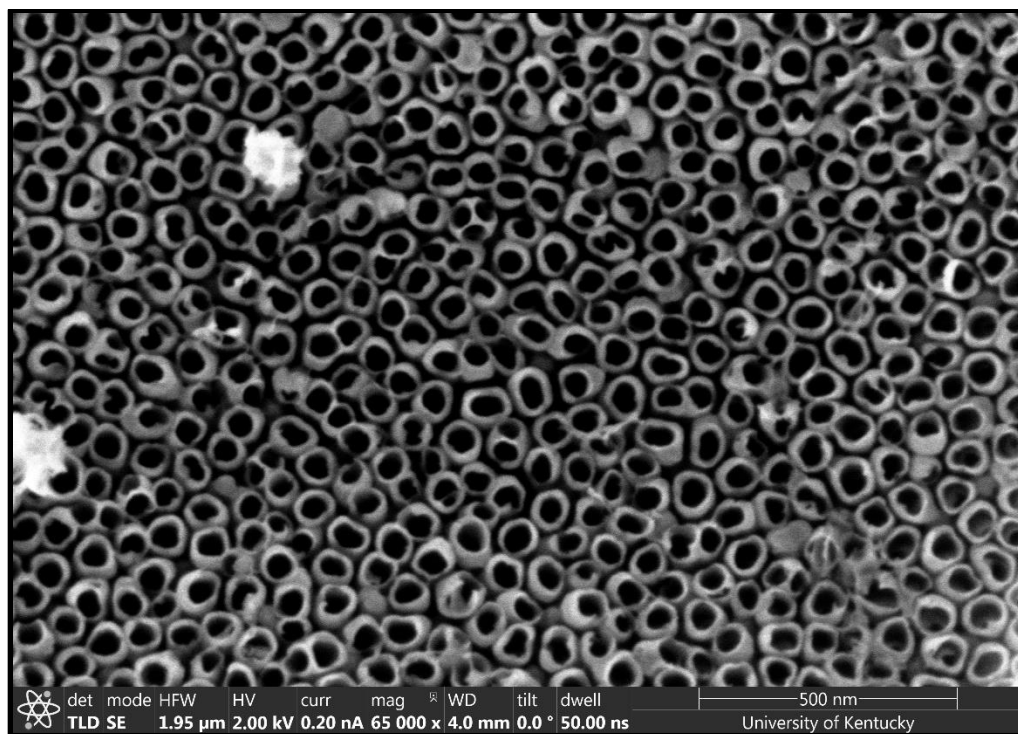


Figure 3.2 Top view SEM image of TiO₂ Nanotube anodized at 60V

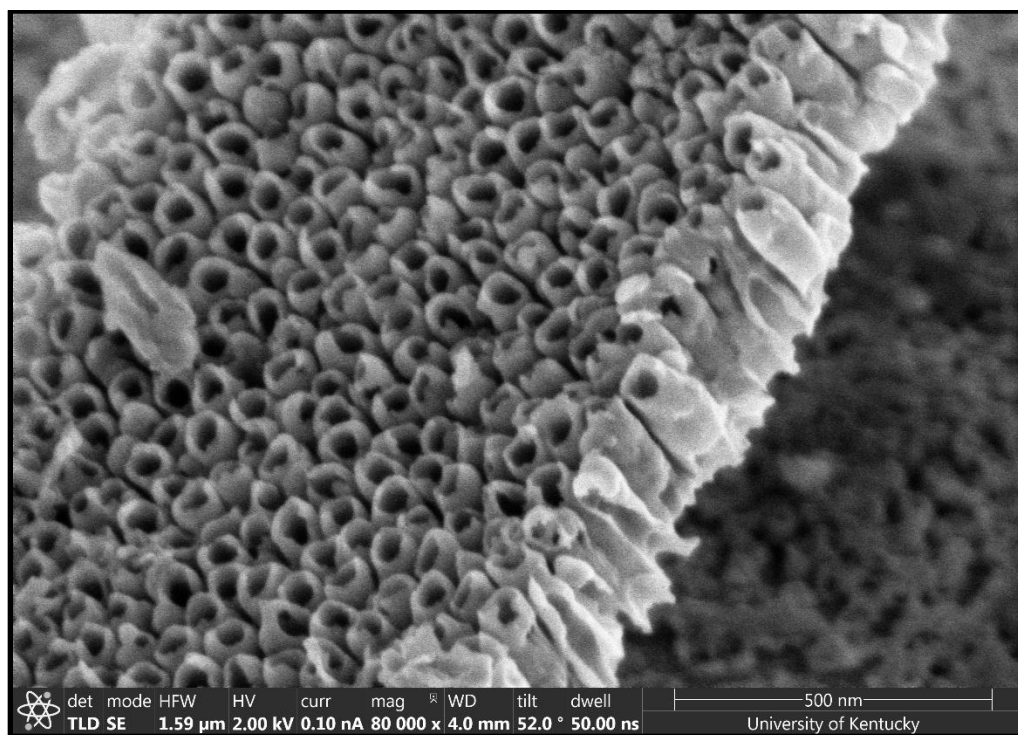


Figure 3.3 Cross Section SEM image of TiO₂ Nanotube anodized at 60V

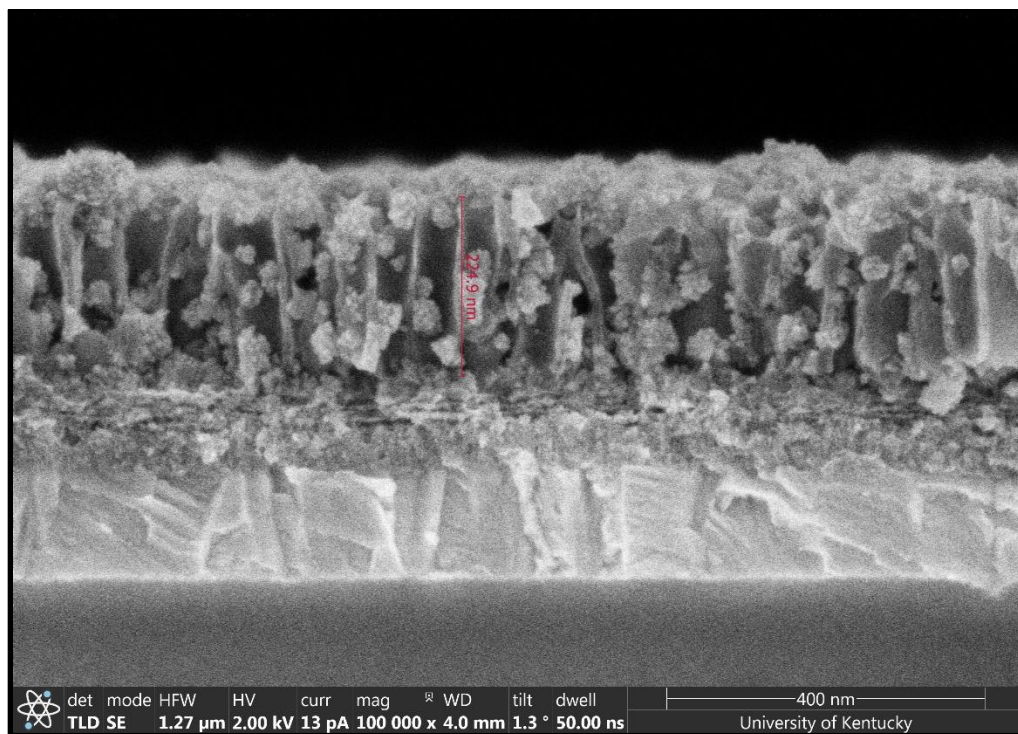


Figure 3.4 1st cross section SEM image of CdS Nanowires embedded in TiO₂ Nanotube array

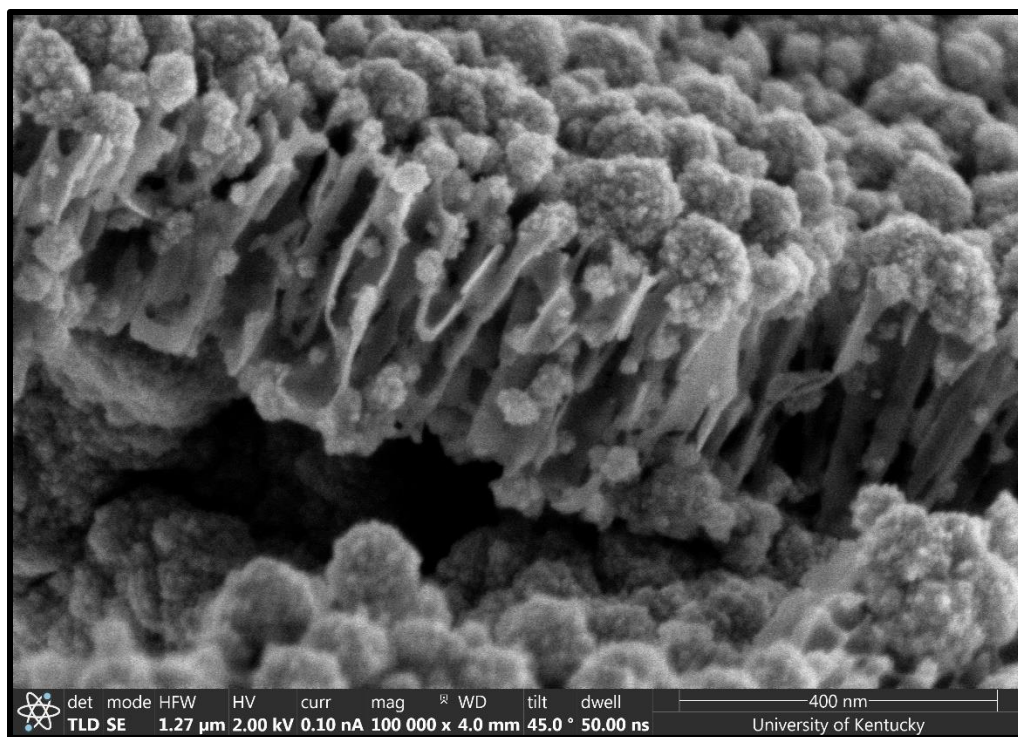


Figure 3.5 2nd cross section SEM image of CdS Nanowires embedded in TiO₂ Nanotube array

3.2.2 UV-Vis Spectroscopy

Cary 50 UV-Vis Spectrophotometer was used to take the absorption and the transmission data for the TiO₂ nanotubes and Planar CdS.

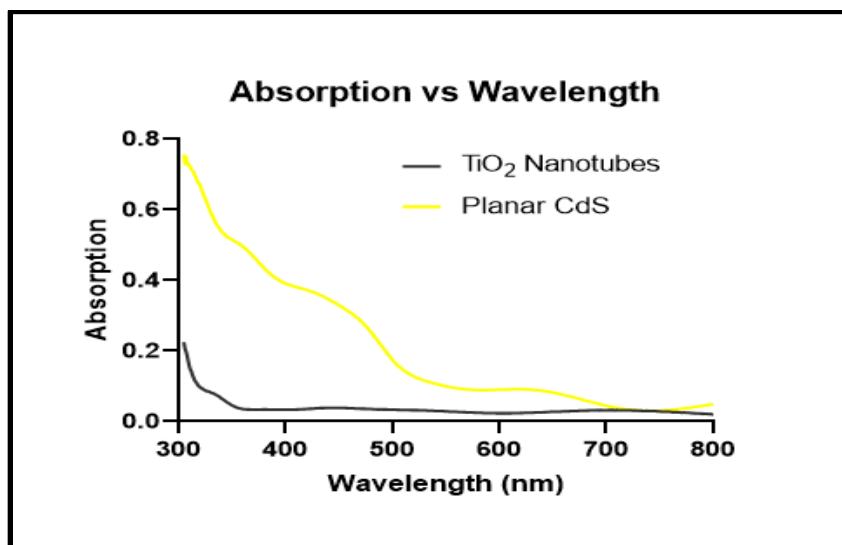


Figure 3.6 Absorption Curve generated from UV-Vis Spectroscopy data for Planar CdS and TiO₂ nanotubes with a porosity of 32%.

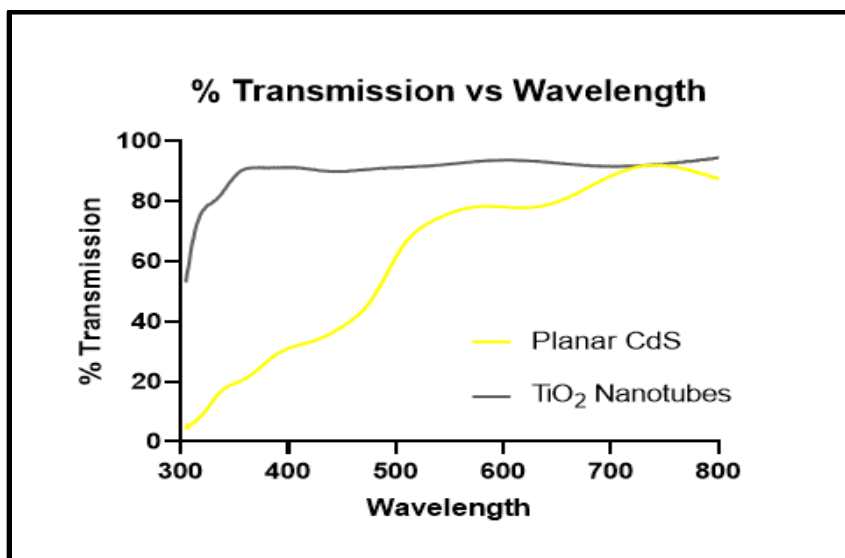


Figure 3.7 Transmission Curve generated from UV-Vis Spectroscopy data for Planar CdS and TiO₂ nanotubes with a porosity of 32%.

CHAPTER 4. HOST NANO-POROUS TEMPLATE – TITANIA NANOTUBES

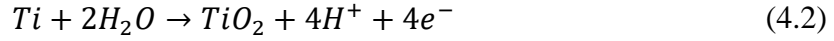
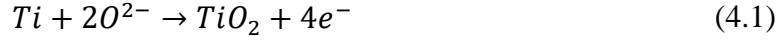
4.1 Nanoporous Titania

Titanium dioxide is one of the most studied metal oxides. It is also one of the most explored nanomaterial based on transition metal oxides. Highly oriented vertically oriented Titania nanotubes find its place in a variety of applications due as they provide large surface to volume ratio, vertically aligned surface, excellent charge transfer properties in nanomaterials mainly governed by the quantum confinement phenomenon. Various methods have been evolved for fabricating TiO_2 nanotubes including hydro/ solvothermal techniques, template-assisted methods, seed growth method, sol-gel method and electrochemical oxidation method.

Among these direct electrochemical oxidation turns out to be simplest and cheapest way to fabricating TiO_2 nanotubes. Zwilling et al. demonstrated that anodic oxidation of Titanium foil leads to the formation of self-organized nanotubular structures of Titanium dioxide [23]. Direct oxidation provides a controllable method of adjusting the shape, size and the degree of order of the resulting in the formation of self-organized nanostructures. Depending on the process parameters, direct oxidation of Titanium surface leads to the formation of a compact structure, ranging from random porous structure to tubular structure.

Porous Titania nanotubes can be fabricated by anodization of Titanium either in acidic electrolytes or in basic electrolytes, either under potentiostatic or galvanostatic conditions. Potentiostatic anodization is more widely used for the fabrication of self-ordered porous Titania nanotubes. During potentiostatic anodization of Titanium, under

constant anodic potential a thin compact barrier oxide layer starts to grow over the Titanium surface.



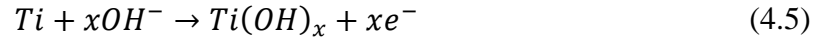
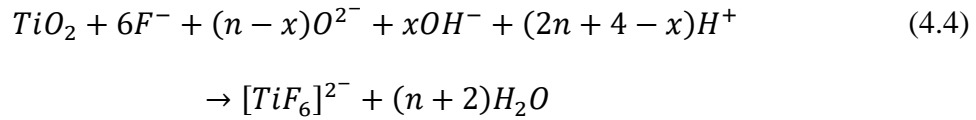
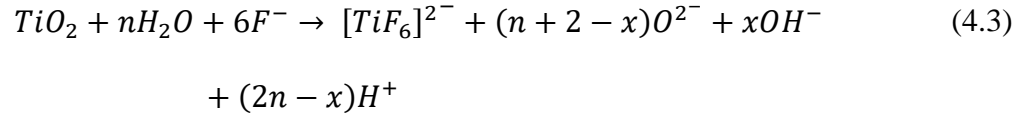
The fabrication of Titania nanotube using anodic oxidation of Titanium has been proposed to involve various stages of reactions [24] leading to the formation self-organized nanostructures: (i) formation of oxide layer, (ii) pore formation and deepening of the pores, (iii) incorporation of adjacent smaller pores into bigger pores, (iv) early nanotube array formation and (v) formation of perfect nanotube array.

During the first stage of anodization the series resistance of the anodization circuit increases over time with the thickening of the initial barrier oxide layer. After reaching a certain thickness of the barrier oxide layer the current drops rapidly to reach a minimum value which is the onset of second stage of anodization (pore initiation stage). For this stage, the current concentrates on local imperfections existing on the initial barrier oxide layer, resulting in non-uniform oxide thickening and pore initiation at the thinner oxide areas [25].

Pore initiation in the growing anodic oxide starts as a result of morphological instability. Pores develop from initial pits following the etching of the fluorine ion species penetrating closer to the metal/ oxide interface. As the field-assisted fluorine ions starts to etch the Titanium dioxide film more and more, the smaller pores start to merge and form bigger pores. The process continues until an equilibrium is established between the

formation of Titanium dioxide and the etching of Titanium dioxide film, resulting in the formation of perfectly well-aligned self-organized Titania nanotubes.

Nanotubular films of TiO_2 fabricated in aqueous inorganic fluorine sources are formed through the etching action of TiO_2 by fluorine ions



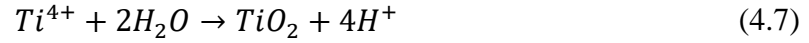
Where, n is used to describe the disassociation rate of water to dissolution of TiO_2 and x is used to describe the ratio of Titanium Hydroxides to TiO_2 .

The balance in the movement rates of the metal/ oxide interface and the oxide/ electrolyte interface governs the steady state pore growth and is achieved by a balance in the dynamic equilibrium between the oxide dissolution at the oxide/ electrolyte interface and formation of oxide at the metal/ oxide interface. Several theories have been proposed to explain the steady-state pore formation mechanism such as average field model, Joule's heat-induced chemical dissolution model, field-assisted oxide dissolution model, direct cation ejection mechanism and flow model.

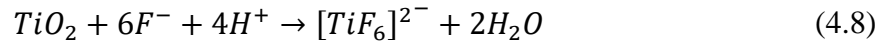
Oxidation of Titanium



Anodic Oxidation



Chemical Dissolution



The most widely accepted theory for the Titania nanotube formation is the field assisted oxide dissolution model [26, 27], which explains the early stage of the anodization is breakdown of the TiO_2 layer via the electric field. The balance between the oxide formation, electric field driven inward movement of O^{2-} ions and the outward migration of Ti^{+} ions at the metal/ oxide interface, and the oxide dissolution maintains the barrier oxide layer thickness. The ordering of pores is influenced by the magnitude of electrostatic stress that is developed along the direction of the electric field as a result of the resistance encountered due to the counter migration and attraction of the ions. Tubular TiO_2 nanostructures of various lengths, pore diameters and wall thickness can be formed based on optimal anodization parameters and solution composition.

4.2 Parameters influencing the formation of Titania Nanotubes by anodic oxidation

The formation of Titania nanotubes using anodic oxidation of Titanium is influenced by the electrolyte, water content, anodization voltage, electrodes, aged electrolyte, anodization time, electrolyte temperature and the electrolyte pH.

4.2.1 Effect of electrolyte on anodic oxidation of Titanium

The nanotube array formation is significantly influenced by the composition and concentration of the electrolyte used. There are four different generations of electrolyte used for fabricating TiO₂ nanotube arrays using anodic oxidation of Titanium. The first generation of electrolyte used for fabricating TiO₂ nanotube arrays were based on hydrofluoric acid (HF)-based aqueous electrolytes. The relatively low pH in HF aqueous solution electrolytes limited the length of the TiO₂ nanotubes. High acidity of HF electrolytes results in rapid dissolution of TiO₂. The maximum nanotube length achieved using the first generation of electrolyte was restricted to approximately 500nm [28-30].

The second generation used buffered electrolytes of citric acid or sodium sulfate by adding weaker acids such as KF or NaF into buffered solution, also the pH was adjusted to weakly acidic by addition of sulfuric acid or sodium hydroxide. By adjusting the pH to weakly acidic of the electrolyte the nanotube of length approximately 4.4μm were achieved [31]. In the second generation of electrolytes the pH interferes the electrochemical etching and chemical dissolution leading to much longer nanotubes in acidic solutions.

The third-generation electrolytes used viscous polar organic electrolytes such as glycerol, ethylene glycol, diethylene glycol, dimethyl sulfoxide (DMSO) in NH₄F, NaF

and KF based fluoride media. The pore diameter in the third-generation electrolyte can be influenced significantly by adjusting the fluoride ion concentration in the electrolyte. Titania nanotube arrays with approximately 1000 μ m long were formed in ethylene glycol containing 0.6 wt% NH₄F and 3.5% water anodized at 60V for 216hr [32]. Ethylene glycol electrolyte containing water and fluoride ions leads to double walled nanotube structures [33].

The fourth-generation electrolytes use non fluoride-based electrolytes grow TiO₂ nanotube arrays. Hydrochloric acid, Hydrogen peroxide, and their mixtures, Sodium Chloride, perchloric acid solution and their mixtures and mixtures of Oxalic acid, formic acid and sulfuric acid in ammonium chloride are used to replace the fluoride ions by chloride ions to fabricate well-developed nanotube arrays [34,35-37]. For hydrochloric acid-based electrolytes the only 3 M of acid concentration leads to the formation of nanotube arrays [35].

4.2.2 Effect of water content on ethylene glycol based Titania nanotubes

The reproducibility of the formation of well-ordered Titania nanotube arrays in a two-electrode configured anodization is affected by the water content of the electrolyte, especially when the anodization is carried out for a shorter period of time. The initial water content in the electrolyte is the key to getting reproducible results. The limiting anodization potential can be varied by varying the water content in ethylene glycol-based electrolyte. The initial current density in anodization decreases as the water content in the electrolyte increases. A minimum of 0.18 wt% of water is required to form well-ordered Titania nanotube arrays [38]. When the water content is greater than 0.5 wt%, the amount of ridges

on the circumference of the nanotubes increased [38]. The key to achieve very long nanotubes is limiting the water content $< 5\%$ in the anodization bath [39].

The photoelectrochemical properties of Titania nanotubes can be modified by varying the water content of the anodization electrolyte. Maximum photon to current conversion efficiency was achieved using 10 wt% water in ethylene glycol based Titania nanotubes, however, the higher water content in the electrolyte lead to ridged structures of TiO_2 nanotubes that are completely separate from each other [40].

4.2.3 Effect of anodization voltage

Anodization voltage is a critical parameter that strongly influences the pore diameter and the interpore distance. Well-ordered TiO_2 nanotubular structures can be grown by applying a suitable range of voltage, below the limiting anodization potential, across the electrodes. Various studies have been performed to study the effect of applied voltage on the growth of TiO_2 nanotubes. Z. Lockman et al. observed that the pore diameter and the nanotube length increased with the increase in the anodization potential [41]. After a certain point further increase in anodization potential lead to the deterioration of the nanotubular structure forming a spongy-like structure or just randomly porous TiO_2 .

Y. Alivov et al. reported that the anodization potential does not have any clear dependence on the pore diameter of the TiO_2 nanotubes in glycerol-based electrolyte when the anodization voltage was varied over the range of 10-240V. The average pore diameter of 220nm was obtained for 10V, while, the samples grown at 30V, 60V and 120V had the average pore diameter of 86nm, 156nm and 75nm respectively [42].

4.2.4 Effect of electrodes

A variety of electrode materials have been used as the cathode material in the formation of TiO₂ nanotubes including Ni, Pd, Pt, Fe, Co, Cu, Ta, W, C, Al and Sn in both aqueous and ethylene glycol electrolytes [43]. Different cathode material affects the dissolution kinetics of the Titanium anode leading to formation of TiO₂ nanostructures of different morphologies. The electrical conductivity of the electrolyte increases with the amount of Titanium dissolved in the solution which in turn helps to prevent the debris formation.

The aspect ratio of the TiO₂ nanotubes vary significantly with the use of different cathode material as counter electrode. Sreekantan et al. used iron, carbon, stainless steel and aluminum as the counter electrodes and observed that TiO₂ nanotubes formed using stainless steel counter electrode produced shorter tube lengths that were conical in shape and are unstable while TiO₂ nanotubes formed using iron counter electrode produced well-organized nanotubes of the higher aspect ratio is obtained [44].

4.2.5 Effect of aged electrolyte

Aged ethylene glycol electrolyte when reused leads to the formation of nanotubes with reasonable quality (i.e. without unwanted debris, or porous oxide layers on the top of the nanotube layer) [45]. Longer nanotubes are obtained in the solution that was previously used to perform anodization. The breakdown potential, after which no ordered nanotubular structures are obtained, increases with the aging of the electrolyte [46]. However, when the solution is really aged leads to the formation of passive oxide layer instead of nanotubular structure suggesting the depletion of the in F^- and H^+ ions.

Aged electrolytes used for subsequent anodization leads to the formation low aspect ratio nanotube arrays. In aged electrolyte subsequent anodization take longer time to completely anodize same thickness of Titanium samples. The pore diameter increases while the final nanotube length decreases in aged electrolyte than in fresh electrolyte when anodization is performed in otherwise similar anodization conditions.

4.2.6 Effect of anodization time

Anodization time greatly influences the formation mechanism of TiO_2 nanotube formation. Too short of anodization does not lead to any nanotube formation. The dimensions of the TiO_2 nanotubes increases by extending the anodization time, however, the average growth rate decreases [47]. Longer anodization time leads to the formation of rough and cross-linked structure is seen where TiO_2 nanotubes are clustered in groups or bundles while shorter anodization time results in the formation of more organized TiO_2 nanostructure [48]. Prolonging the anodization leads to the collapse of the nanotubular structures starting with the thinning of tube walls due over dissolution of the tubes by the fluoride ions.

4.2.7 Effect of electrolyte temperature

The rate of oxide growth, structural formation and the quality of TiO_2 nanotubes is directly influenced by the electrolyte temperature. The electrolyte temperature has a significant impact on the dimensions (pore diameter and the wall thickness) of the nanotubes formed in viscous non aqueous electrolytes, the nanotube size reduces with the reduction in the electrolyte temperature, while in aqueous electrolytes the impact of electrolyte temperature was insignificant [49].

However, Grzegorz D. Sulka et al. observed that the highest values of inner pore diameter, pore circularity and the regularity in the pore arrangement are observed at an optimal electrolyte temperature and applied potential of 20°C and 50V [50]. When the electrolyte temperature was increased to 30°C smaller pore diameters, smaller pore circularities and a weaker pore arrangement was seen [51].

4.2.8 Effect of electrolyte pH

The electrolyte pH in electrochemical anodization is an important parameter that directly influence the formation of TiO₂ nanotube structure by anodic oxidation of Titanium. The fluoride ion concentration and the solution acidity determine the rate of chemical dissolution of titania in the solution. The chemical dissolution increases with the increase in F^- and H^+ concentration in the electrolyte. The acid in the electrolyte increases the chemical dissolution as well as reduces the viscosity of the solution leading to fast formation of Titania nanotubes.

The lower pH of the solution is known to prolong the time required to establish equilibrium the dissolution rate and the rate of nanotube growth which in turn results in increased pore diameter of the nanotubes [52]. The lower pH leads to increased pore diameter but gives less ordered TiO₂ nanotubes than that formed in pH neutral solutions. Varying the pH from strongly acidic (pH<1) to weakly acidic (pH 4.5) increases the nanotube length from 0.56 µm to 4.4 µm in otherwise similar anodizing conditions [53].

The wall thickness is increased as the pH increases up to pH value of 10 above that the wall thickness, the pore diameter and the structural order of the nanotube decreases gradually resulting in the formation of unwanted debris [53]. The lower pH values produce shorter and cleaner nanotubes.

CHAPTER 5. NUMERICAL PROCEDURES AND SCAPS SIMULATION

SCAPS is a one-dimensional solar cell simulation program, originally developed for cell structures of the CuInSe_2 and the CdTe family. The program has evolved its capabilities over time making it suitable for simulating crystalline solar cells (Si and GaAs family) and amorphous cells (a-Si and micromorphous Si) [54]. SCAPS allows to add up to seven semiconductor layers, E_g , χ , ϵ , N_C , N_V , v_{thn} , v_{thp} , μ_n , μ_p , N_A , N_D , all traps (defects) N_t can be graded for each semiconductor layer. The different recombination mechanisms included are band-to-band (direct), Auger, SRH-type. Intra band tunneling, tunneling to and from interface states can be accounted for in the program.

A variety of illumination spectra are included, and it can also be supplied by the user. The illumination can be from either the p-side or the n-side, also, allowing for spectrum cut-off and attenuation. The generation is either calculated from the specified illumination spectrum or can be user specified. The program calculates energy bands, concentrations and currents at a given working point (voltage, frequency, temperature), J-V characteristics, ac characteristics, spectral response. SCAPS also has a built-in curve fitting feature and also a panel for the interpretation of admittance measurements.

In SCAPS the only variables to have explicit temperature dependence are the effective density of states of the conduction band, the effective density of states of the valence band, the thermal velocities, the thermal voltage and all their derivatives. The user must specify the other corresponding material parameters for each T for other variables. The working point voltage is the dc-bias voltage used in C-f simulation and in $QE(\lambda)$ simulation. The working point frequency the frequency at which the C-V measurement is simulated.

5.1 The Physical Model

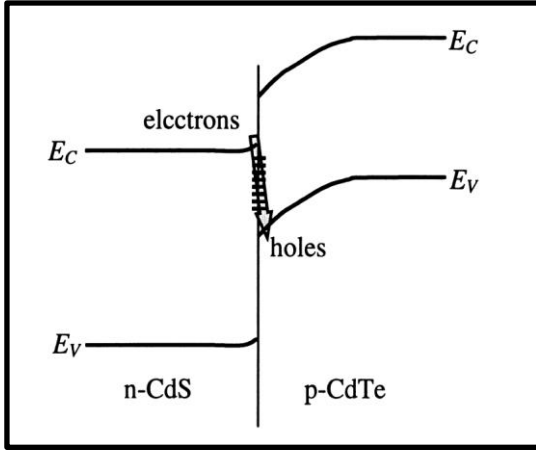


Figure 5.1 Pauwells Vanhoutte Model for CdS/CdTe heterojunction

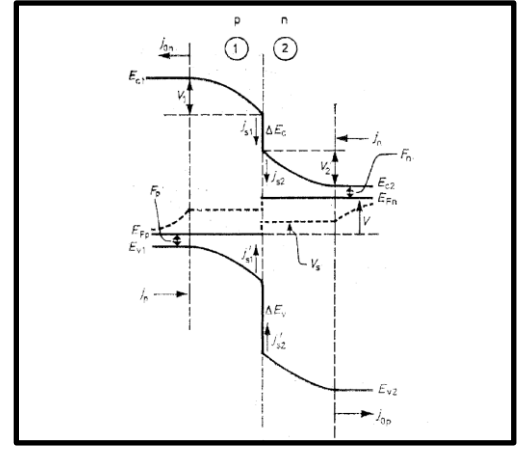


Figure 5.2 p-n heterojunction interface showing bending and discontinuities in bands

The physical model in SCAPS is based on Pauwells Vanhoutte model [55]. The figure 5.1 shows the interface recombination as the dominant recombination path between the window electrons and the absorber holes. Pauwells Vanhoutte model considers the interface recombination and arbitrary energy barriers at the interface to find the optimum structure for a heterojunction solar cell.

The model is based on the various underlying assumptions as stated: (i) The generation and recombination of carriers in the space charge region is neglected. (ii) Thermionic emission is considered as the majority carrier transport mechanism in the space charge region and it was assumed that at the interface one type of carriers are the majority carriers. (iii) Interface recombination allows for the exchange of electrons and holes from both conduction bands to the valance bands of both the semiconductors at the interface and

it was assumed that one of the semiconductors is much more heavily doped than the other. (iv) Tunnelling at the interfaces or at the is neglected. (v) Analysis of efficiency is on the basis of current-voltage characteristics.

The model, at the interfaces, allows for the discontinuities in (i) the quasi-fermi levels, (ii) the energy bands E_c and E_v , and (iii) the bandgap E_g ; for the interface recombination to occur. Interface recombination is described by the extension of SRH formalism. At the interfaces the electrostatic potential is assumed to be continuous. Thermionic emission is used to derive the relation between fermi level discontinuity, carrier concentrations and current. For direct bandgap semiconductors with identical effective masses, the thermionic emission current for the electrons is given by

$$J_{th\ n} = v_{th\ n} \left(n_1 \exp\left(-\frac{|\Delta E_c|}{kT}\right) - n_2 \right) \quad (5.1)$$

Where, $J_{th\ n}$ is the particle current from semiconductor 1 to 2, $v_{th\ n}$ is the thermal velocity of electrons, n_1 and n_2 are the electron concentrations and ΔE_c is the discontinuity in the conduction band. Thermionic emission current for holes can be computed similarly.

In SCAPS for each layer, the type and density of on shallow level and up to three deep levels can be defined. The shallow level is completely ionized and does not contribute to recombination. Transport of majority carriers and the minority carriers at the contacts is described by thermionic emission and the surface recombination velocities respectively. Boundary conditions are imposed on the continuity equation for the electrons at the metal semiconductor contact

$$J_n = S_n(n - n_{eq}) \quad (5.2)$$

$$S_n = \frac{A^* T^2}{q N_c} = v_{th} n \quad (5.3)$$

Where, n_{eq} is the equilibrium electron concentration at the contact, S_n is the surface recombination velocity of electrons and A^* is the effective Richardson constant.

Figure 5.2 shows the p-n heterojunction interface, where V_1 and V_2 are the band bendings in the space charge regions of the p-type and the n-type semiconductor respectively, ΔE_c and ΔE_v are the discontinuities in the bands, E_{Fn} and E_{Fp} are the quasi-fermi levels under forward bias V . j_n, j_{s2}, j_{s1} and j_{0n} are electron particle current densities respectively entering the space charge region of the n-type material, recombining from the conduction bands 1 and 2 at the interface, and leaving the space charge region of the p-type material. The quantities j_p, j_{s1}', j_{s2}' and j_{0p} are hole particle current densities defined analogously. F_n and F_p determine the doping concentrations.

The difference in electron-affinities of both materials determines the jump ΔE_c in the bottom of the conduction bands of the two semiconductors at the interface. ΔE_v is the jump in the top of the valence bands in the two semiconductors. $\Delta E_v = \Delta E_c + \Delta E_g$ where $\Delta E_g = E_{g2} - E_{g1}$ is the difference in the bandgaps of the two semiconductors. ΔE_c and ΔE_v can be positive or negative.

Using the Pauwels Vanhoutte model, it was concluded that for the heterojunctions the semiconductor with the smaller bandgap should have good quality, i.e., it should have larger collection efficiency; it should absorb all photons. Best efficiencies are obtained for three type of device structures. In the first type, the weakly doped semiconductor should

have an optimum bandgap, it should be inverted at the interface, and the strongly doped semiconductor should have a larger bandgap. In the second type, the strongly doped semiconductor must have an optimum bandgap and the discontinuity at the interface in its minority carrier band must approach zero from the positive side, i.e. it may not constitute a barrier for the collection of minority carriers. The third type has the characteristics of the first type, but the strongly doped semiconductor has the smaller bandgap.

5.2 SCAPS 1-D Simulation Procedures

SCAPS-1D was used for simulating the J-V characteristics of nanowire CdS-CdTe solar cell. Basic Working procedures for SCAPS-1D is explained with the help of figures 5.3-5.10.

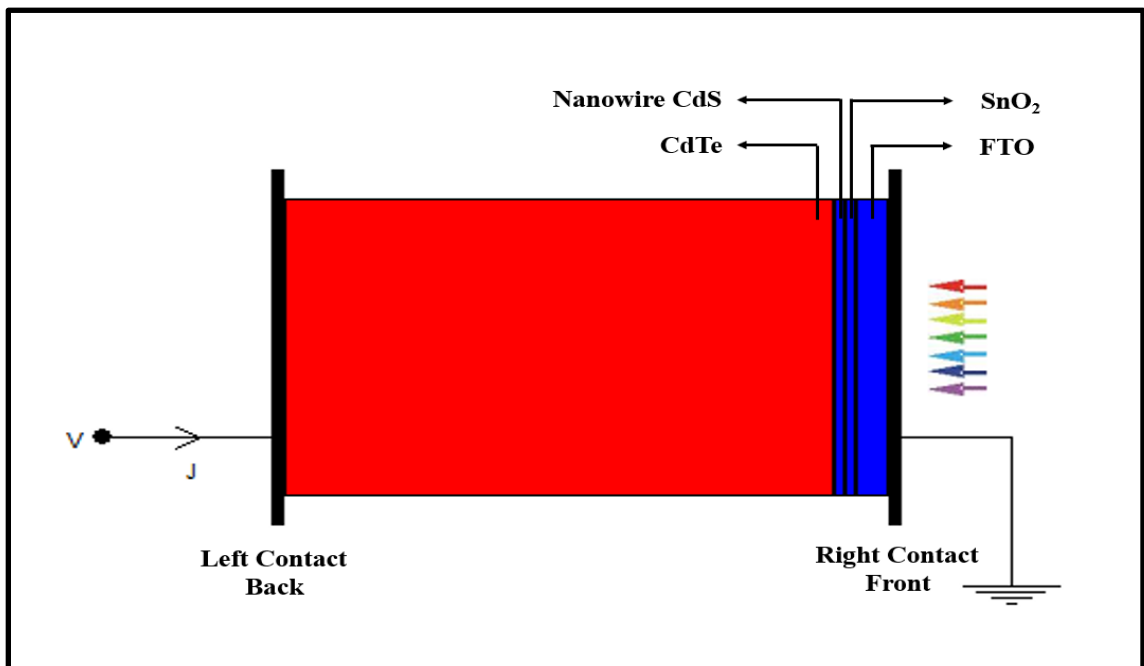


Figure 5.3 Solar Cell Definition

Figure 5.3 shows the Solar cell structure screenshot taken from the SCAPS Solar cell definition panel. In SCAPS the p-side must be connected to the left contact in order to form

a p-n junction due to the fact that n-p junction simulated in SCAPS leads to non-uniform current which in turn is much less stable. SCAPS simulation program was used to simulate window/ absorber type CdS/ CdTe solar cell. The p-side semiconductor used for simulation is 5 μm CdTe which acts as the absorber layer, while the n-side in 200nm Nanowire CdS which acts as window layer. 100nm of intrinsic SnO_2 , which acts as a buffer layer, was included to perform simulations for simulate for the actual device design used in our lab. The solar cell is illuminated from the right side.

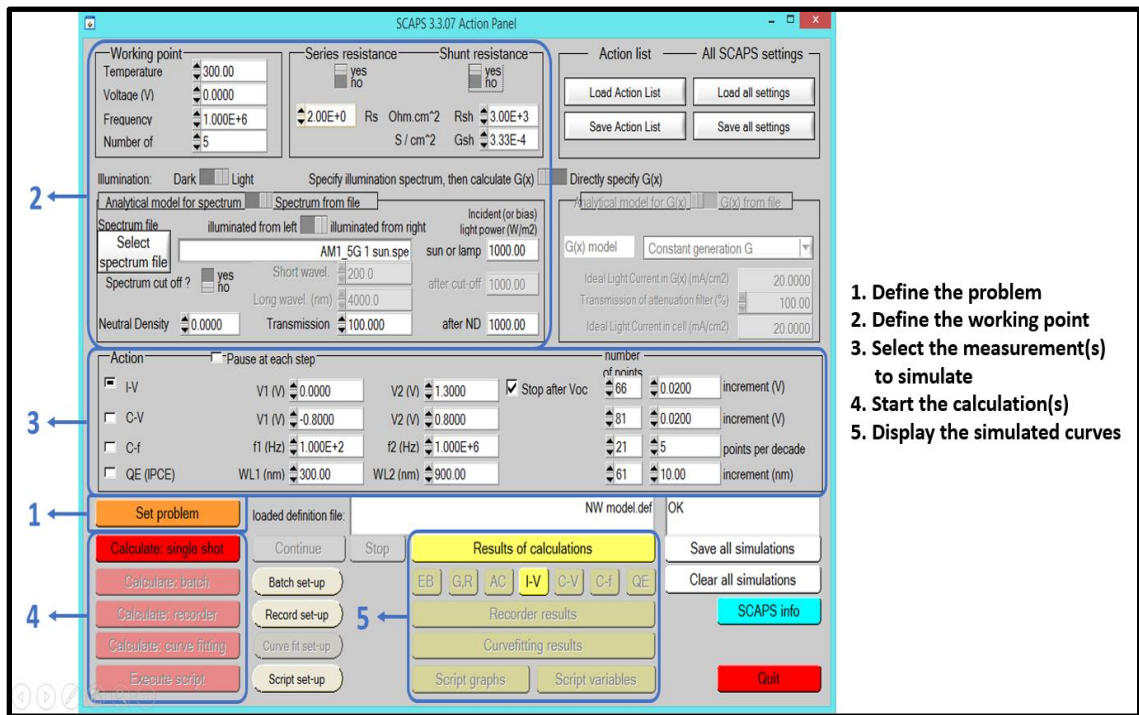


Figure 5.4 SCAPS: Action Panel

Figure 5.4 shows the SCAPS start-up panel is the Action panel. The action panel consists of 5 blocks: Block 1 defines the problem; block 2 defines the working points; block 3 lets the user to select the measurement(s) to simulate from I-V, C-V, C-f and $\text{QE}(\lambda)$; block 4 is for starting the calculation which can either be a single shot calculations or a batch and the calculations can be recorded; and block 5 displays the simulated curve(s).

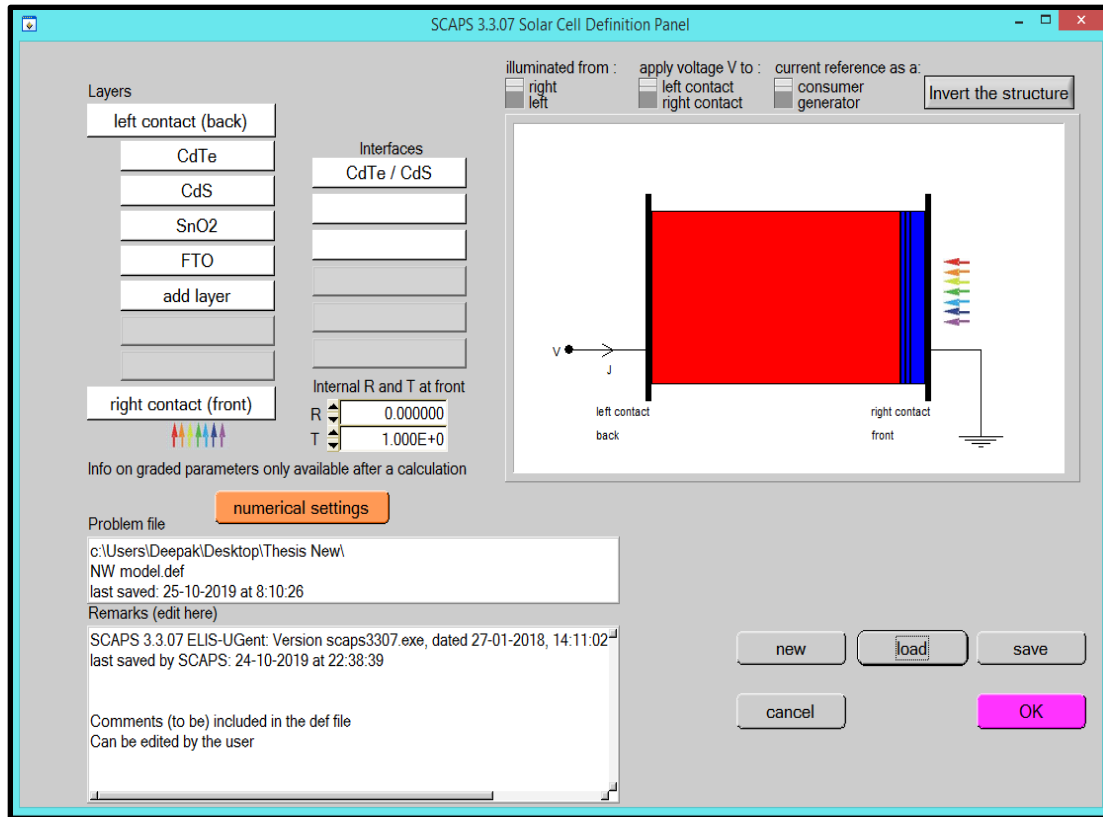


Figure 5.5 SCAPS: Solar Cell Definition Panel

Figure 5.5 shows the Solar cell definition panel. The user can define up to 7 semiconductor layers. For each layer, specific parameters need to be provided. The contact, layer and interface properties can be added by clicking appropriate boxes. The conventions for the Voltage and Current in the external contacts can be user defined.

The SCAPS program is optimized for p-n junctions and is less stable for n-p junctions (n-p junctions lead to non-uniform current), that means the p-side should be kept to the left and the n-side should be kept to the right. Interface layer can be defined between any two layers. The user can save a model to file or load a model from an already saved file. The program also provides the flexibility of illumination either from the left or from the right.

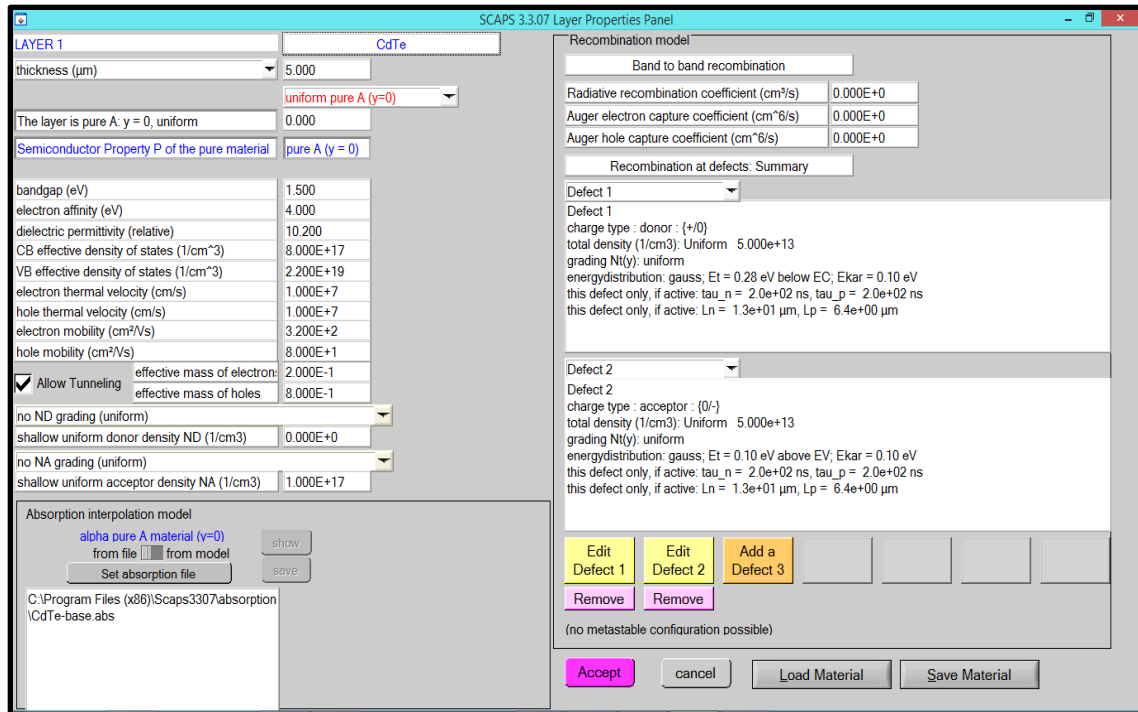


Figure 5.6 SCAPS: Layer Properties Panel

Figure 5.6 shows the Layer Properties Panel where various material properties of the semiconductor need to be specified. The various parameters that needs to be supplied includes the thickness, the bandgap, electron affinity, dielectric permittivity, effective density of states for the conduction band and the valence band, thermal velocity of electron and holes, electron and hole mobilities, effective mass of electrons and holes if tunneling is allowed, and shallow acceptor/ donor density of the semiconductor material.

The absorption interpolation model can be selected from the default absorption models for various semiconductor in SCAPS or can be loaded from a file if the user has the absorption model for particular semiconductor material. Band to band recombination mechanism can be allowed by providing the Radiative recombination coefficient, Auger electron capture coefficient and Auger hole capture coefficient.

SCAPS 3.3.07 Defect Properties Panel

Defect 1 of CdTe

defect type	Single Donor (0/+)
capture cross section electrons (cm ²)	1.000E-14
capture cross section holes (cm ²)	1.000E-14
energetic distribution	Gauß
reference for defect energy level Et	Below EC
energy level with respect to Reference (eV)	0.280
characteristic energy (eV)	0.100

no Nt grading (uniform)

Nt total (1/cm3)	uniform Nt	5.000E+13
Nt peak (1/eV/cm3)	uniform Nt	2.821E+14

Optical capture of electrons ☐ From model ☒ From file

refractive index (n)	3.000
effective mass of electrons (rel.)	1.000E+0
effective field ratio	1.00E+0
cut off energy (eV)	10.00
optical electron capture cross sections file:	

Optical capture of holes ☐ From model ☒ From file

refractive index (n)	3.000
effective mass of holes (rel.)	1.000E+0
effective field ratio	1.00E+0
cut off energy (eV)	10.00
optical hole capture cross sections file:	

accept cancel

Figure 5.7 SCAPS: Defect Properties Panel

Defect properties panel, shown in figure 5.7, opens on clicking on “Add a defect” button on the Layer properties panel. Up to seven defects can be added to each semiconductor layer. The defect can be neutral, acceptor-type and donor-type and the defects can also be multivalent defects. The defect energetic distribution can be Single, Uniform, Gauss, CB tail and VB tail. The reference to energy defect level has to be specified by the user and which can be above E_v , below E_c and above E_i . Optical capture of electrons and/or holes can also be allowed.

Right Contact (Front)

Electrical properties

Thermionic emission / surface recombination velocity (cm/s) :

electrons

holes

Metal work function (eV) or ☐ **flat bands**

Majority carrier barrier height (eV) :

relative to EF

relative to EV or EC

☐ Allow contact tunneling

Effective mass of electrons

Effective mass of holes

Optical properties

optical filter ☒

Filter Mode reflection

From Value

From File

Complement of Filter

Select Filter File

OK cancel

Figure 5.8 SCAPS: Contact Panel

Figure 5.8 shows the Contact properties panel. Clicking on either the front or the back contact on the Solar cell definition panel opens the contact properties panel. Electrical and Optical properties can be edited in the contact panel. The user can provide the metal work function ϕ_m (for majority carriers). The user can also choose the flat band option in which case the metal work function is calculated for every temperature in such a way that the flat band condition prevails. Majority carrier barrier height relative to the fermi level and conduction/ valence band is calculated. Tunneling of electrons and holes through the contact can be allowed.

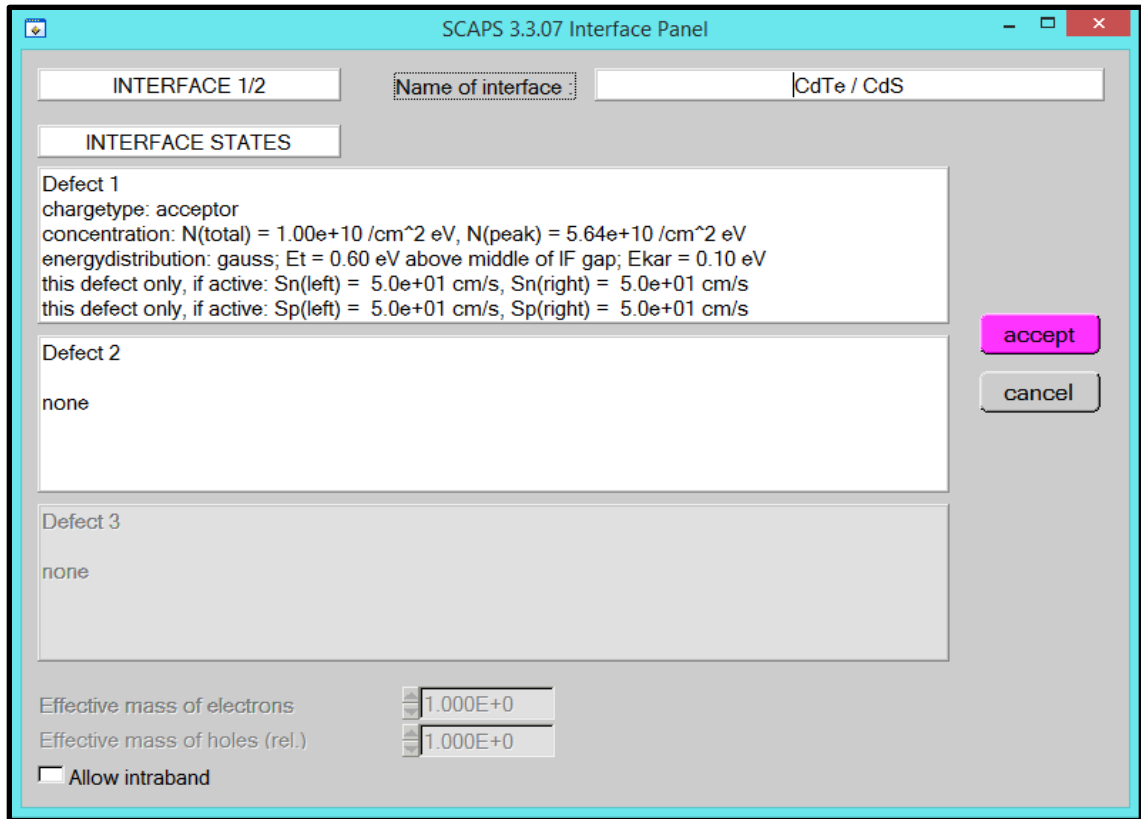


Figure 5.9 SCAPS: Interface Panel

Figure 5.9 shows the Interface panel which can be added between two semiconductor layers by clicking on the Interfaces button on the Solar cell definition panel. The interface transport model used in SCAPS is based on the thermionic emission mechanism. The smallest thermal velocity of the two neighboring layers is equal to the thermal velocity of the interface transport. There can only be 3 possible interface defects and their charge type cannot be multivalent. Interface recombination is based on Pauwels-Vanhoutte theory [55]. Intraband tunneling also be allowed between the interface of two semiconductor layer.

The tables below list the parameters used in SCAPS simulations.

Table 5.1 Back contact material properties

Back Contact	Parameter		Value
	Thermionic Emission/ surface recombination velocity (cm/s)		
	(i)	electrons	1.00E+5
	(ii)	holes	1.00E+7
	Metal Work Function		5.5000
	Majority Carrier barrier height(eV)		
	(i)	relative to E_f	0.0000
	(ii)	relative to E_v	-0.1397

Table 5.2 CdTe material properties

CdTe	Parameter		Value
	Thickness (μm)		5.000
	Bandgap (eV)		1.500
	Electron Affinity (eV)		4.000
	Dielectric Permittivity (relative)		10.200
	CB Effective Density of States ($1/\text{cm}^3$)		8.000E+17
	VB Effective Density of States ($1/\text{cm}^3$)		2.200E+19
	Electron Thermal Velocity (cm/s)		1.000E+7
	Hole Thermal Velocity (cm/s)		1.000E+7
	Electron Mobility (cm^2/Vs)		3.200E+2
	Hole Mobility (cm^2/Vs)		8.000E+1
	Allow tunneling		
	(i)	Effective mass of electrons	2.000E-1
	(ii)	Effective mass of holes	8.000E-1
	Shallow Uniform Acceptor Density N_A ($1/\text{cm}^3$)		1.000E+17

Table 5.3 Donor type defect parameters in CdTe

Defect 1 of CdTe	Parameter		Value
	Defect Type		Single Donor
	(i)	Capture Cross Section Electrons (cm ²)	1.000E-14
	(ii)	Capture Cross Section Holes (cm ²)	1.000E-14
	Energetic Distribution		Gauß
	(i)	Reference for defect energy level E _t	Below E _C
	(ii)	energy level w.r.t Reference (eV)	0.280
	(iii)	characteristic energy (eV)	0.100
	N _t total (1/cm ³) uniform		5.000E+13
	N _t peak (1/eV/cm ³) uniform		2.821E+14

Table 5.4 Acceptor type defect parameters in CdTe

Defect 2 of CdTe	Parameter		Value
	Defect Type		Single Acceptor
	(i)	Capture Cross Section Electrons (cm ²)	1.000E-14
	(ii)	Capture Cross Section Holes (cm ²)	1.000E-14
	Energetic Distribution		Gauß
	(i)	Reference for defect energy level E _t	Above E _v
	(ii)	energy level w.r.t Reference (eV)	0.100
	(iii)	characteristic energy (eV)	0.100
	N _t total (1/cm ³) uniform		5.000E+13
	N _t peak (1/eV/cm ³) uniform		2.821E+14

Table 5.5 CdTe / CdS Interface parameters

Parameter		Value
Defect Type		Acceptor
(i)	Capture Cross Section Electrons (cm ²)	5.00E-16
(ii)	Capture Cross Section Holes (cm ²)	5.00E-16
Energetic Distribution		Gauß
(i)	Reference for defect energy level E _t	Above middle of interface gap
(ii)	energy level w.r.t Reference (eV)	0.600
(iii)	characteristic energy (eV)	0.100
N _t total (1/cm ³) uniform		1.00E+10
N _t peak (1/eV/cm ³) uniform		5.64E+10
Allow Tunneling to Interface States		
(i)	Relative mass of electrons	2.000E-1
(ii)	Relative mass of holes	8.000E-1

Table 5.6 CdS material properties

		Parameter	Value
CdS	Nanowires	Thickness (μm)	0.200
		Bandgap (eV)	3.200
		Electron Affinity (eV)	4.100
		Dielectric Permittivity (relative)	9.000
		CB Effective Density of States ($1/\text{cm}^3$)	2.300E+18
		VB Effective Density of States ($1/\text{cm}^3$)	1.700E+19
		Electron Thermal Velocity (cm/s)	1.000E+7
		Hole Thermal Velocity (cm/s)	1.000E+7
		Electron Mobility (cm^2/Vs)	1.000E+2
		Hole Mobility (cm^2/Vs)	2.500E+1
		Allow tunneling	
		(i) Effective mass of electrons	2.000E-1
		(ii) Effective mass of holes	8.000E-1
		Shallow Uniform Donor Density N_D ($1/\text{cm}^3$)	1.000E+18

Table 5.7 Acceptor type defect parameters in CdS

Defect 1 of CdS	Parameter		Value
	Defect Type		Single Acceptor
	(i)	Capture Cross Section Electrons (cm ²)	1.000E-14
	(ii)	Capture Cross Section Holes (cm ²)	1.000E-14
	Energetic Distribution		Single
	(i)	Reference for defect energy level E _t	Above E _i
	(ii)	energy level w.r.t Reference (eV)	0.000
	N _t total (1/cm ³) uniform		1.000E+16

Table 5.8 SnO₂ material properties

SnO₂	Parameter	Value
	Thickness (μm)	0.100
	Bandgap (eV)	3.600
	Electron Affinity (eV)	4.500
	Dielectric Permittivity (relative)	9.000
	CB Effective Density of States (1/cm ³)	3.200E+18
	VB Effective Density of States (1/cm ³)	2.500E+19
	Electron Thermal Velocity (cm/s)	1.000E+7
	Hole Thermal Velocity (cm/s)	1.000E+7
	Electron Mobility (cm ² /Vs)	1.000E+2
	Hole Mobility (cm ² /Vs)	2.500E+1
	Shallow Uniform Donor Density N _D (1/cm ³)	1.000E+18

Table 5.9 Neutral type defect parameters in SnO₂

Defect 1 of SnO₂	Parameter		Value
	Defect Type		Neutral
	(i)	Capture Cross Section Electrons (cm ²)	1.000E-15
	(ii)	Capture Cross Section Holes (cm ²)	1.000E-13
	Energetic Distribution		Gauß
	(i)	Reference for defect energy level E _t	Above E _i
	(ii)	energy level w.r.t Reference (eV)	0.000
	(iii)	characteristic energy (eV)	0.100
	N _t total (1/cm ³) uniform		1.000E+15
	N _t peak (1/eV/cm ³) uniform		5.642E+15

Table 5.10 FTO material properties

FTO	Parameter	Value
	Thickness (μm)	0.300
	Bandgap (eV)	3.600
	Electron Affinity (eV)	4.800
	Dielectric Permittivity (relative)	9.000
	CB Effective Density of States ($1/\text{cm}^3$)	3.200E+18
	VB Effective Density of States ($1/\text{cm}^3$)	2.500E+19
	Electron Thermal Velocity (cm/s)	1.000E+7
	Hole Thermal Velocity (cm/s)	1.000E+7
	Electron Mobility (cm^2/Vs)	3.000E+1
	Hole Mobility (cm^2/Vs)	7.500E+0
	Shallow Uniform Donor Density N_D ($1/\text{cm}^3$)	5.000E+20

Table 5.11 Neutral type defect parameters in FTO

Parameter		Value
Defect Type		Neutral
(i)	Capture Cross Section Electrons (cm ²)	1.000E-15
(ii)	Capture Cross Section Holes (cm ²)	1.000E-12
Energetic Distribution		Gauß
(i)	Reference for defect energy level E _t	Above E _i
(ii)	energy level w.r.t Reference (eV)	0.000
(iii)	characteristic energy (eV)	0.100
N _t total (1/cm ³) uniform		1.000E+15
N _t peak (1/eV/cm ³) uniform		5.642E+15

Table 5.12 Front contact material properties

Front Contact	Parameter		Value
	Thermionic Emission/ surface recombination velocity (cm/s)		
	(i)	electrons	1.00E+5
	(ii)	holes	1.00E+6
	Metal Work Function		4.4000
	Majority Carrier barrier height(eV)		
	(i)	relative to E_f	-0.4000
	(ii)	relative to E_v	-0.2692

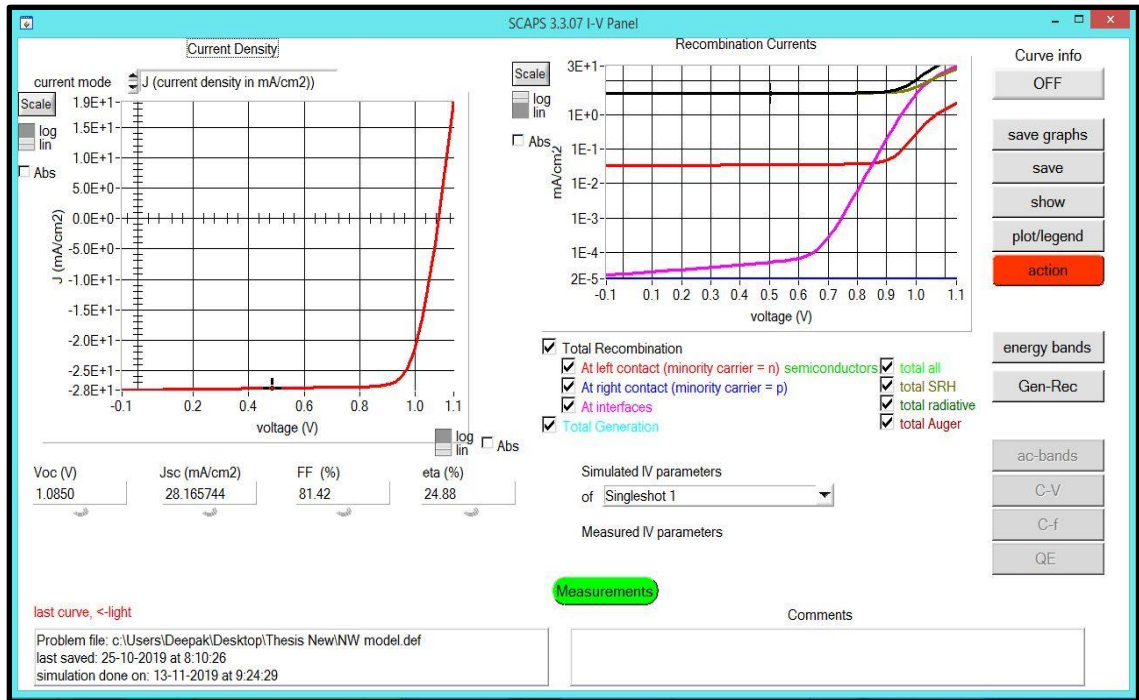


Figure 5.10 SCAPS: I-V Panel

Figure 5.10 shows the results of the Simulated J-V characteristics at 300 K for the parameters shown in Table 5.1 – 5.12. in SCAPS

CHAPTER 6. RESULTS AND DISCUSSION

Experimental results on the fabrication of titanium oxide nanotubes and the spectral absorption of thin film CdS and CdS nanopillars are presented in Section 6.1 while the Section 6.2 describes the results of numerical calculations and the related discussion.

6.1 Nano porous Titania Template: Experimental results

For our experiments, a nano porous template made of titanium dioxide (titania) serves as the host for embedding the CdS nanopillars inside its nanopores. The nanoporous titania matrix, by itself has negligible absorption in the visible part of the spectrum, and the Titania-CdS combination is advantageous over the traditional CdS window layer because it enhances the optical transmission through the window layer by increasing the effective energy band gap of CdS and thus extending the transmission edge of CdS.

In order to investigate the effect of host nanotube parameters, a study was done on the parameters that affect the pore diameter and the pitch of Titania nanotube arrays. Nano porous Titania templates were fabricated to study the effect of some of the parameters that affect the pore diameter and the pitch of the nanotube arrays. The results on the effect of anodization voltage and fluoride ion concentration in the anodization solution on the pore diameter and the pitch for the experimentally fabricated devices will be discussed below with the help of Table 6.1 and Figures 6.1-6.6.

Table 6.1 Effect of fluoride ion concentration and anodization voltage on pore diameter and interpore distance

Sample #	NH ₄ F	Anodization Voltage	Average Pore Diameter	Average interpore distance
1	2 mL	50 V	58.3 nm	85.4 nm
2	2 mL	60 V	50 nm	81.8 nm
3	0.81 mL	50 V	57.5 nm	88.2 nm
4	0.3 mL	40 V	49.3 nm	---
5	0.3 mL	50 V	57 nm	88.6 nm
6	0.3 mL	60 V	42 nm	79.2 nm

Table 6.1 shows the effect of fluoride ion concentration and anodization voltage on pore diameter and interpore distance (center-to-center distance between two adjoining nanopores). Three different fluoride ion concentration and three different anodization voltages were used, to successfully fabricate nano porous Titania template, in order to study their effect on the pore diameter and the pitch.

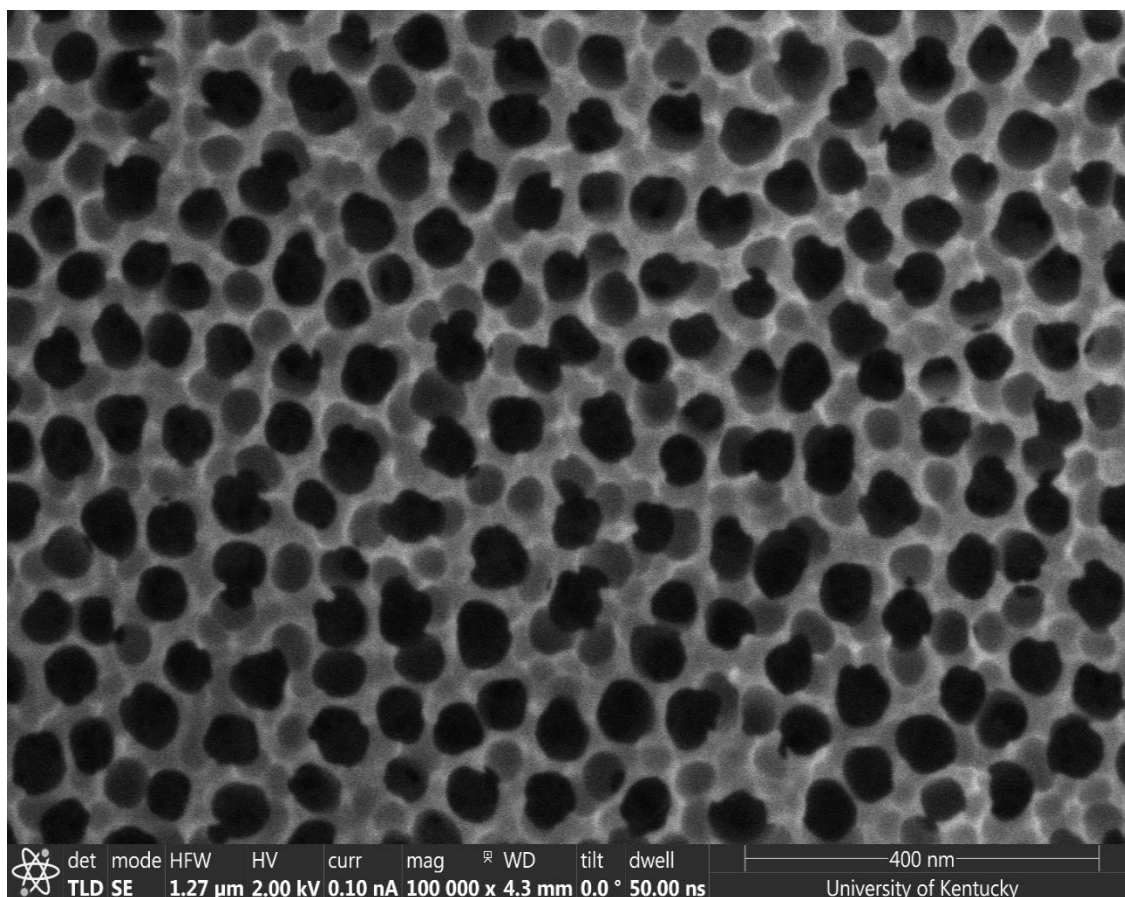


Figure 6.1 Top view SEM image of Sample # 1 fabricated in a fresh electrolyte comprising of 98 mL of EG and 2 mL of NH_4F at an anodization voltage of 50 V.

Figure 6.1 shows the top view SEM image of nanoporous template fabricated in a fresh electrolyte comprising of 98 mL of EG (Ethylene Glycol) and 2 mL of NH_4F at an anodization voltage of 50 V, the average pore diameter of the nanotubes thus obtained was found to be 58.5 nm and an average interpore distance of 85.4 nm.

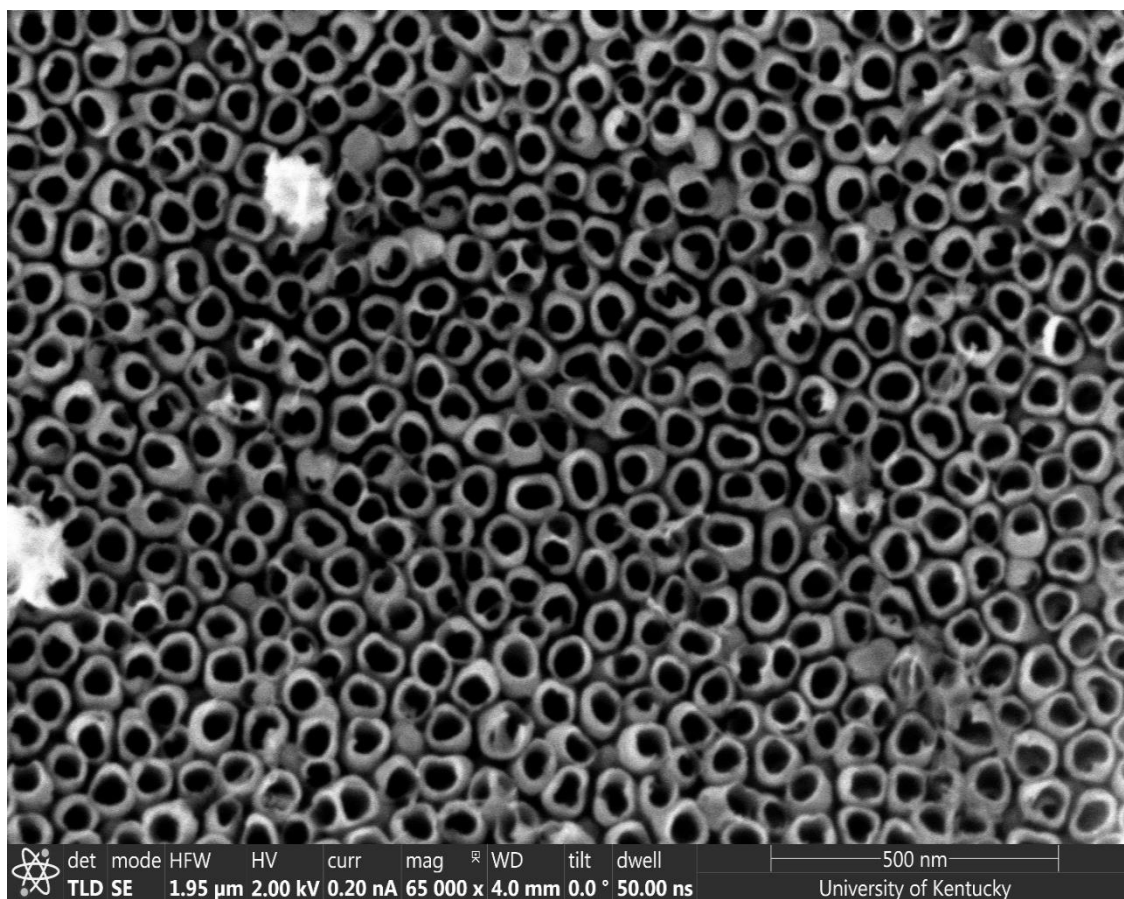


Figure 6.2 Top view SEM image of sample # 2 fabricated in a fresh electrolyte comprising of 98 mL of EG and 2 mL of NH₄F at an anodization voltage of 60 V.

Figure 6.2 shows the top view SEM image of nanoporous template fabricated in a fresh electrolyte comprising of 98 mL of EG (Ethylene Glycol) and 2 mL of NH₄F at an anodization voltage of 60 V, the average pore diameter of the nanotubes thus obtained was found to be 50 nm and an average interpore distance of 81.8 nm.

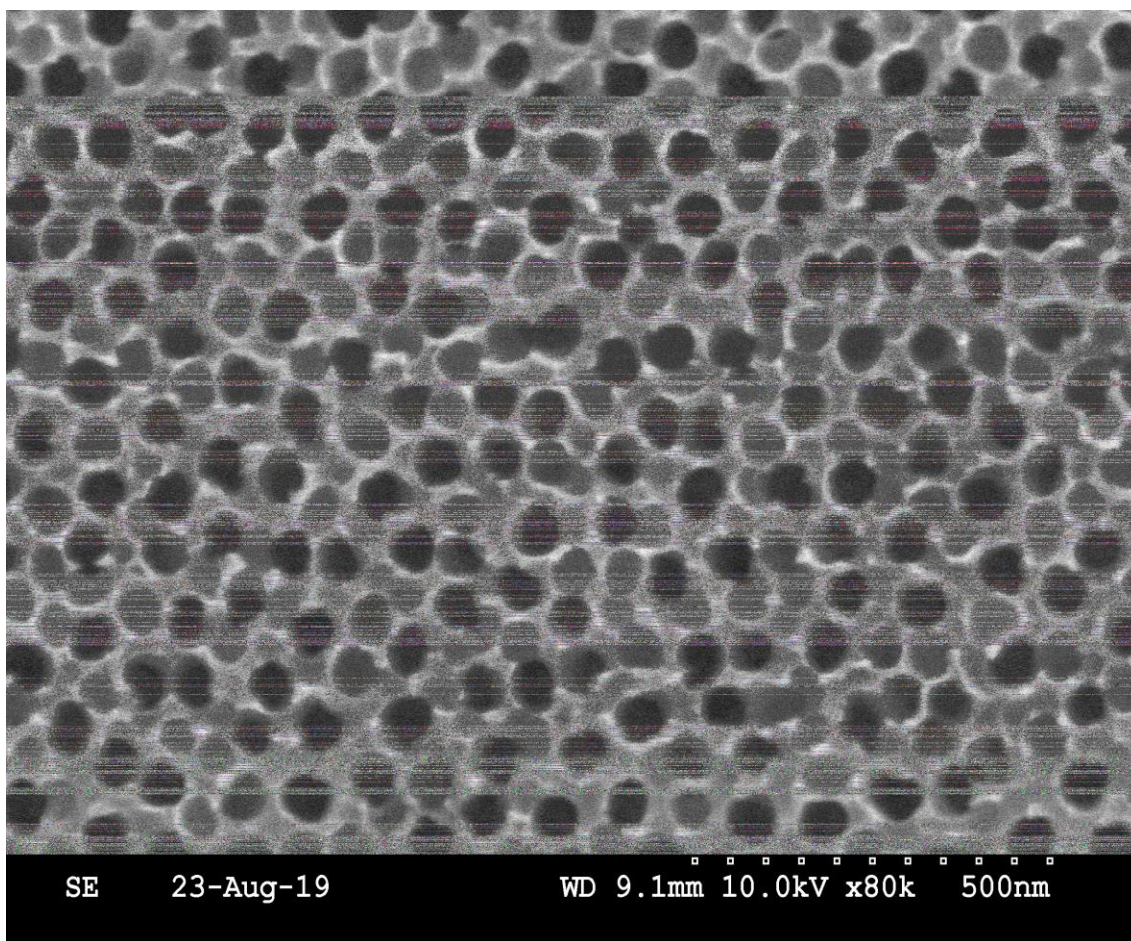


Figure 6.3 Top view SEM image of sample # 3 fabricated in a fresh electrolyte comprising of 98 mL of EG and 0.81 mL of NH₄F at an anodization voltage of 50 V.

Figure 6.3 shows the top view SEM image of nanoporous template fabricated in a fresh electrolyte comprising of 98 mL of EG (Ethylene Glycol) and 0.81 mL of NH₄F at an anodization voltage of 50 V, the average pore diameter of the nanotubes thus obtained was found to be 57.5 nm and an average interpore distance of 88.2 nm.

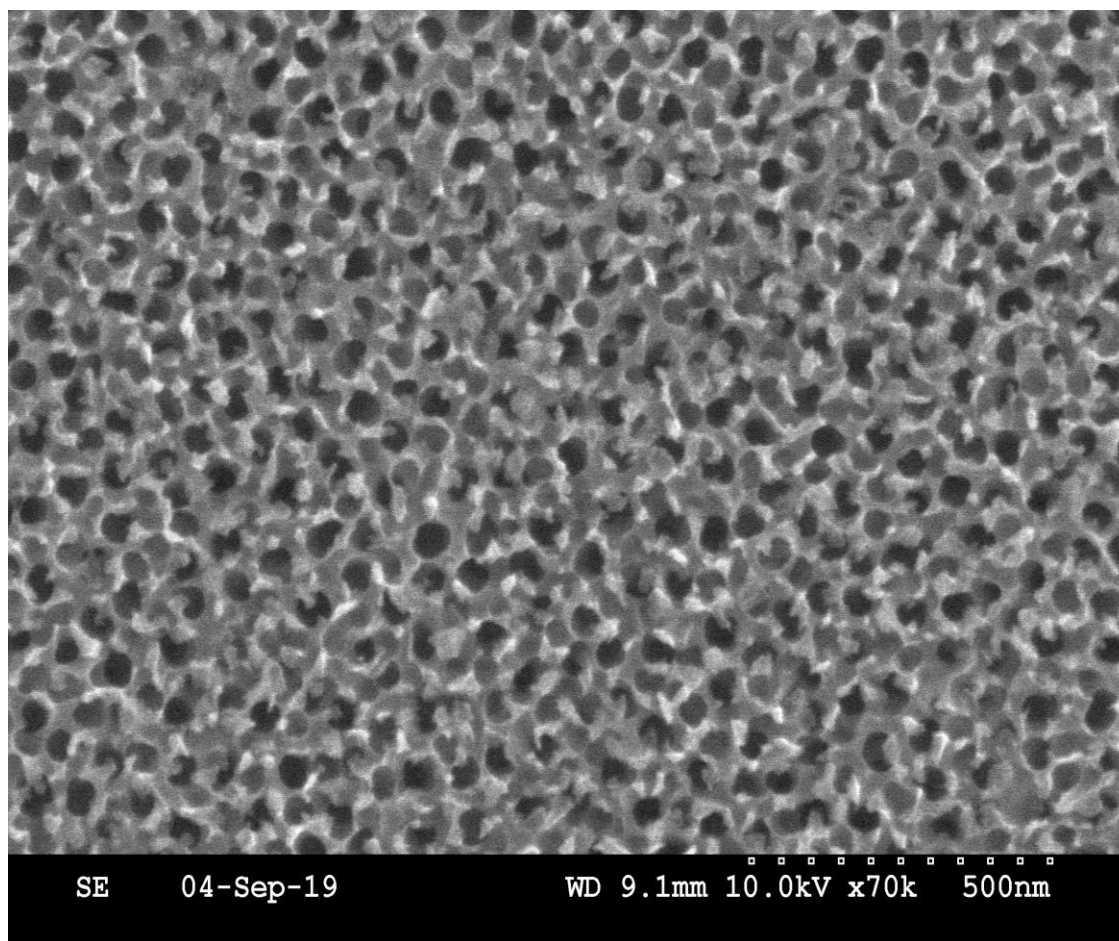


Figure 6.4 Top view SEM image of sample # 4 fabricated in a fresh electrolyte comprising of 98 mL of EG and 0.3 mL of NH₄F at an anodization voltage of 40 V.

Figure 6.4 shows the top view SEM image of nanoporous template fabricated in a fresh electrolyte comprising of 98 mL of EG (Ethylene Glycol) and 0.3 mL of NH₄F at an anodization voltage of 40 V, the average pore diameter of the nanotubes thus obtained was found to be 49.3 nm. Average interpore distance could not be estimated because the porous structure were not very well defined.

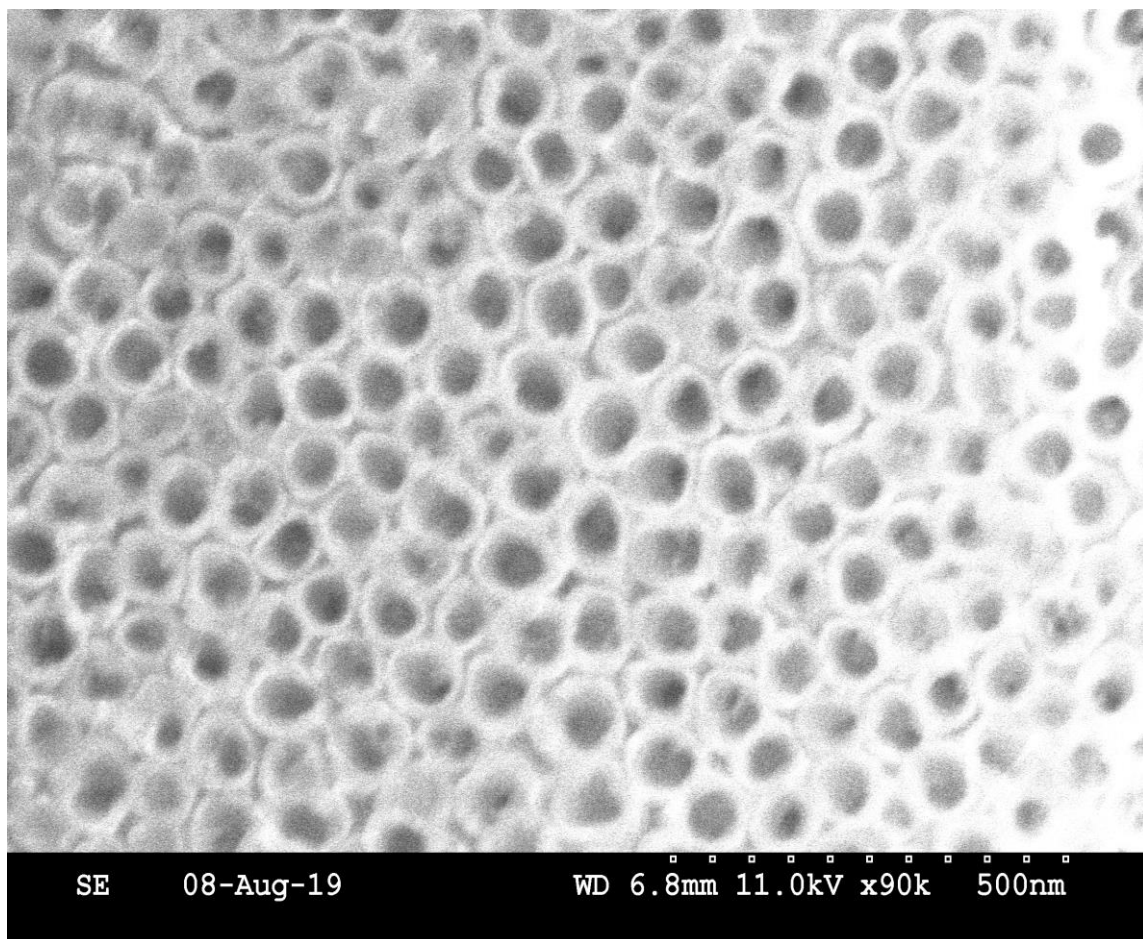


Figure 6.5 Top view SEM image of sample # 5 fabricated in a fresh electrolyte comprising of 98 mL of EG and 0.3 mL of NH₄F at an anodization voltage of 50 V.

Figure 6.5 shows the top view SEM image of nanoporous template fabricated in a fresh electrolyte comprising of 98 mL of EG (Ethylene Glycol) and 0.3 mL of NH₄F at an anodization voltage of 50 V, the average pore diameter of the nanotubes thus obtained was found to be 57 nm and an average interpore distance of 88.2 nm.

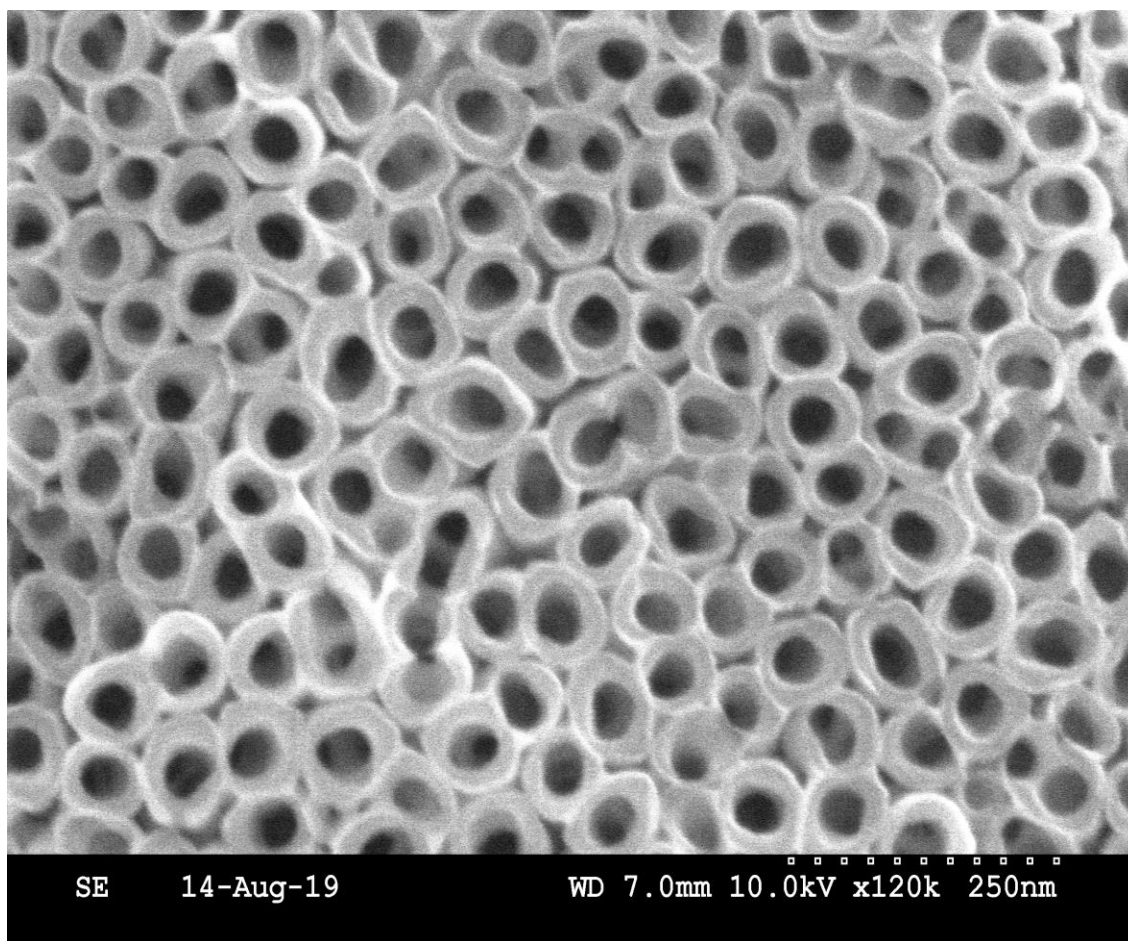


Figure 6.6 Top view SEM image of sample # 6 fabricated in a used electrolyte comprising of 98 mL of EG and 0.3 mL of NH₄F at an anodization voltage of 60 V.

Figure 6.6 shows the top view SEM image of nanoporous template fabricated using 98 mL of EG and 0.3 mL of NH₄F at an anodization voltage of 60 V, the electrolyte used was previously used to anodize one 4 μ m and one 150nm Titanium sample, the average pore diameter of the nanotubes thus obtained was found to be 42 nm and an average interpore distance of 79.2 nm.

6.1.1.1 Effect of Fluoride ion concentration on pore diameter

Three samples (Sample # 1, Sample # 3 and sample # 5) were anodized at 50 V with varying concentration of fluoride ions in the electrolyte. These samples were anodized in electrolyte containing 2 mL, 0.81 mL and 0.3 mL of NH_4F for Sample # 1, Sample # 3 and sample # 5 respectively. The anodization was otherwise performed under similar anodization conditions except for varying the fluoride ion concentration. From the Table 6.1 and Figure 1, 3, and 5 it is seen that the pore diameter increases only slightly, from 57 nm to 58.3 nm, when the fluoride concentration is increased from 0.3 mL to 2 mL. It is clear that in the experimental range investigated here, pore diameter of the titania nanotube matrix is rather insensitive to the ammonium fluoride concentration.

6.1.1.2 Effect of anodization voltage on pore diameter

In literature various authors have different opinion on the effect of anodization voltage on the pore diameter. In Ethylene Glycol based electrolyte several authors have suggested that the pore diameter increases with the increase in anodization voltage [28,29,41,47,56,57]. However, Y. Alivov et al. reported that in glycerol-based electrolyte the anodization potential does not have any clear dependence on the pore diameter of the TiO_2 nanotubes, when the anodization voltage was varied over the range of 10-240V [42].

For our devices, the effect of anodization voltage on pore diameter can be seen from the results obtained from sample # 4, sample # 5 and sample # 6. The electrolyte contained 0.3 mL of NH_4F in 98 mL of Ethylene Glycol. Sample # 4, sample # 5 and sample # 6 were anodized at three different voltages of 40 V, 50 V and 60 V respectively. From Table 6.1 and Figures 4-6 it is seen that when the anodization voltage is increased from 40 V to 50

V, the pore diameter increases from 49.3 nm to 57 nm. However, when the anodization voltage is increased further from 50 V to 60 V, the pore diameter decreased from 57 nm to 42 nm. Thus, for the case of ethylene glycol based electrolyte it can be suggested that there is an optimum anodization voltage at which the pore diameter is maximum for a fixed fluoride ion concentration.

6.1.1.3 Effect of Fluoride ion concentration on the pitch

The effect of fluoride ion concentration on the pitch can be seen with two sets of samples anodized at two different voltages. Set one contained Sample # 1, Sample # 3 and sample # 5 anodized at 50 V where the NH_4F content in the electrolyte were 2 mL, 0.81 mL and 0.3 mL respectively. Set two consisted of Sample # 2 and Sample # 6 anodized at 60 V. In set 1, pitch decreased from 88.6 nm to 85.4 nm when the Ammonium Fluoride content was increased from 0.3 mL to 2 mL. In set 2, pitch increased slightly from 79.2 nm to 81.8 nm when the Ammonium Fluoride content was increased from 0.3 mL to 2 mL. It is clear that in the experimental range investigated here, the pitch (interpore distance) of the titania nanotube matrix is rather insensitive to the ammonium fluoride concentration.

6.1.1.4 Effect of anodization voltage on pitch

The effect of anodization voltage on the pitch can be seen with two sets of samples anodized at two different voltages. Set one contained Sample # 1 and sample # 2 anodized at 50 V and 60 V respectively, where the electrolyte contained 2 mL of NH_4F in 98 mL of Ethylene Glycol. Set two consisted of Sample # 5 and Sample # 6 anodized at 50 V and 60

V respectively, where the electrolyte content was 0.3 mL of NH_4F in 98 mL of Ethylene Glycol. In set 1, pitch decreased from 85.4 nm to 81.8 nm when the anodization voltage was increased from 50 V to 60 V. In set 2, pitch decreased from 88.6 nm to 79.2 nm when the anodization voltage was increased from 50 V to 60 V. It is clear that an increase in anodization voltage from 50 V to 60 V leads to a substantial reduction in the pitch of the titania nanotube matrix.

From the above discussion it can be concluded that the anodization voltage is the more effective parameter, which can be tailored and optimized to fabricate Titania Nanotube arrays of desired porosity.

6.2 Numerical Results and Discussion

6.2.1 Interpolation of absorption profile for various CdS coverages

TiO₂ nanotubes, Planar CdS and Nanowire CdS were fabricated as explained in Chapter 3 and their absorption spectra were measured using Cary 50 UV-Vis Spectrophotometer. Defining the “CdS coverage” (x) as the fraction of the total surface area filled by the embedded CdS nanopillars, the absorption spectrum (A) for a particular value of CdS coverage (x) was obtained by interpolation as expressed in the Equation 6.1 below,

$$(x) * A_{CdS\ Planar} + (1 - x) * A_{TiO_2} = A_{CdS\ Nanowire\ (x)} \quad (6.1)$$

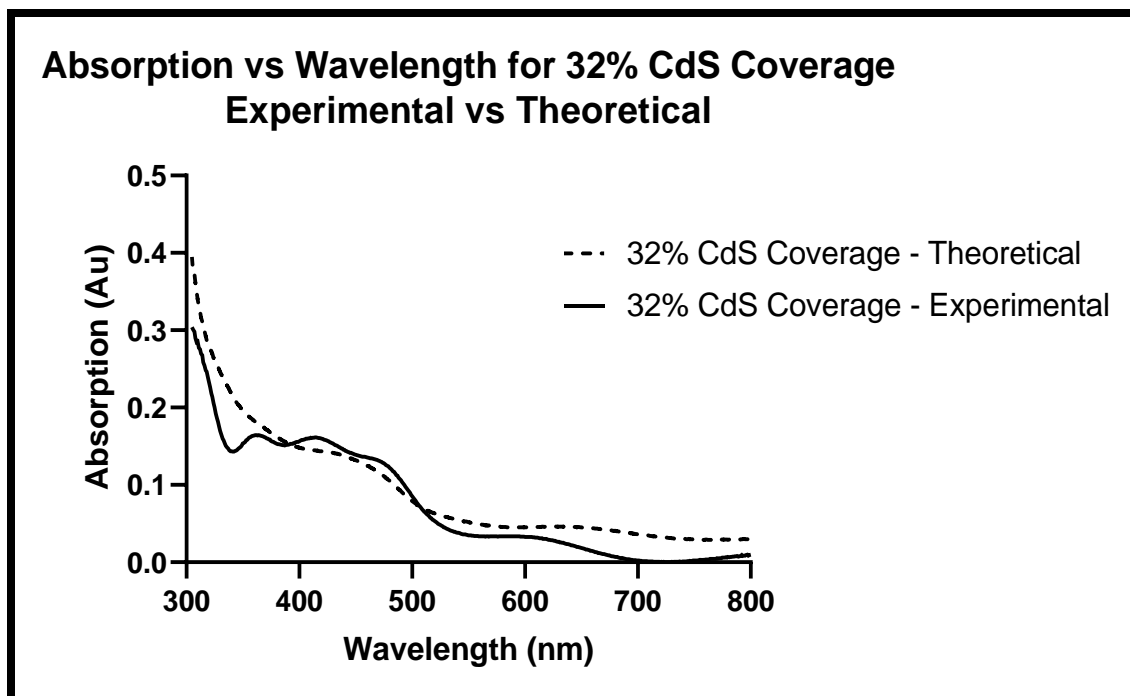


Figure 6.7 Absorption vs Wavelength for 32% CdS Coverage Experimental vs Theoretical

Figure 6.7 shows the comparison between the absorption profile for experimentally fabricated CdS Nanowires and the theoretical absorption profile CdS Nanowires for 32% coverage. The theoretical absorption profile was interpolated using equation (6.1). It is seen that the theoretical absorption profile for CdS Nanowires follows closely the experimental profile thus verifying that the linear assumption used in equation (6.1) holds.

The absorption profiles interpolated using equation (6.1) was input in SCAPS to replace the default absorption profile for different coverages of CdS.

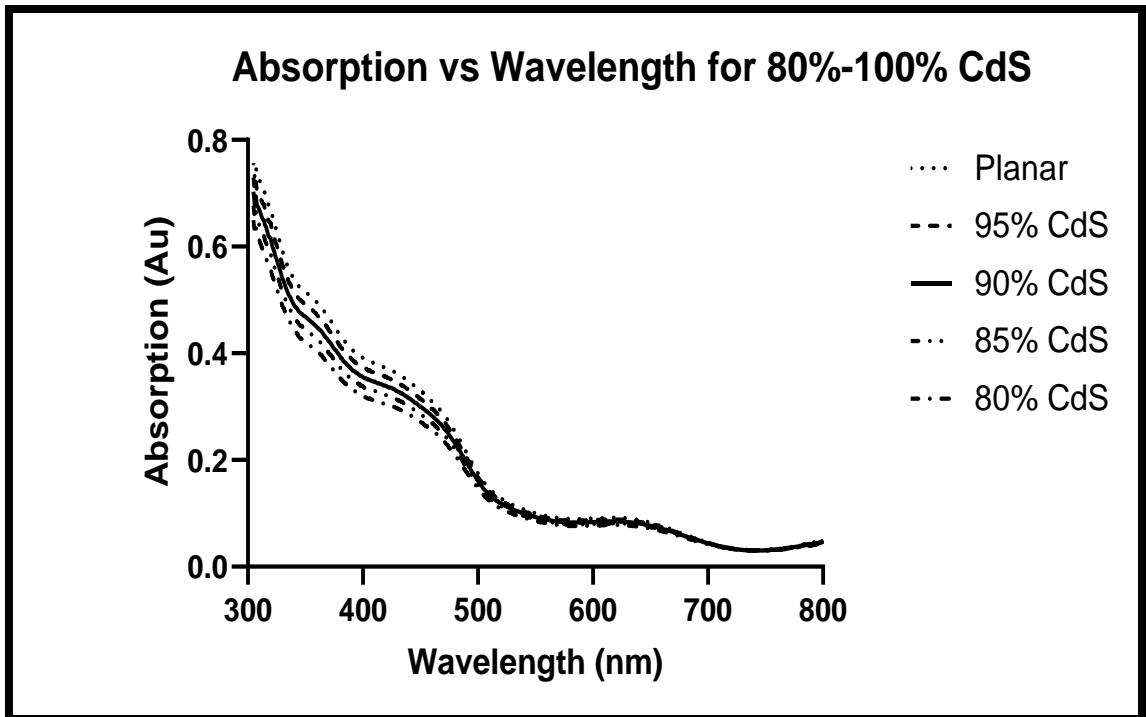


Figure 6.8 Theoretical absorption profile CdS Nanowires for 80% - 100% coverage

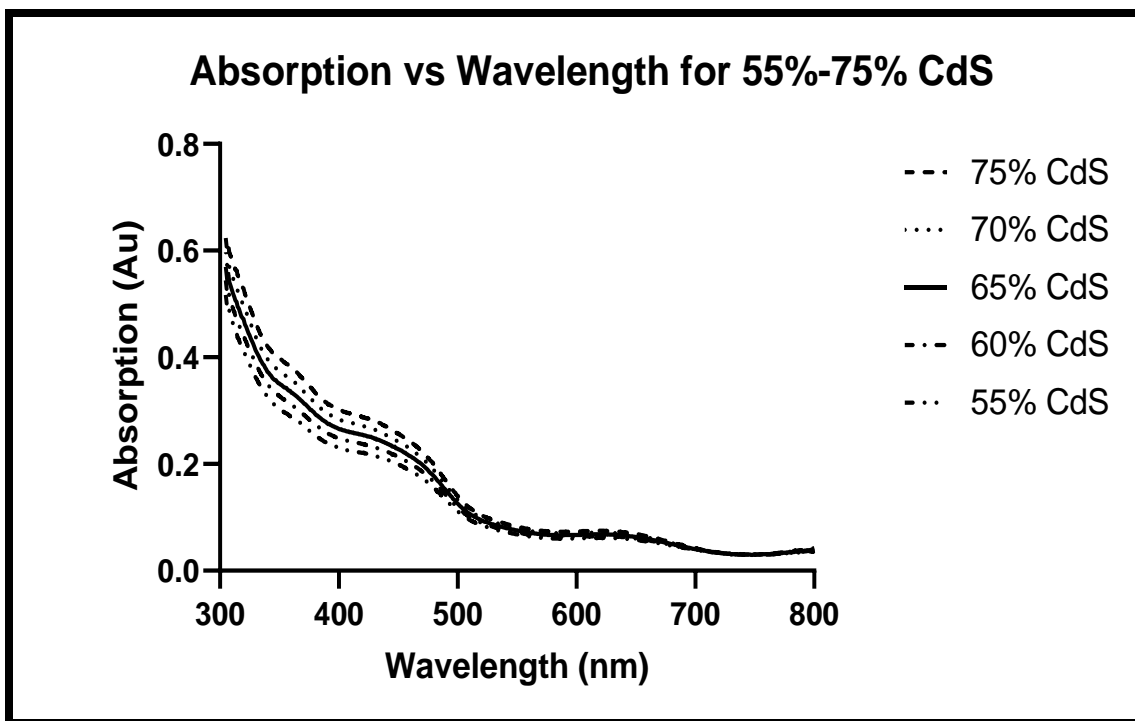


Figure 6.9 Theoretical absorption profile CdS Nanowires for 55% - 75% coverage

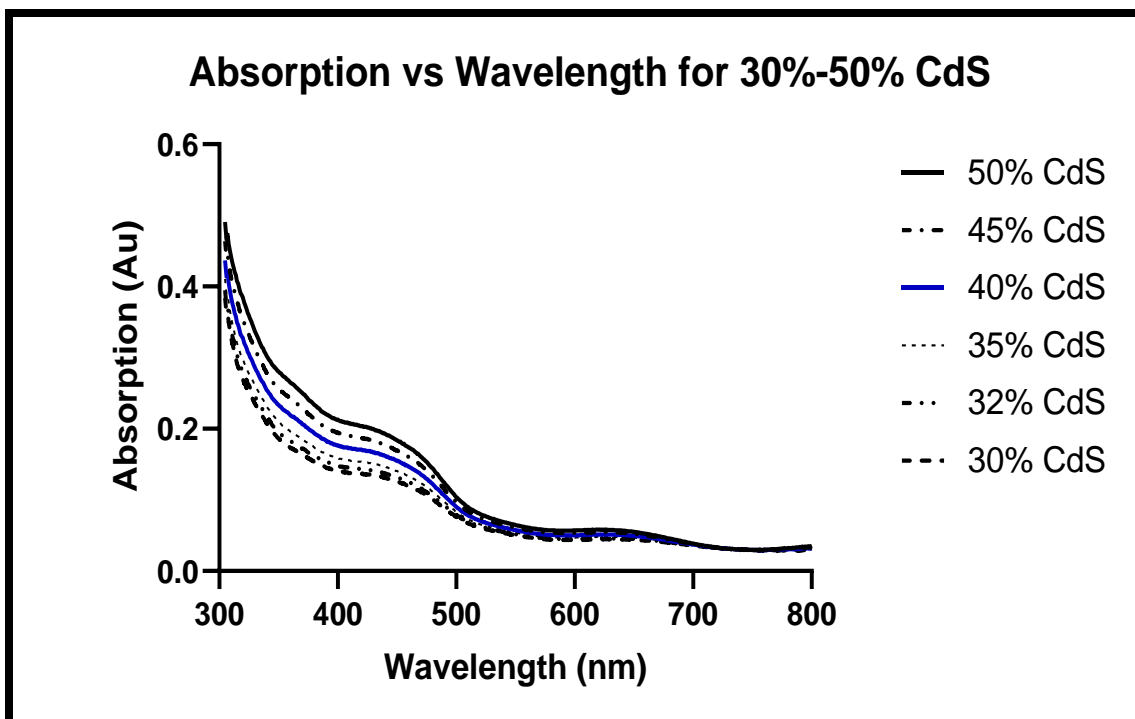


Figure 6.10 Theoretical absorption profile CdS Nanowires for 30% - 50% coverage

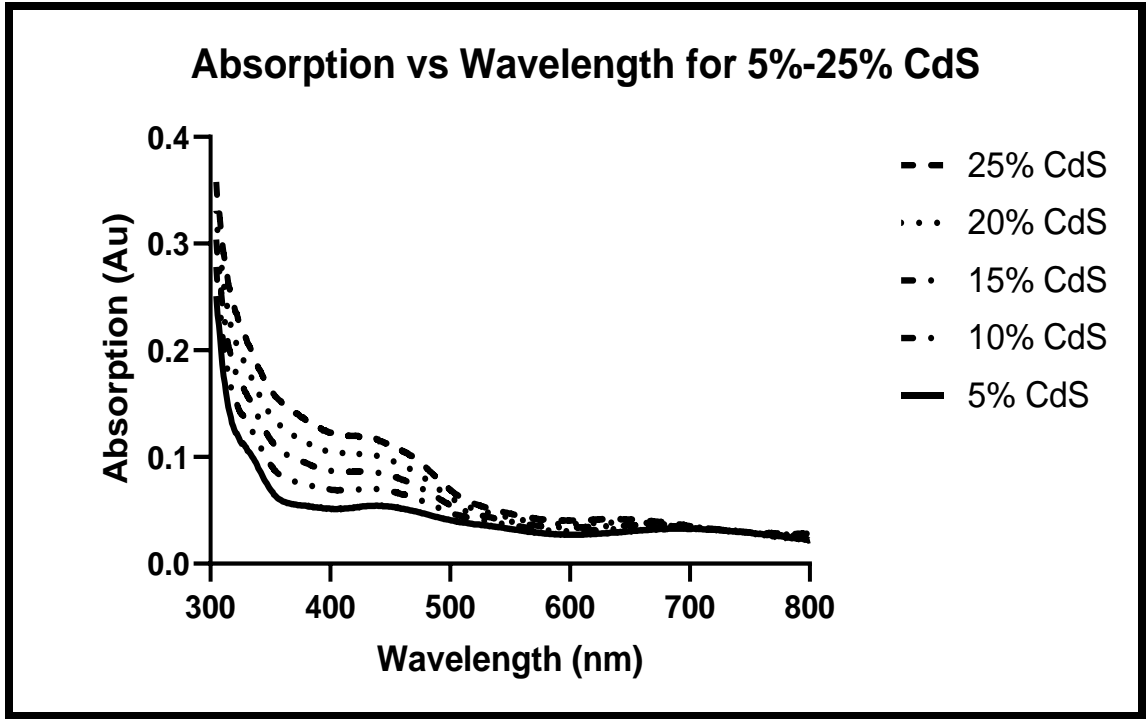


Figure 6.11 Theoretical absorption profile CdS Nanowires for 5% - 25% coverage

Figures 6.8 – 6.11 shows the theoretical absorption profile CdS Nanowires for 5% -100% coverage. The absorption spectrum (A) for a particular value of CdS coverage (x) was obtained by interpolation as expressed in the Equation 6.1. From the figures 6.8 –6.11 it can be seen that the absorption in the lower wavelength region drops from ≈ 0.8 Au to ≈ 0.25 Au when the CdS coverage drops from 100% to 5%.

The total interface state density (integrated over all energies) for the CdTe / CdS interface was varied in the range of $1.50\text{E}+4$ (cm^{-2}) to $3.00\text{E}+10$ (cm^{-2}) for different CdS coverages (0.0001% CdS to 100% CdS) to account for the reduced interface area (to fraction x) at the junction between the nanowire CdS window layer and the absorber CdTe layer. Acceptor type defect with Gauß type of Energetic Distribution was considered for the CdTe / CdS interface.

As the interface area between the CdTe / CdS junction reduces (from 100% CdS to 0.0001% CdS), a reduction in dark saturation current is obtained due to the decrease in interface recombination velocity that allows for less recombination at the interface which in turn enhances the overall device performance.

6.2.2 Results and Discussion on SCAPS simulation

6.2.2.1 Effect of host parameters and CdTe doping density on I-V characteristics

The effect of the host nanotube parameters (pore diameter and pitch for different CdS coverages) and CdTe doping density on device performance in nanowire CdS/ CdTe solar cells were studied using SCAPS-1D simulation and are presented in this section. To study the effect of CdTe doping density on the device performance, the shallow uniform acceptor density N_A (cm^{-3}) in CdTe was varied in the simulations from 10^{14} - 10^{18} cm^{-3} .

Also, to study the effect of host nanotube parameters the pore diameter was varied from a few nanometers to microns range and the pitch of the host nanotubes were varied from 100 nm to 10 μm in steps of one order of magnitude. For each set of simulations, the pitch was kept constant and the pore diameter were varied proportionally to give a certain percentage of CdS coverage in the film. To simulate for different CdS coverages, ranging from 0.0001% - 100%, the total interface state density (cm^{-2}) was varied.

In CdS/ CdTe solar cells the bulk series resistance is negligible in comparison to the contact resistance. However, as the pore diameter and the pitch are varied in order to obtain different CdS coverages, the bulk series resistance for the nanostructured device changes. The bulk series resistance varies over a considerable range and the contact resistance is no longer dominant which affects the device performance considerably. For the simulations the total series resistance of $2 \Omega\text{-cm}^2$ was assumed for the planar CdS/ CdTe solar cell.

The resistance calculations derived in chapter 2 for the planar CdS and the nanowire CdS devices, were used in the simulations in conjunction to the other parameter changes.

From the equations 2.29 and 2.37, it is seen that the bulk series resistance in case of planar devices is inversely proportional to the doping. In case of nanowire devices, the bulk series resistance is dependent on the doping, the pore diameter, pitch and the CdTe thickness. However, for the simulations the CdTe thickness was kept constant at 5 μm .

$$R_{eff\ Planar} = \frac{\eta N_1 \alpha}{I_L \mu_p p A} \left[\frac{t e^{-\alpha t}}{\alpha} - \frac{e^{-\alpha t}}{\alpha^2} + \frac{1}{\alpha^2} \right] \quad (2.29)$$

$$R_{eff\ nanowire} = R_{eff\ Planar} * \left[1 + \left(\frac{L}{\sqrt{2}} - \frac{D}{2} \right) * \frac{1}{h} \right] \quad (2.37)$$

The results of the simulations showed that by using CdS nanopillars embedded in nanoporous template as the window layer, an absolute gain of 1.05% in efficiency could be achieved over the case of the planar CdS window layer. This gain in efficiency was obtained when the CdS coverage was 0.1%, CdTe doping density was 10^{17} cm^{-3} , the pore diameter could range from 2.35nm – 23.48nm and the interpore distance ranging from 100nm – 1000nm. The planar device was 24.88% efficient whereas 25.93% efficient solar cells could be achieved with the CdS nanopillars device.

In the sections to follow the results obtained from SCAPS simulations for an interpore distance of 100nm will be discussed and comparison will be made on the solar cell parameters, Voc, Jsc, FF and Efficiency, for various CdTe dopings against optimal doping of 10^{17} cm^{-3} . The results obtained for an interpore distance of 100nm is chosen over an interpore distance of 1000nm as the nanoporous Titania template fabricated in our lab is closer to 100nm. Other results obtained from the SCAPS simulation to study the effect of various parameter are presented as plots and tables in the Appendix section.

6.2.2.2 Short Circuit Current enhancement

The bandgap of planar Cadmium Sulfide is 2.4 eV, loss of photocurrent is caused by light absorption in the n-Cadmium Sulfide (CdS) window layer in the shorter wavelength region (below 512 nm), leading to the degradation of cell performance. High density of recombination sites present in CdS films prevents the photons, with wavelength less than 512 nm that are absorbed in CdS, from contributing to the collected photocurrent. This loss is reduced when an array of CdS nanowires replaces the conventional planar n-CdS film.

When the CdS nanowires are embedded in the nano porous template, an increase in the effective bandgap for CdS is obtained which in turn suppresses the photon loss in the lower wavelength region and makes the window layer more transmittive to sunlight than is the case with the traditional planar CdS window layer. This leads to an increase in the number of photons available to the p-CdTe absorber. These extra photons lead to an increase the short circuit current. Also, the dominant junction current mechanism at the nanowire CdS-CdTe heterojunction involves interface recombination at the CdS-CdTe interface [58]. This interface recombination current is reduced in the case of the CdS-nanopillars-window layer and therefore a higher open circuit voltage (V_{oc}) is achieved.

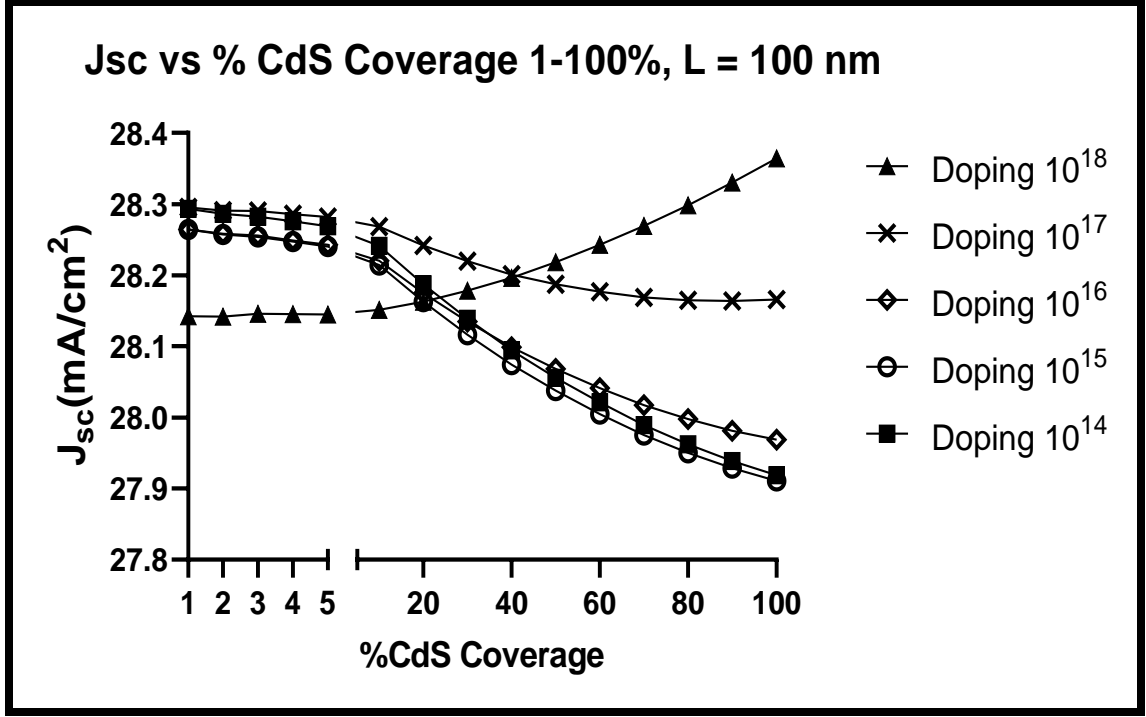


Figure 6.12 Jsc vs 1-100% CdS Coverage Interpore Distance 100nm

Figure 6.12 shows the plot of short circuit current vs CdS coverage for the simulated results where the CdS coverage was varied from 1% to 100% for various doping levels. The CdTe doping density varied from 10^{14} cm^{-3} to 10^{18} cm^{-3} .

It is seen that as a result of transmission gain obtained using nanopillars of CdS, the short circuit current increases with a decrease in the CdS coverage. An increase in short circuit current was expected as the number of photons available to the p-CdTe absorber increased by lowering the CdS coverage, i.e., a smaller number of photons being lost in the lower wavelength region for the nanowire CdS as compared to the planar CdS. At relatively low doping levels, 10^{14} cm^{-3} to 10^{17} cm^{-3} , the transmission gain is dominant and results in a better enhancement of the short circuit current.

At higher doping levels the dopants, impurities that also act as recombination centers, has more pronounced effect on the short circuit current. The absolute gain in the short circuit current at higher doping level gets reduced as was expected, an increase in the number of recombination sites counters the gain that was obtained from higher transmission using nanostructures. However, at the doping level of 10^{17} cm^{-3} transmission gain still being the dominant mechanism results in an increase in the short circuit current, as the number of recombination sites are not enough to counter the gain obtained from transmission.

At higher doping level of 10^{18} cm^{-3} the dopants (a) offers low resistivity, higher mobility for the flow of electrons and holes; (b) act as recombination centers causing greater recombination. However, the recombination tends to be more dominant mechanism and despite of the higher mobility the electrons and holes generated by the photons absorbed in CdTe layer, all the electrons and holes generated do not reach the junction. This causes a loss in photocurrent; this effect is seen in figure 6.12 where we see that there is a slight dip in the short circuit current with the decreasing CdS coverage.

The maximum short circuit current of 28.3 mA cm^{-2} is obtained for doping density of 10^{17} cm^{-3} .

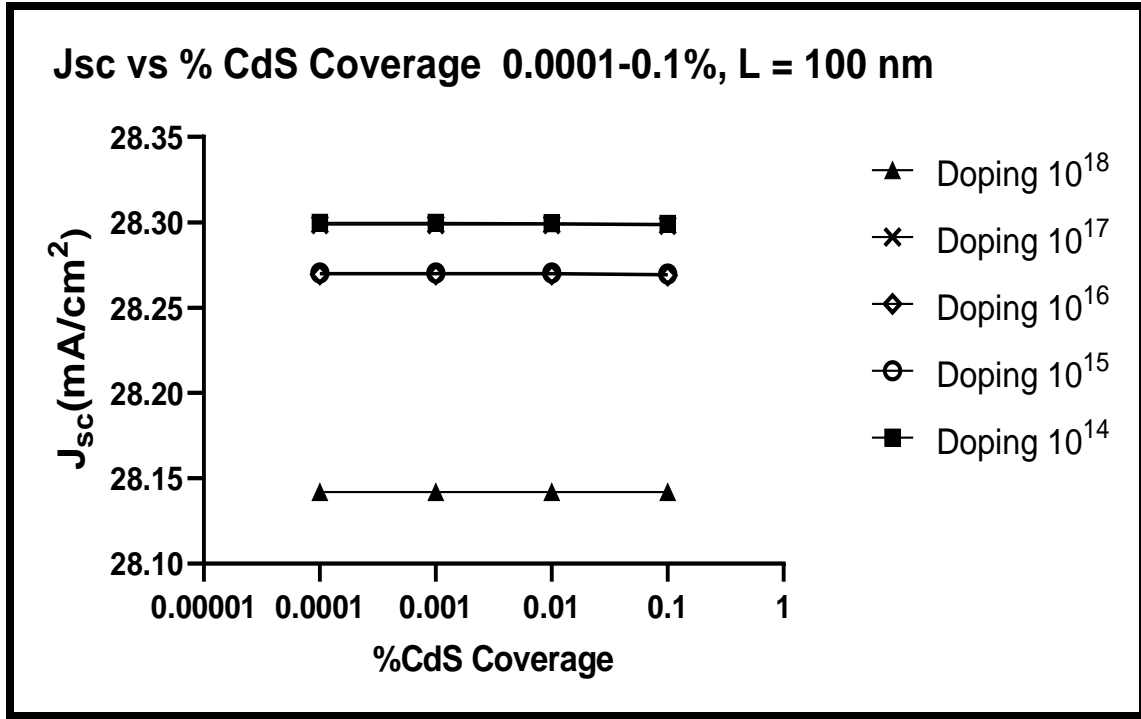


Figure 6.13 Jsc vs 0.0001-0.1% CdS Coverage Interpore Distance 100nm

Figure 6.13 shows the plot of short circuit current vs CdS coverage for the simulated results where the CdS coverage was varied from 0.0001% to 0.1% for various doping levels. The CdTe doping density varied from 10^{14} cm^{-3} to 10^{18} cm^{-3} .

In the plot it is seen that the short circuit current, irrespective of the doping level, saturates below 0.1% CdS coverage. This gives us the threshold point below which there is no additional advantage to be gained in terms of transmission.

The maximum short circuit current of 28.3 mA cm^{-2} , after which it saturates, is obtained for doping density of 10^{17} cm^{-3} .

6.2.2.3 Enhancement in the Open Circuit Voltage

The dominant junction current mechanism at the nanowire CdS-CdTe heterojunction involves interface recombination at the CdS-CdTe interface [58]. Reduction in the junction area between CdS and CdTe leads to a reduction in the total number of interface states. This is an advantage because interface states are known [59,60] to lead an increase in the effective reverse saturation current and a reduced open circuit voltage.

As the interface area at the junction between CdTe and CdS nanowires for different CdS coverage is reduced by a factor of x . Assuming $I_{01} = \frac{1}{x} I_{02}$ and $I_{L2} = y * I_{L1}$ Where y represents the current enhancement factor due to a better window layer as has been demonstrated in Figures 6.12 and 6.13 and I_0 and I_L are the effective reverse saturation current and the light generated current respectively.

$$V_{oc} = \frac{\eta kT}{q} \ln \left(\frac{J_{sc}}{J_0} + 1 \right) \quad (2.16)$$

For Planar CdS/ CdTe Solar Cell:

$$V_{OC_Planar} = \frac{\eta kT}{q} \ln \left(\frac{I_{L1}}{I_{01}} \right) \quad (6.2)$$

For Nanowire CdS/ CdTe Solar Cell:

$$V_{OC_Nanowire} = \frac{\eta kT}{q} \ln \left(\frac{I_{L2}}{I_{02}} \right) \quad (6.3)$$

Therefore,

$$V_{OC_Nanowire} - V_{OC_Planar} = \frac{\eta kT}{q} \ln \left(\frac{I_{L2}/I_{L1}}{I_{01}/I_{02}} \right) \quad (6.4)$$

From the above equation 6.4 it is seen that the open circuit voltage can be enhanced by using nanowire CdS window layer. The open circuit voltage depends on the reverse saturation current density, which in turn depends on the acceptor doping density.

$$J_0 = qN_C N_V \left(\frac{1}{N_A} \sqrt{\frac{D_n}{\tau_n}} + \frac{1}{N_D} \sqrt{\frac{D_p}{\tau_p}} \right) e^{-\frac{E_g}{kT}} \quad (2.17)$$

From equations (6.4) & (2.17) it is seen that with an increase in the doping concentration the effective reverse saturation current decreases leading to an increase in the open circuit voltage.

The reverse saturation current across the junction in CdS/ CdTe solar cell is comprised of (i) diffusion current, (ii) generation-recombination current, (iii) tunneling between CdS conduction band and empty trap levels followed by the hole capture by the trap and (iv) recombination via interface states [60]. The dominant junction current mechanism at the nanowire CdS-CdTe heterojunction involves interface recombination at the CdS-CdTe interface [58].

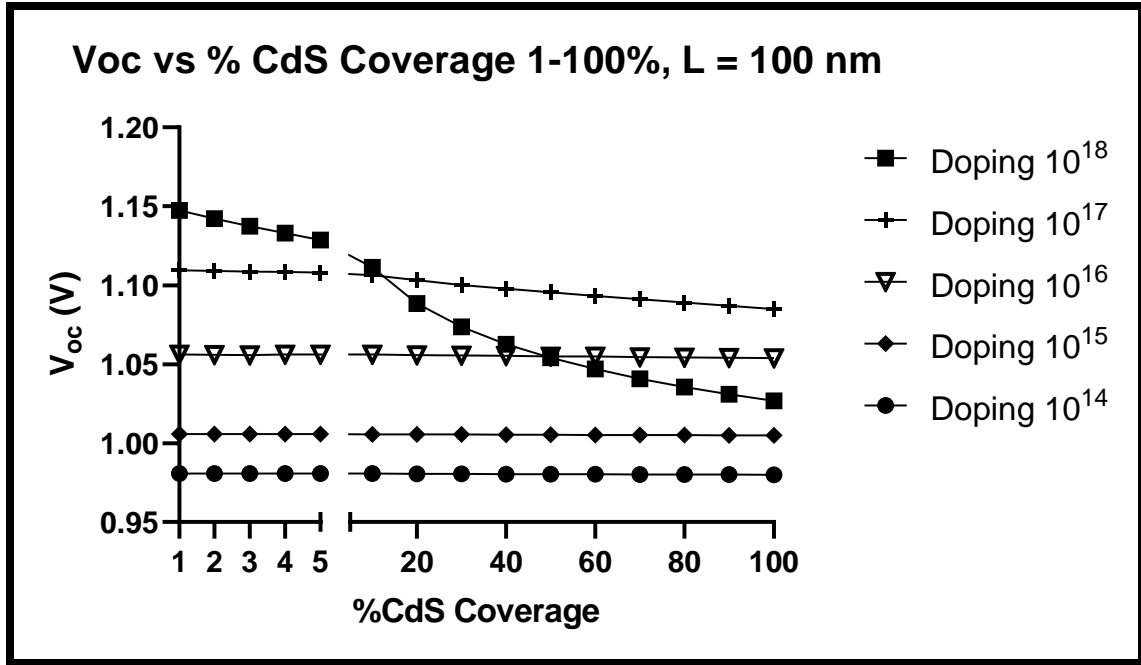


Figure 6.14 Voc vs 1-100% CdS Coverage Interpore Distance 100nm

Figure 6.14 shows the plot of open circuit voltage vs CdS coverage for the simulated results where the CdS coverage was varied from 1% to 100% for various doping levels. The CdTe doping density were varied from 10^{14} cm^{-3} to 10^{18} cm^{-3} .

At doping levels of 10^{14} cm^{-3} - 10^{16} cm^{-3} , the gain obtained by reduction in interface states is not visible because at these low doping levels (Na) electron transport mechanisms other than interface recombination are more likely to be dominant, as is indicated by equation (2.17).

At higher doping levels, 10^{17} cm^{-3} and 10^{18} cm^{-3} , other electron transport mechanisms become less important and interface recombination becomes dominant. the net effect is an increase in the effective reverse saturation current that leads to an increase in the open circuit voltage as seen in Fig. 6.14. An open circuit voltage of 1.11V can be achieved for a doping density of 10^{17} cm^{-3} .

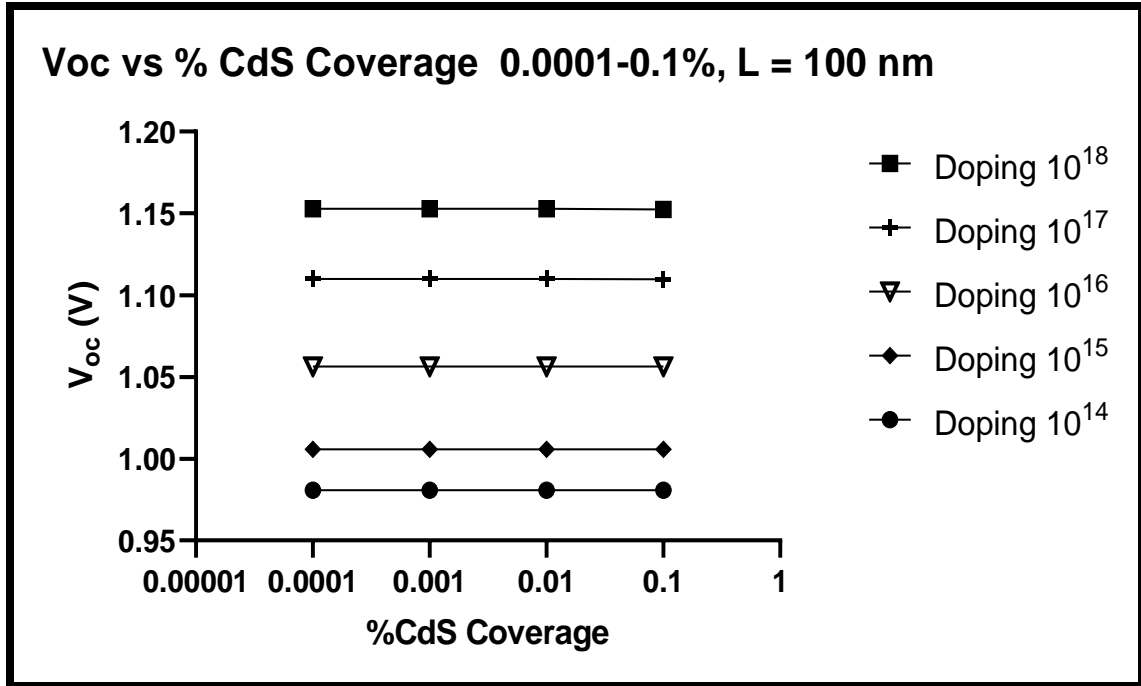


Figure 6.15 Voc vs 0.0001-0.1% CdS Coverage Interpore Distance 100nm

Figure 6.15 shows the plot of open circuit voltage vs CdS coverage for the simulated results where the CdS coverage was varied from 0.0001% to 0.1% for various doping levels. The CdTe doping density were varied from 10^{14} cm^{-3} to 10^{18} cm^{-3} .

The dominant junction current mechanism at the nanowire CdS-CdTe heterojunction involves interface recombination at the CdS-CdTe interface [58]. The open circuit voltage increases as the CdTe doping is increased, increase in the doping level causes a reduction in the effective reverse saturation current. However, the number of interface states below 0.1% CdS coverage becomes so low such that the recombination via interface states is no longer the dominant junction current mechanism and any further reduction in the CdS coverage does not improve the Voc any further.

An open circuit voltage of 1.153V can be achieved for a doping density of 10^{18} cm^{-3} .

6.2.2.4 Effect of decreasing CdS coverage on Fill Factor

When the parasitic series resistance and shunt resistance, R_s and R_{sh} , both have negligible effect on the solar cell performance, the fill factor can be approximately expressed in terms of open-circuit voltage as [18]

$$FF = \frac{\frac{qV_{oc}}{kT} - \ln\left(0.72 + \frac{qV_{oc}}{kT}\right)}{1 + \frac{qV_{oc}}{kT}} \quad (2.19)$$

However, when either the series resistance or the shunt resistance has significant effect on the device performance the above equation may yield inaccurate results.

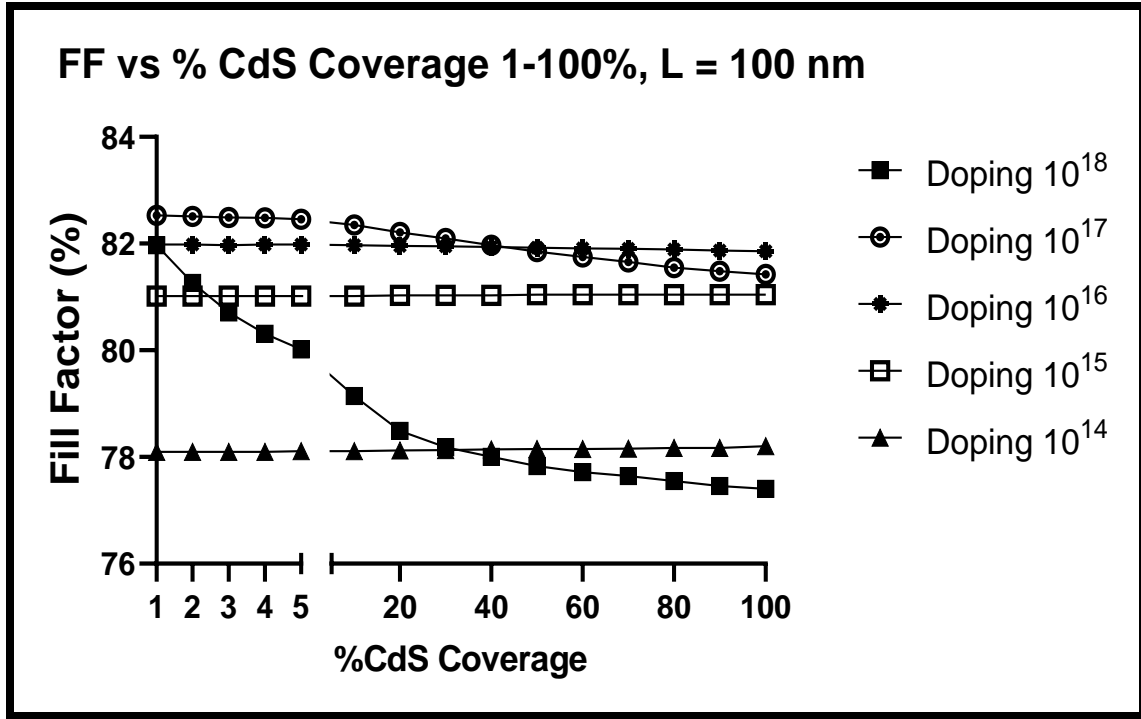


Figure 6.16 FF vs 1-100% CdS Coverage Interpore Distance 100nm

Figure 6.16 shows the plot of fill factor vs CdS coverage for the simulated results where the CdS coverage was varied from 1% to 100% for various doping levels. The CdTe doping density were varied from 10^{14} cm^{-3} to 10^{18} cm^{-3} .

At lower acceptor doping density of 10^{14} cm^{-3} the bulk series resistance is high that counters the effect of increase in Voc as the interface state density is reduced. The overall effect is such that the fill factor of the device practically remains unchanged.

However, at higher acceptor doping density of 10^{17} cm^{-3} the bulk series resistance is lower and the dominant factor causing the increase in fill factor is the contribution from increase in Voc with reduced number of interface states. The fill factor gradually increases in a linear fashion with the decreasing CdS coverage. At even higher acceptor doping density of 10^{18} cm^{-3} , the series resistance has negligible effect to counter the gain obtained

from the increase in Voc. This can be seen in figure 6.16, where, the fill factor increases exponentially with decreasing CdS coverage.

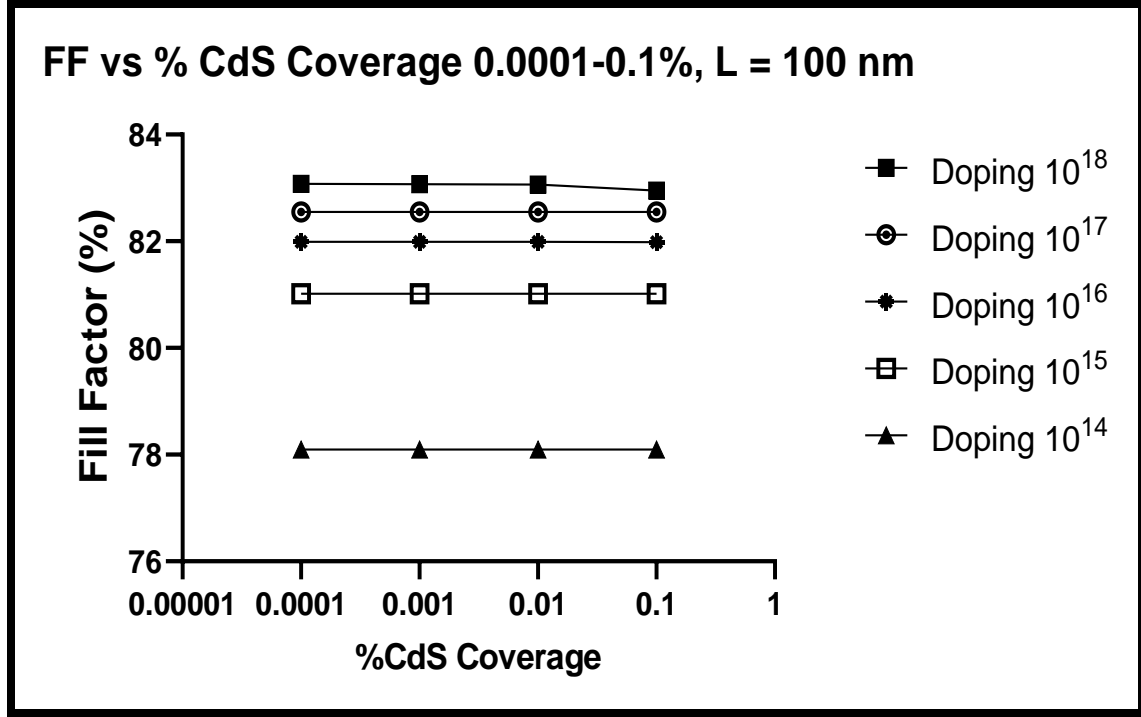


Figure 6.17 FF vs 0.0001-0.1% CdS Coverage Interpore Distance 100nm

Figure 6.17 shows the plot of fill factor vs CdS coverage for the simulated results where the CdS coverage was varied from 0.0001% to 0.1% for various doping levels. The CdTe doping density were varied from 10^{14} cm^{-3} to 10^{18} cm^{-3} .

The fill factor tracks the open circuit voltage when the parasitic series resistance and shunt resistance, R_s and R_{sh} , both have negligible effect on the solar cell performance. As the open circuit voltage reaches the saturation at less than 0.1% CdS coverage results in the saturation of the fill factor below 0.1% CdS coverage, the bulk series resistance is negligibly affected for a interpore distance of 100 nm.

6.2.2.5 Effect of decreasing CdS coverage on Efficiency

$$\begin{aligned} PCE (\eta) &= \frac{P_m(\text{Maximum Power that the solar cell can deliver})}{\text{Incident Power from Sunlight}} \\ &= \frac{V_{OC} * I_{SC} * FF}{P_{inc}} \end{aligned} \quad (2.21)$$

Where P_{inc} is the incident power from the incoming solar radiation and is given by

$$P_{inc} = A \int_0^{\infty} F(\lambda) \left(\frac{hc}{\lambda} \right) d\lambda \quad (2.22)$$

A is the total device area, $F(\lambda)$ is the incident photon flux and $\left(\frac{hc}{\lambda} \right)$ is the energy associated with each photon.

The efficiency of a solar cell is a function of open circuit voltage, short circuit current and the fill factor. With the open circuit voltage, short circuit current and the fill factor all increasing the overall efficiency can be increased by up to 4.53%, absolute value. This absolute gain in efficiency is the advantage obtained from using the nanostructured devices. The record research cell conversion efficiency improved from 17.8% in 2011 [61] to 22.1% in 2016 [62] and has not increased since 2016. By employing the nanostructured CdS window layer instead of conventional Planar CdS, using SCAPS simulation it is shown that the cell conversion efficiency can be improved considerably, and the amount of toxic cadmium used in the CdTe solar cell can also be reduced.

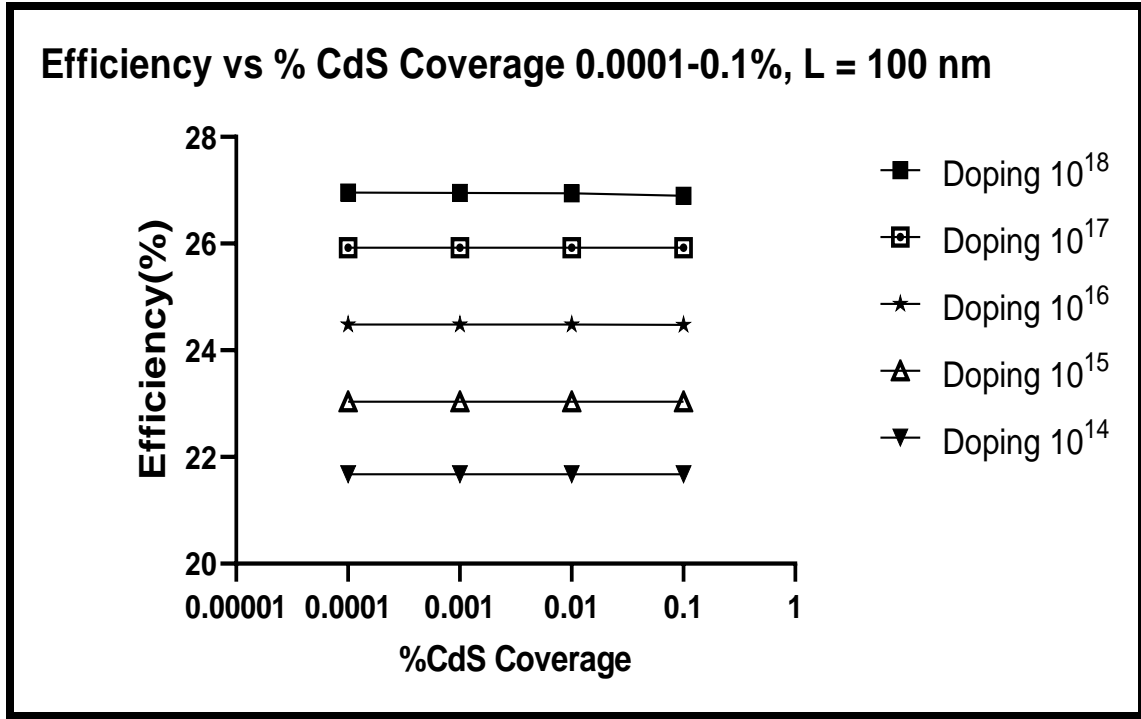


Figure 6.18 Efficiency vs 0.0001-0.1% CdS Coverage Interpore Distance 100nm

Figure 6.18 shows the plot of Efficiency vs CdS coverage for the simulated results where the CdS coverage was varied from 0.0001% to 0.1% for various doping levels. The CdTe doping density were varied from 10^{14} cm^{-3} to 10^{18} cm^{-3} .

For the CdS coverages below 0.1% in the film, as the open circuit voltage and the short circuit current starts to saturate, for 10^{14} cm^{-3} to 10^{17} cm^{-3} doping levels, so does the efficiency. The efficiency increases from 21.68% for 10^{14} cm^{-3} doped CdTe layer to 25.92% for 10^{17} cm^{-3} doped CdTe layer at CdS coverage level of 0.1%. Below 0.1% CdS coverage no gain in efficiency is observed for 10^{14} cm^{-3} to 10^{17} cm^{-3} doping levels.

However, for 10^{18} cm^{-3} doping as the open circuit voltage keeps on increasing and the short circuit current fall below 0.1% CdS coverage, the overall effect is a slight gain in

the efficiency of the device which can be attributed to higher doping and not from the advantages obtained for the nanostructured device.

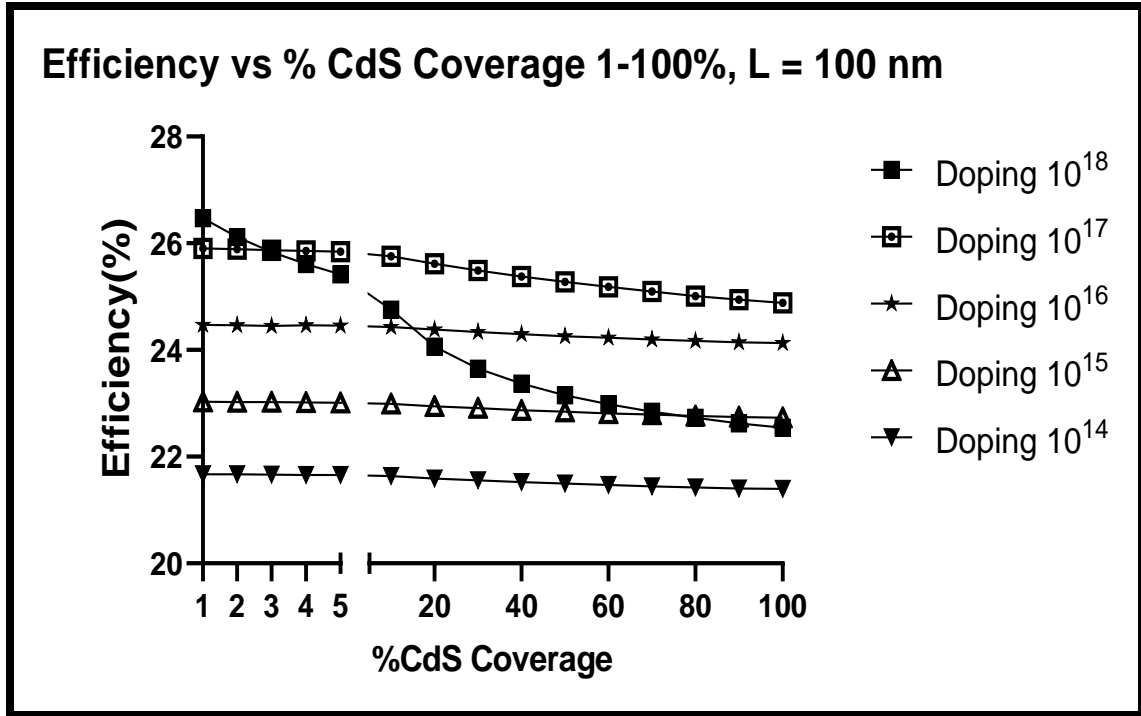


Figure 6.19 Efficiency vs 1-100% CdS Coverage Interpore Distance 100nm

Figure 6.19 shows the plot of Efficiency vs CdS coverage for the simulated results where the CdS coverage was varied from 1% to 100% for various doping levels. The CdTe doping density were varied from 10^{14} cm^{-3} to 10^{18} cm^{-3} .

As the open circuit voltage and the short circuit current keeps on increasing with lowering of the CdS coverage, for 10^{14} cm^{-3} to 10^{17} cm^{-3} doping levels, so does the efficiency. The efficiency increases from 21.40% for 10^{14} cm^{-3} doped CdTe layer to 25.92% for 10^{17} cm^{-3} doped CdTe layer as CdS coverage decreases from 100% - 1% and the doping increases from 10^{14} cm^{-3} to 10^{18} cm^{-3} .

However, for 10^{18} cm^{-3} doping as the open circuit voltage keeps on increasing and the short circuit current falls, the overall effect is a slight gain in the efficiency of the device which can be attributed to higher doping and not from the advantages obtained for the nanostructured device.

Table 6.2 (on the next page) shows the values of Voc, Jsc, FF and Efficiency for various CdS Coverages at $10^{17}(\text{cm}^{-3})$ CdTe doping. The results presented in the table is for an optimal interpore distance ranging from 100nm-1000nm. It is seen that the values of Voc, Jsc, FF and Efficiency gets saturated for a CdS coverage of 0.1%. At an acceptor doping density of $10^{17}(\text{cm}^{-3})$, the enhancement in the device performance is mainly from the advantage obtained using the nanostructure device design. This conclusion is reached from the fact that the Voc and the Jsc is still increasing with the decreasing CdS coverage, i.e., the increase in transmission obtained at reduced CdS coverage is still the dominant mechanism contributing in the enhancement of the device performance. Other results obtained from the SCAPS simulation to study the effect of various parameter is presented as plots and tables in the Appendix section.

**Table 6.2 Effect of CdS Coverage on Voc, Jsc, FF and Efficiency for 10¹⁷
doping density**

% CdS	Voc (V)	Jsc (mA/cm²)	FF (%)	Efficiency (%)
0.0001	1.1098	28.298603	82.55	25.925479323
0.001	1.1098	28.298600	82.55	25.925476574
0.01	1.1098	28.298570	82.55	25.925449090
0.1	1.1097	28.298266	82.55	25.922834562
1	1.1094	28.295106	82.53	25.906654419
2	1.1091	28.290776	82.51	25.889409951
3	1.1087	28.290100	82.49	25.873181419
4	1.1084	28.285868	82.48	25.859175864
5	1.1081	28.281542	82.46	25.841955259
10	1.1064	28.268339	82.35	25.755860337
20	1.1032	28.241714	82.21	25.613560429
30	1.1002	28.219616	82.1	25.489768871
40	1.0978	28.200909	81.97	25.377057791
50	1.0955	28.187278	81.85	25.274594956
60	1.0933	28.176772	81.75	25.183630997
70	1.0911	28.168931	81.66	25.098299493
80	1.089	28.164739	81.55	25.012527329
90	1.087	28.163687	81.48	24.944228346
100	1.085	28.165744	81.42	24.881815410

CHAPTER 7. CONCLUSION AND FUTURE WORK

7.1 Solar Cell Device Performance

From numerical simulations of device performance, it was found that replacing the n-CdS window layer of the traditional CdS-CdTe solar cell by nanopillars of CdS results in

- I. Reduction in the junction area between CdS and CdTe and hence a reduction in the total number of interface states. This is an advantage because interface states are known to lead to an increase in the effective reverse saturation current, which results in a reduction in the open circuit voltage of the solar cell.
- II. Increase in the number of photons available to the p-CdTe absorber because the CdS nanopillars embedded in Titania (or Alumina) matrix are more transmittive to the sunlight than the traditional CdS film. This is demonstrated in the experimental data of Figure [58], where optical transmission/ absorption is plotted against wavelength. These extra photons are advantageous because of the expected increase in the short circuit current and, to a lesser extent, in the open circuit voltage.
- III. Overall increase in the electrical resistance encountered by the light-generated electrons in CdTe as they travel toward the junction with the CdS nanopillars. This is because of the longer path travelled by the electrons light-generated not directly above the CdS nanopillar. This would lead to an increase in the effective series resistance of the solar cell and is thus a disadvantage; however, this increase is expected to be relatively small because the contact resistance between CdTe and the top electrode in these devices is typically much higher, and hence dominant, than the bulk resistance of the CdTe layer.

Numerical simulations were performed to investigate the effects of the above three aspects of the nanopillar device design. The effects of host nanotube parameters (pore diameter and pitch for different CdS coverages) and CdTe doping density on device performance in nanowire CdS/ CdTe solar cells were studied using SCAPS-1D simulation, and the optimum values for these parameters were obtained in order to achieve the highest efficiency.

The pore diameter was varied from a few nanometers to microns range and the pitch of the host nanotubes were varied from 100 nm to 10 mm in steps of one order of magnitude. The bulk series resistance of the device varies upon varying the pore diameter and the pitch of the nanotubes in order to obtain various fractions of CdS coverages. The optimal range for the pore diameter and the pitch for achieving the highest efficiency were found to be 2.35nm – 23.48nm for the pore diameter and the pitch ranging from 100nm – 1000nm.

The effect of CdTe doping density on the device performance was studied by varying the shallow uniform acceptor density N_A (cm^{-3}) in CdTe from 10^{14} cm^{-3} to 10^{18} cm^{-3} . It was concluded that using the nanopillars of CdS as the window layer exhibited the obvious advantages, as mentioned above, for CdTe doping density ranging from 10^{14} cm^{-3} to 10^{17} cm^{-3} . The CdTe doping density for the optimal device performance was found to be 10^{17} cm^{-3} .

Under the optimal conditions, owing to the advantages obtained from the three aspects mentioned above, the highest efficiency for nw-CdS/ CdTe structure obtained was 25.93% with short circuit current of 28.3 mA cm^{-2} , open circuit voltage of 1.11 V and fill factor of 82.55 at 300K.

7.2 Titania Nanotubes Host Matrix

Experimentally the effect of anodization voltage and fluoride ion concentration on the pore diameter and the pitch were studied for Titania nanotube host. From the experiments it is concluded that for Titania nanotubes fabricated in ethylene glycol-based electrolyte,

- (i) In the range of 0.3 mL to 2 mL of ammonium fluoride content, pore diameter of the titania nanotube matrix is rather insensitive to the ammonium fluoride concentration.
- (ii) In the range of 0.3 mL to 2 mL of ammonium fluoride content, pitch (or interpore distance) of the titania nanotube matrix is rather insensitive to the ammonium fluoride concentration.
- (iii) For the case of ethylene glycol based electrolyte, there is an optimum anodization voltage at which the pore diameter is maximum for a fixed fluoride ion concentration.
- (iv) An increase in anodization voltage from 50 V to 60 V leads to a substantial reduction in the pitch of the titania nanotube matrix.
- (v) Thus, anodization voltage is the more effective parameter, which can be tailored and optimized to fabricate Titania Nanotube arrays of desired porosity.

7.3 Suggestions for Future Work

- (i) Similar study can be done on a host other than nanoporous Titania template, For example, Anodized Aluminum Oxide (AAO).
- (ii) n-CdS window layer can be replaced with an n-CdZnS layer.
- (iii) Further experiments can be performed to verify and elucidate the results obtained from this numerical study of solar cell device performance.

APPENDIX

Table A.1 Effect of CdS Coverage on Voc, Jsc, FF and Efficiency for 10^{17} doping,

Pitch = 10^2 nm

%CdS Coverage	Voc	Jsc	FF	Efficiency
0.0001	1.1098	28.2986	82.55	25.9255
0.001	1.1098	28.2986	82.55	25.9255
0.01	1.1098	28.2986	82.55	25.9254
0.1	1.1097	28.2983	82.55	25.9228
1	1.1094	28.2951	82.53	25.9067
2	1.1091	28.2908	82.51	25.8894
3	1.1087	28.2901	82.49	25.8732
4	1.1084	28.2859	82.48	25.8592
5	1.1081	28.2815	82.46	25.8420
10	1.1064	28.2683	82.35	25.7559
20	1.1032	28.2417	82.21	25.6136
30	1.1002	28.2196	82.1	25.4898
40	1.0978	28.2009	81.97	25.3771
50	1.0955	28.1873	81.85	25.2746
60	1.0933	28.1768	81.75	25.1836
70	1.0911	28.1689	81.66	25.0983
80	1.089	28.1647	81.55	25.0125
90	1.087	28.1637	81.48	24.9442

100	1.085	28.1657	81.42	24.8818
------------	-------	---------	-------	---------

Table A.2 Effect of CdS Coverage on Voc, Jsc, FF and Efficiency for 10¹⁶ CdTe**doping, Pitch = 10² nm**

%CdS Coverage	Voc	Jsc	FF	Efficiency
0.0001	1.0563	28.2695	81.99	24.4831
0.001	1.0563	28.2695	81.99	24.4831
0.01	1.0563	28.2694	81.99	24.4830
0.1	1.0563	28.2690	81.98	24.4796
1	1.0561	28.2643	81.98	24.4710
2	1.0559	28.2584	81.98	24.4612
3	1.0557	28.2559	81.97	24.4515
4	1.0562	28.2490	81.98	24.4600
5	1.0562	28.2428	81.98	24.4547
10	1.0561	28.2200	81.97	24.4297
20	1.0558	28.1749	81.96	24.3807
30	1.0555	28.1349	81.95	24.3362
40	1.0553	28.0987	81.94	24.2973
50	1.055	28.0682	81.92	24.2581
60	1.0548	28.0412	81.91	24.2273
70	1.0545	28.0174	81.9	24.1968
80	1.0543	27.9976	81.89	24.1722
90	1.054	27.9814	81.87	24.1455
100	1.0538	27.9688	81.86	24.1270

**Table A.3 Effect of CdS Coverage on Voc, Jsc, FF and Efficiency for 10¹⁵ CdTe
doping, Pitch = 10² nm**

%CdS Coverage	Voc	Jsc	FF	Efficiency
0.0001	1.0057	28.2703	81.02	23.0352
0.001	1.0057	28.2703	81.02	23.0352
0.01	1.0057	28.2703	81.02	23.0351
0.1	1.0057	28.2697	81.02	23.0347
1	1.0057	28.2642	81.02	23.0302
2	1.0057	28.2574	81.02	23.0246
3	1.0057	28.2539	81.02	23.0218
4	1.0057	28.2472	81.02	23.0163
5	1.0057	28.2404	81.02	23.0108
10	1.0056	28.2142	81.02	22.9872
20	1.0055	28.1627	81.03	22.9457
30	1.0055	28.1164	81.03	22.9080
40	1.0054	28.0741	81.03	22.8713
50	1.0053	28.0377	81.04	22.8421
60	1.0052	28.0049	81.04	22.8132
70	1.0051	27.9754	81.04	22.7869
80	1.0051	27.9501	81.04	22.7663
90	1.005	27.9286	81.04	22.7465
100	1.005	27.9107	81.04	22.7319

Table A.4 Effect of CdS Coverage on Voc, Jsc, FF and Efficiency for 10¹⁴ CdTe**doping, Pitch = 10² nm**

%CdS Coverage	Voc	Jsc	FF	Efficiency
0.0001	0.9808	28.2996	78.1	21.6776
0.001	0.9808	28.2996	78.1	21.6776
0.01	0.9808	28.2996	78.1	21.6776
0.1	0.9808	28.2990	78.1	21.6772
1	0.9808	28.2933	78.1	21.6728
2	0.9808	28.2862	78.1	21.6674
3	0.9808	28.2825	78.1	21.6645
4	0.9808	28.2755	78.1	21.6592
5	0.9808	28.2685	78.11	21.6566
10	0.9807	28.2412	78.11	21.6335
20	0.9806	28.1874	78.12	21.5928
30	0.9805	28.1388	78.13	21.5562
40	0.9804	28.0944	78.14	21.5227
50	0.9804	28.0558	78.15	21.4959
60	0.9803	28.0210	78.15	21.4670
70	0.9802	27.9895	78.16	21.4434
80	0.9801	27.9622	78.17	21.4231
90	0.9801	27.9387	78.17	21.4051
100	0.98	27.9190	78.2	21.3960

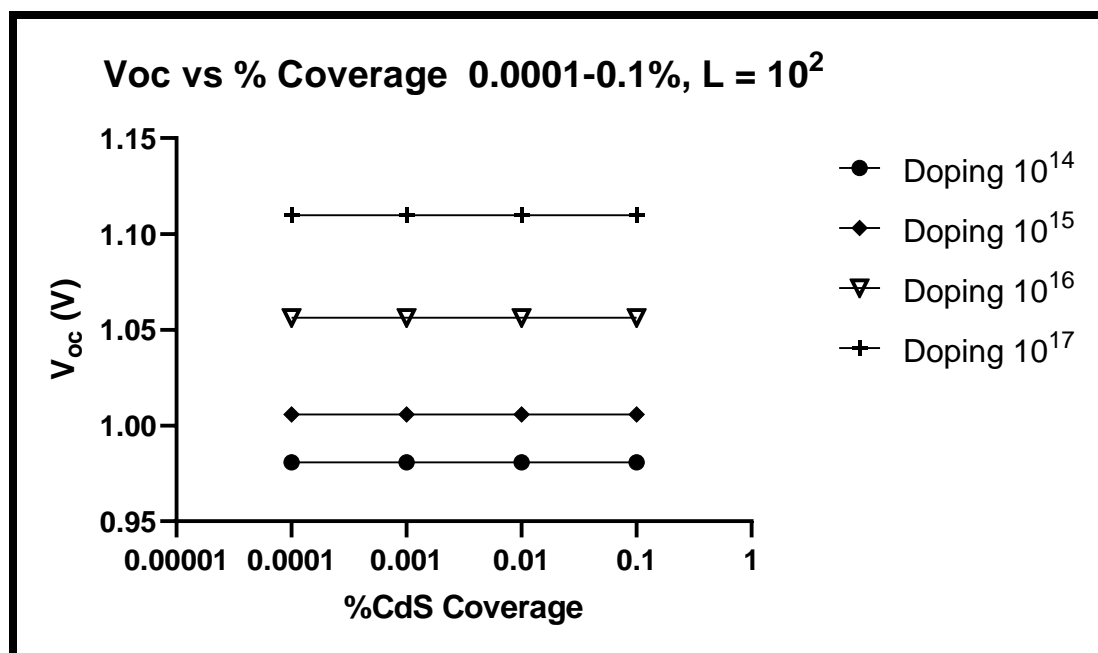


Figure A.1 Voc vs 0.0001-0.1% CdS Coverage Interpore Distance 100nm

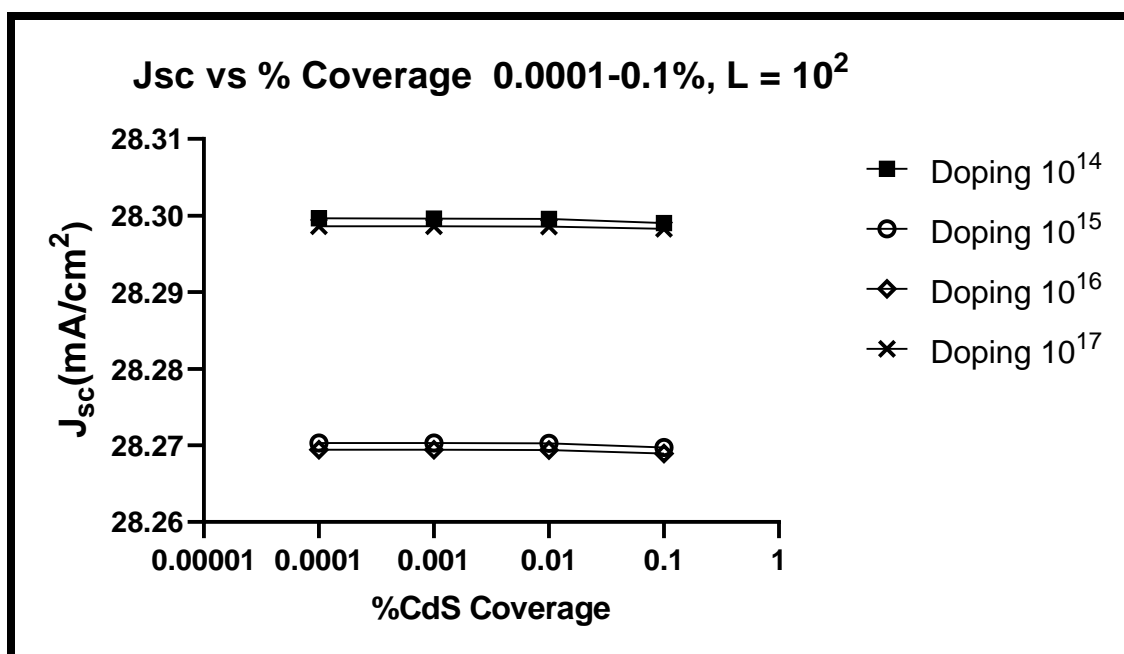


Figure A.2 Jsc vs 0.0001-0.1% CdS Coverage Interpore Distance 100nm

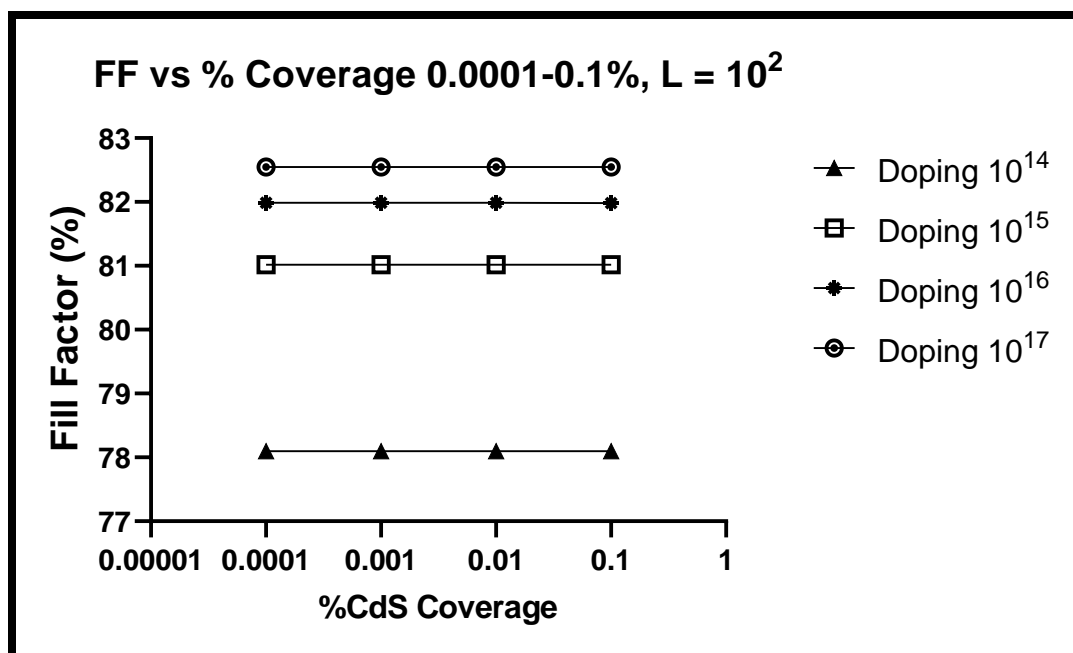


Figure A.3 FF vs 0.0001-0.1% CdS Coverage Interpore Distance 100nm

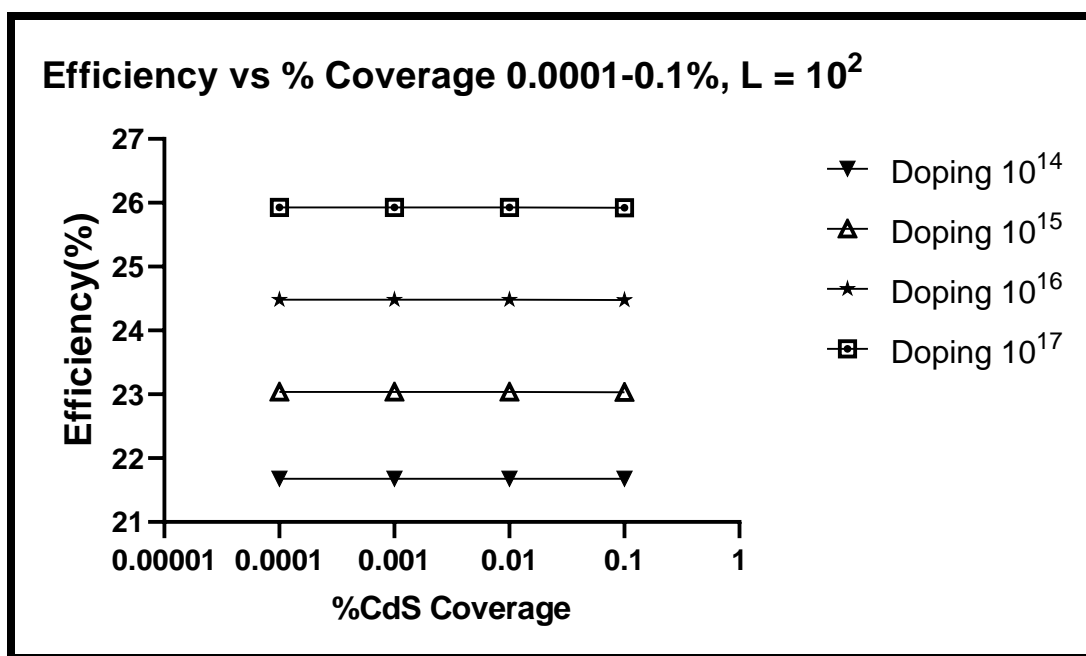


Figure A.4 Efficiency vs 0.0001-0.1% CdS Coverage Interpore Distance 100nm

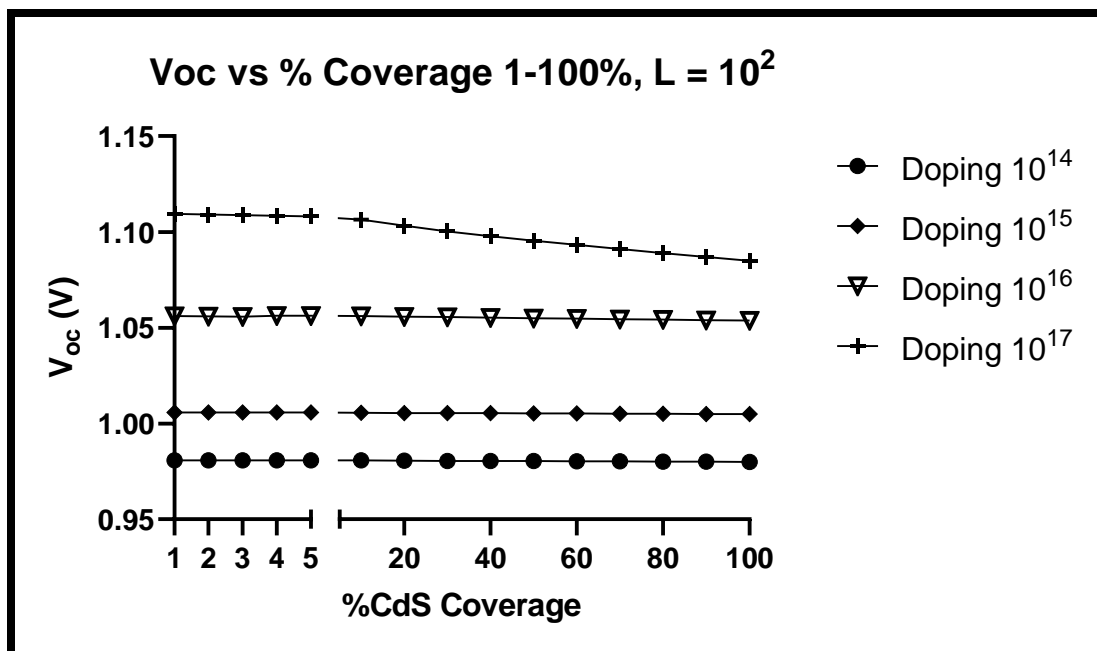


Figure A.5 Voc vs 1-100% CdS Coverage Interpore Distance 100nm

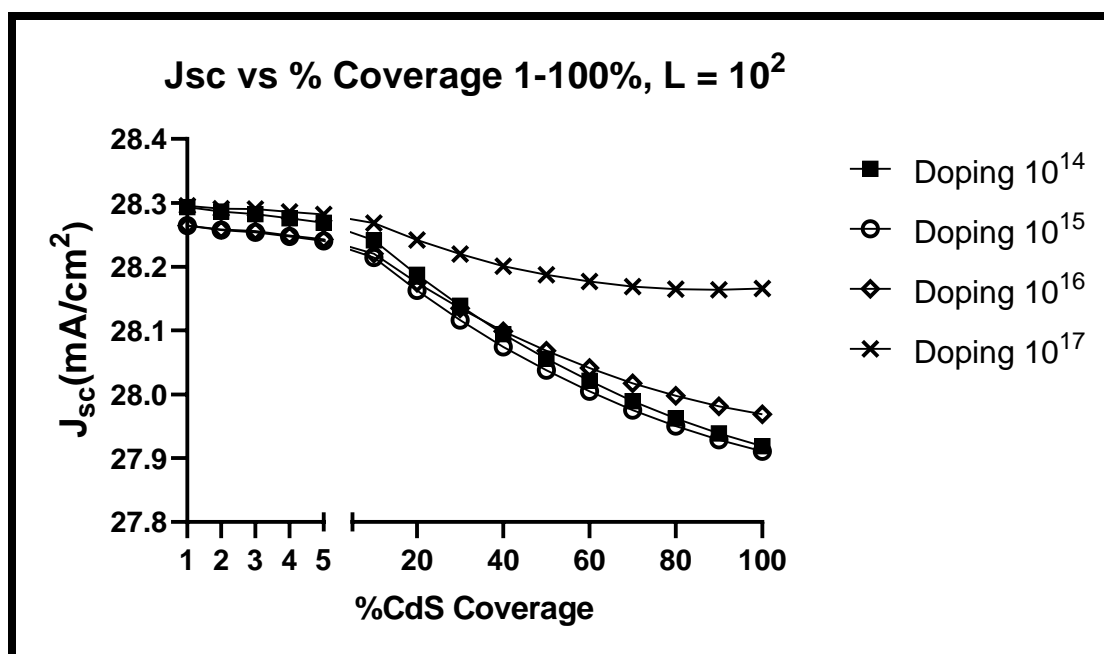


Figure A.6 Jsc vs 1-100% CdS Coverage Interpore Distance 100nm

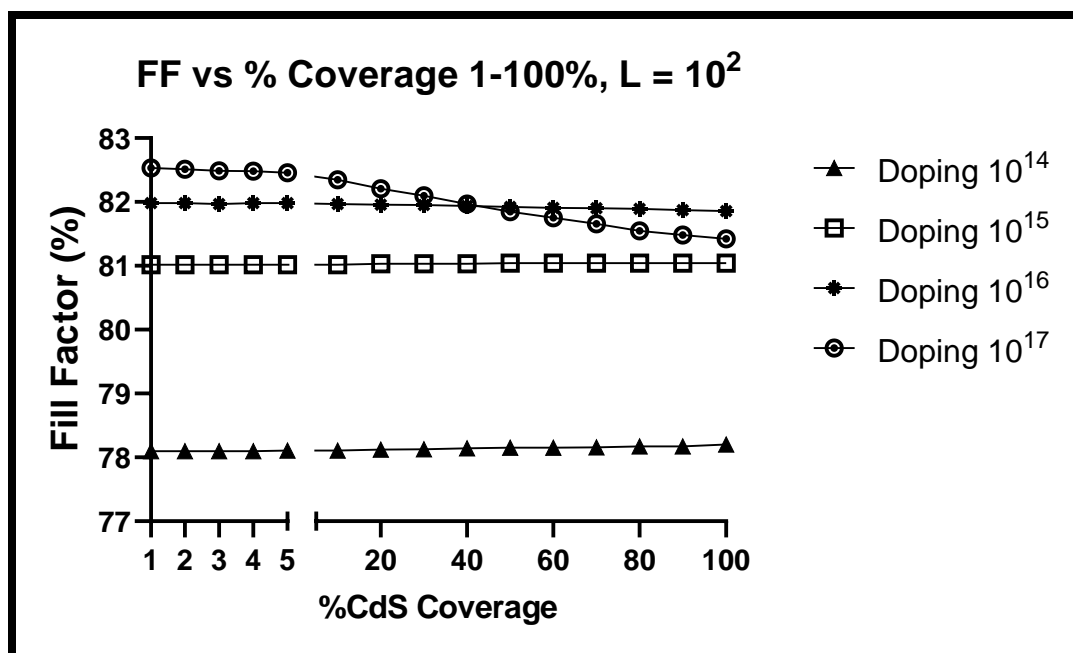


Figure A.7 FF vs 1-100% CdS Coverage Interpore Distance 100nm

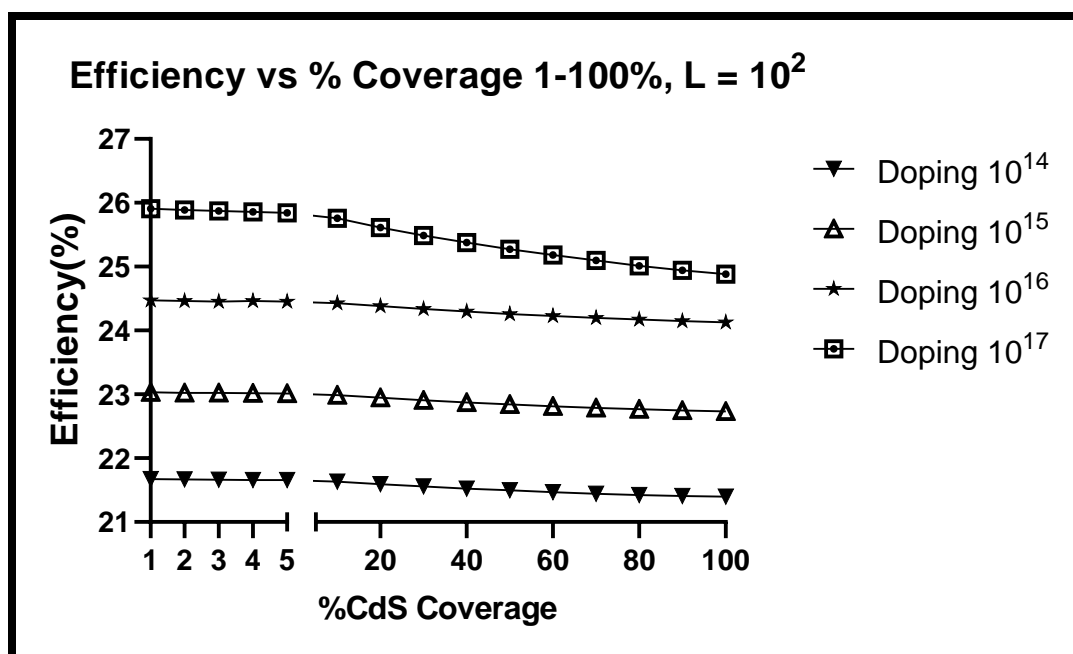


Figure A.8 Efficiency vs 1-100% CdS Coverage Interpore Distance 100nm

Table A.5 Effect of CdS Coverage on Voc, Jsc, FF and Efficiency for 10^{17} CdTe**doping, Pitch = 10^3 nm**

%CdS Coverage	Voc	Jsc	FF	Efficiency
0.0001	1.1098	28.2986	82.55	25.9255
0.001	1.1098	28.2986	82.55	25.9255
0.01	1.1098	28.2986	82.55	25.9254
0.1	1.1097	28.2983	82.55	25.9228
1	1.1094	28.2951	82.53	25.9067
2	1.1091	28.2908	82.51	25.8894
3	1.1087	28.2901	82.49	25.8732
4	1.1084	28.2859	82.48	25.8592
5	1.1081	28.2815	82.46	25.8420
10	1.1064	28.2683	82.35	25.7559
20	1.1032	28.2417	82.21	25.6136
30	1.1002	28.2196	82.1	25.4898
40	1.0978	28.2009	81.97	25.3771
50	1.0955	28.1873	81.85	25.2746
60	1.0933	28.1768	81.75	25.1836
70	1.0911	28.1689	81.66	25.0983
80	1.089	28.1647	81.55	25.0125
90	1.087	28.1637	81.48	24.9442
100	1.085	28.1657	81.42	24.8818

Table A.6 Effect of CdS Coverage on Voc, Jsc, FF and Efficiency for 10¹⁶ CdTe**doping, Pitch = 10³ nm**

%CdS Coverage	Voc	Jsc	FF	Efficiency
0.0001	1.0563	28.2695	81.99	24.4831
0.001	1.0563	28.2695	81.99	24.4831
0.01	1.0563	28.2694	81.99	24.4830
0.1	1.0563	28.2690	81.98	24.4796
1	1.0561	28.2643	81.98	24.4710
2	1.0559	28.2584	81.98	24.4612
3	1.0557	28.2559	81.97	24.4515
4	1.0562	28.2490	81.98	24.4600
5	1.0562	28.2428	81.98	24.4547
10	1.0561	28.2200	81.97	24.4297
20	1.0558	28.1749	81.96	24.3807
30	1.0555	28.1349	81.95	24.3362
40	1.0553	28.0987	81.94	24.2973
50	1.055	28.0682	81.92	24.2581
60	1.0548	28.0412	81.91	24.2273
70	1.0545	28.0174	81.9	24.1968
80	1.0543	27.9976	81.89	24.1722
90	1.054	27.9814	81.87	24.1455
100	1.0538	27.9688	81.86	24.1270

Table A.7 Effect of CdS Coverage on Voc, Jsc, FF and Efficiency for 10^{15} CdTe doping, Pitch = 10^3 nm

%CdS Coverage	Voc	Jsc	FF	Efficiency
0.0001	1.0057	28.2703	81.02	23.0352
0.001	1.0057	28.2703	81.02	23.0352
0.01	1.0057	28.2703	81.02	23.0351
0.1	1.0057	28.2697	81.02	23.0347
1	1.0057	28.2642	81.02	23.0302
2	1.0057	28.2574	81.02	23.0246
3	1.0057	28.2539	81.02	23.0218
4	1.0057	28.2472	81.02	23.0163
5	1.0057	28.2404	81.02	23.0108
10	1.0056	28.2142	81.02	22.9872
20	1.0055	28.1627	81.03	22.9457
30	1.0055	28.1164	81.03	22.9080
40	1.0054	28.0741	81.03	22.8713
50	1.0053	28.0377	81.04	22.8421
60	1.0052	28.0049	81.04	22.8132
70	1.0051	27.9754	81.04	22.7869
80	1.0051	27.9501	81.04	22.7663
90	1.005	27.9286	81.04	22.7465
100	1.005	27.9107	81.04	22.7319

Table A.8 Effect of CdS Coverage on Voc, Jsc, FF and Efficiency for 10¹⁴ CdTe**doping, Pitch = 10³ nm**

%CdS Coverage	Voc	Jsc	FF	Efficiency
0.0001	0.9808	28.2996	78.1	21.6776
0.001	0.9808	28.2996	78.1	21.6776
0.01	0.9808	28.2996	78.1	21.6776
0.1	0.9808	28.2990	78.1	21.6772
1	0.9808	28.2933	78.1	21.6728
2	0.9808	28.2862	78.1	21.6674
3	0.9808	28.2825	78.1	21.6645
4	0.9808	28.2755	78.1	21.6592
5	0.9808	28.2685	78.1	21.6538
10	0.9807	28.2412	78.11	21.6335
20	0.9806	28.1874	78.12	21.5928
30	0.9805	28.1388	78.13	21.5562
40	0.9804	28.0944	78.14	21.5227
50	0.9804	28.0558	78.14	21.4931
60	0.9803	28.0210	78.15	21.4670
70	0.9802	27.9895	78.16	21.4434
80	0.9801	27.9622	78.16	21.4203
90	0.9801	27.9387	78.17	21.4051
100	0.98	27.9190	78.2	21.3960

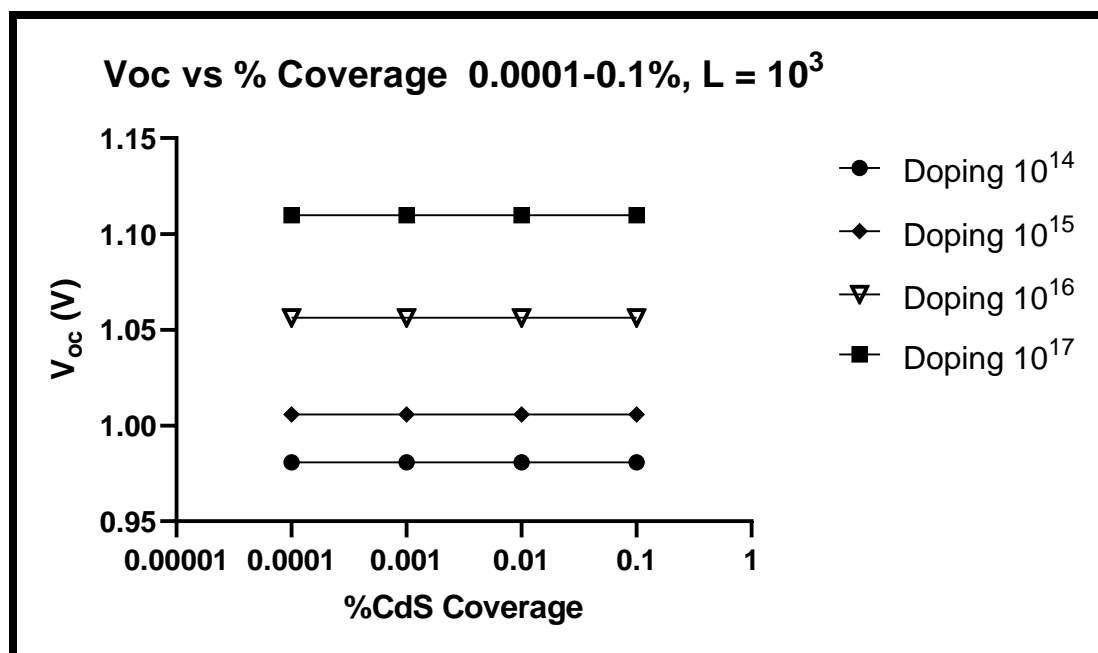


Figure A.9 Voc vs 0.0001-0.1% CdS Coverage Interpore Distance $1\mu\text{m}$

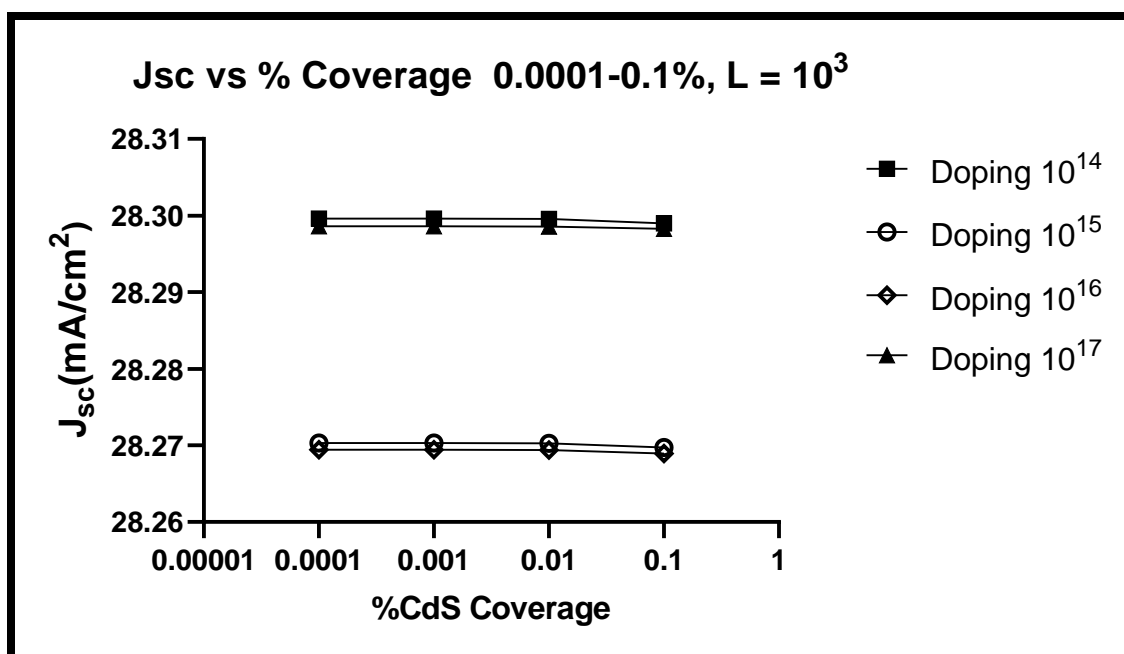


Figure A.10 Jsc vs 0.0001-0.1% CdS Coverage Interpore Distance $1\mu\text{m}$

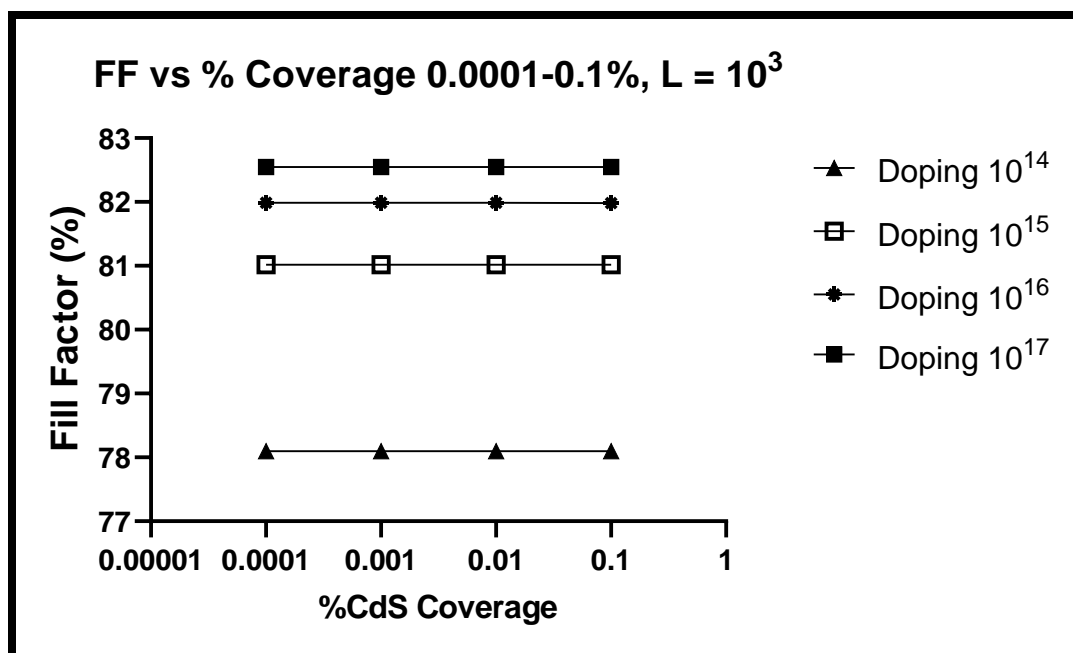


Figure A.11 FF vs 0.0001-0.1% CdS Coverage Interpore Distance $1\mu\text{m}$

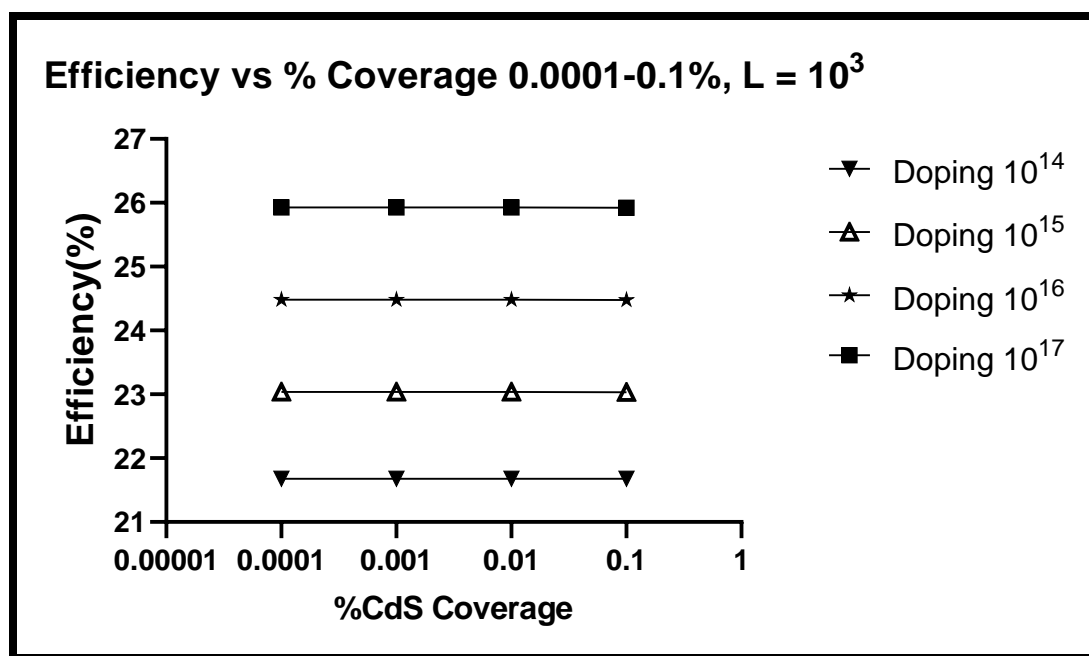


Figure A.12 Efficiency vs 0.0001-0.1% CdS Coverage Interpore Distance $1\mu\text{m}$

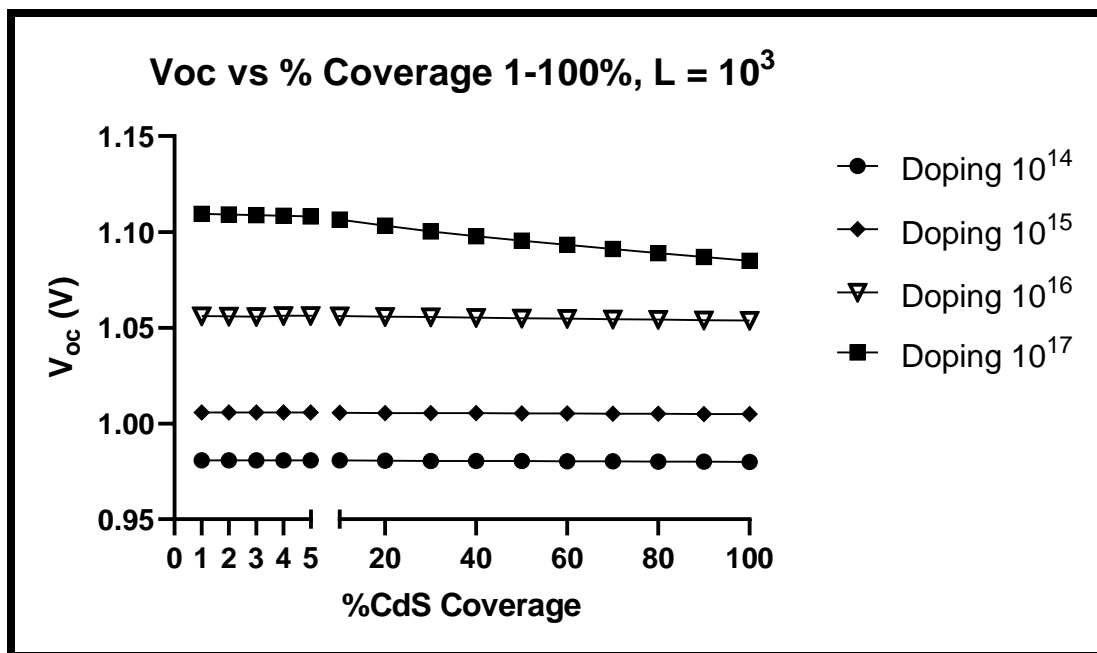


Figure A.13 Voc vs 1-100% CdS Coverage Interpore Distance $1\mu\text{m}$

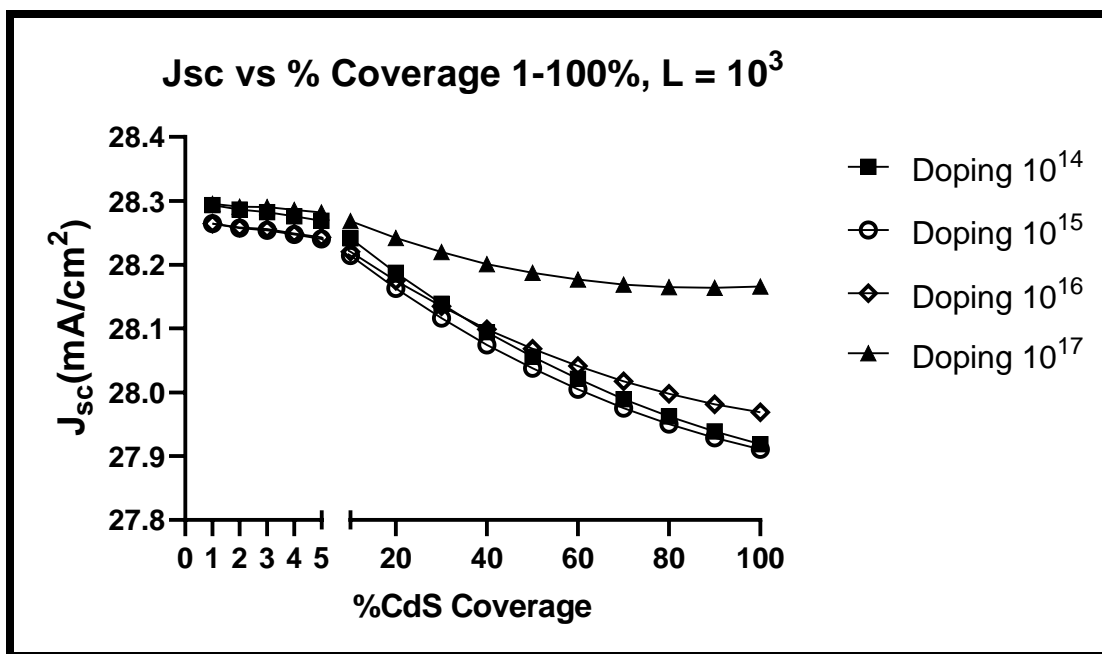


Figure A.14 Jsc vs 1-100% CdS Coverage Interpore Distance $1\mu\text{m}$

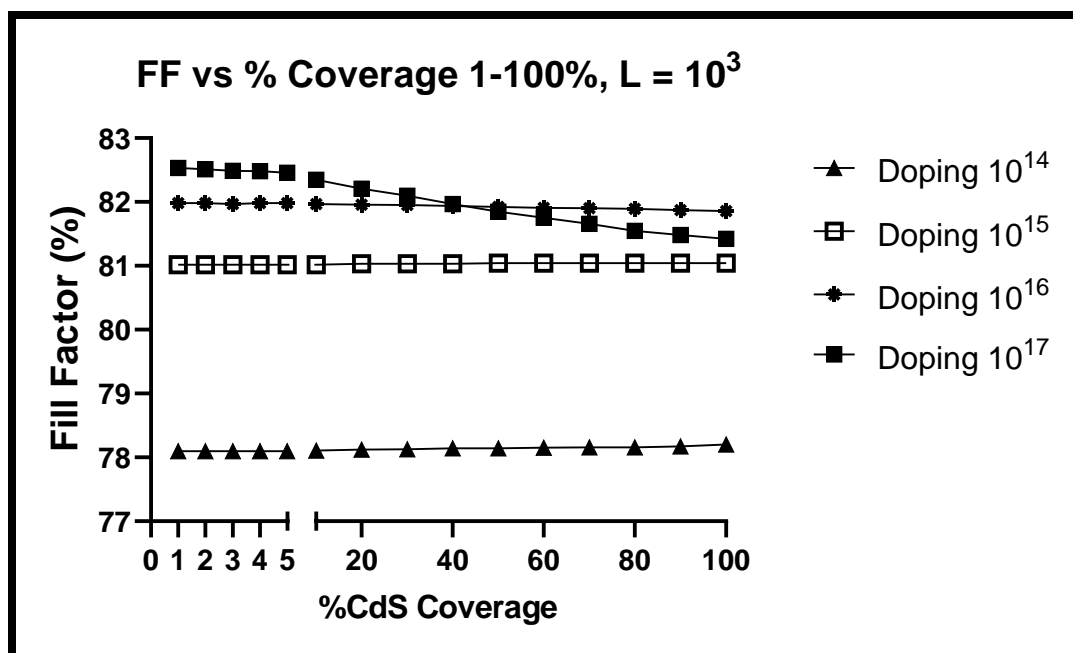


Figure A.15 FF vs 1-100% CdS Coverage Interpore Distance $1\mu\text{m}$

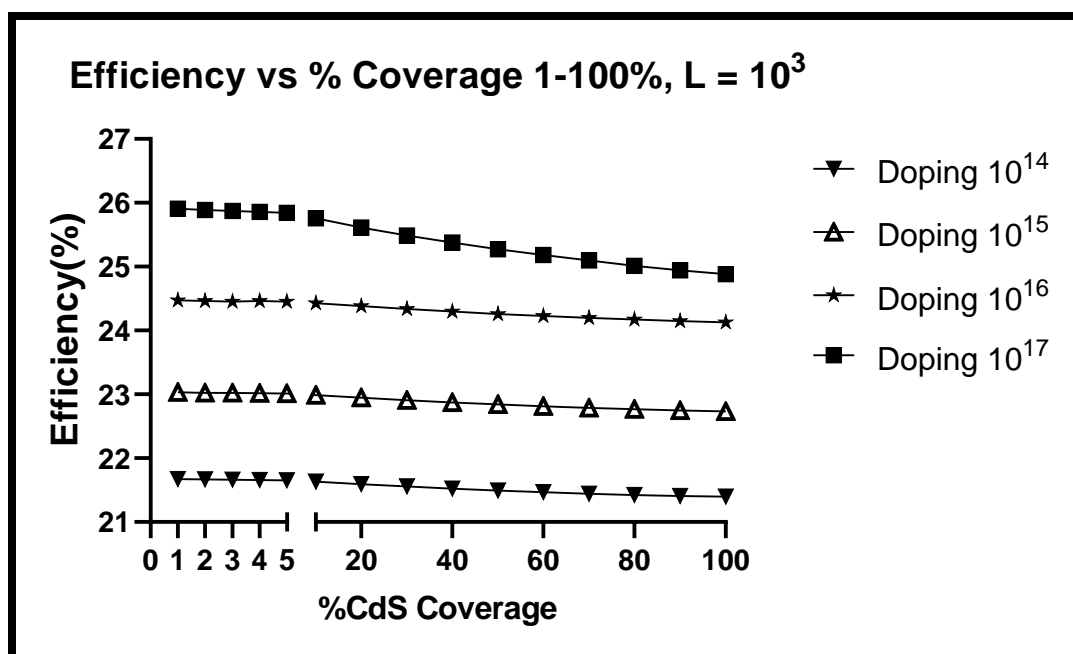


Figure A.16 Efficiency vs 1-100% CdS Coverage Interpore Distance $1\mu\text{m}$

**Table A.9 Effect of CdS Coverage on Voc, Jsc, FF and Efficiency for 10^{17} CdTe
doping, Pitch = 10^4 nm**

%CdS Coverage	Voc	Jsc	FF	Efficiency
0.0001	1.1098	28.2986	82.55	25.9255
0.001	1.1098	28.2986	82.55	25.9255
0.01	1.1098	28.2986	82.55	25.9254
0.1	1.1097	28.2983	82.55	25.9228
1	1.1094	28.2951	82.53	25.9067
2	1.1091	28.2908	82.51	25.8894
3	1.1087	28.2901	82.49	25.8732
4	1.1084	28.2859	82.48	25.8592
5	1.1081	28.2815	82.46	25.8420
10	1.1064	28.2683	82.35	25.7559
20	1.1032	28.2417	82.21	25.6136
30	1.1002	28.2196	82.1	25.4898
40	1.0978	28.2009	81.97	25.3771
50	1.0955	28.1873	81.85	25.2746
60	1.0933	28.1768	81.75	25.1836
70	1.0911	28.1689	81.66	25.0983
80	1.089	28.1647	81.55	25.0125
90	1.087	28.1637	81.48	24.9442
100	1.085	28.1657	81.42	24.8818

Table A.10 Effect of CdS Coverage on Voc, Jsc, FF and Efficiency for 10¹⁶ CdTe**doping, Pitch = 10⁴ nm**

%CdS Coverage	Voc	Jsc	FF	Efficiency
0.0001	1.0563	28.2695	81.98	24.4801
0.001	1.0563	28.2695	81.98	24.4801
0.01	1.0563	28.2694	81.98	24.4800
0.1	1.0563	28.2690	81.98	24.4796
1	1.0561	28.2643	81.98	24.4710
2	1.0559	28.2584	81.98	24.4612
3	1.0557	28.2559	81.97	24.4515
4	1.0562	28.2490	81.98	24.4600
5	1.0562	28.2428	81.98	24.4547
10	1.0561	28.2200	81.97	24.4297
20	1.0558	28.1749	81.96	24.3807
30	1.0555	28.1349	81.95	24.3362
40	1.0553	28.0987	81.94	24.2973
50	1.055	28.0682	81.92	24.2581
60	1.0548	28.0412	81.91	24.2273
70	1.0545	28.0174	81.9	24.1968
80	1.0543	27.9976	81.89	24.1722
90	1.054	27.9814	81.87	24.1455
100	1.0538	27.9688	81.86	24.1270

**Table A.11 Effect of CdS Coverage on Voc, Jsc, FF and Efficiency for 10¹⁵ CdTe
doping, Pitch = 10⁴ nm**

%CdS Coverage	Voc	Jsc	FF	Efficiency
0.0001	1.0057	28.2703	81.01	23.0323
0.001	1.0057	28.2703	81.01	23.0323
0.01	1.0057	28.2702	81.01	23.0323
0.1	1.0057	28.2697	81.01	23.0318
1	1.0057	28.2642	81.01	23.0273
2	1.0057	28.2574	81.01	23.0218
3	1.0057	28.2539	81.01	23.0189
4	1.0057	28.2472	81.02	23.0163
5	1.0057	28.2404	81.02	23.0108
10	1.0056	28.2142	81.02	22.9872
20	1.0055	28.1627	81.02	22.9429
30	1.0055	28.1164	81.03	22.9080
40	1.0054	28.0741	81.03	22.8713
50	1.0053	28.0376	81.03	22.8393
60	1.0052	28.0049	81.03	22.8104
70	1.0051	27.9754	81.04	22.7869
80	1.0051	27.9501	81.04	22.7663
90	1.005	27.9286	81.04	22.7465
100	1.005	27.9107	81.04	22.7319

**Table A.12 Effect of CdS Coverage on Voc, Jsc, FF and Efficiency for 10¹⁴ CdTe
doping, Pitch = 10⁴ nm**

%CdS Coverage	Voc	Jsc	FF	Efficiency
0.0001	0.9808	28.2995	78.06	21.6664
0.001	0.9808	28.2995	78.06	21.6664
0.01	0.9808	28.2994	78.06	21.6664
0.1	0.9808	28.2988	78.06	21.6660
1	0.9808	28.2931	78.06	21.6616
2	0.9808	28.2861	78.06	21.6562
3	0.9808	28.2823	78.06	21.6533
4	0.9808	28.2754	78.07	21.6508
5	0.9808	28.2684	78.07	21.6454
10	0.9807	28.2411	78.08	21.6251
20	0.9806	28.1873	78.09	21.5844
30	0.9805	28.1387	78.1	21.5478
40	0.9804	28.0943	78.11	21.5143
50	0.9804	28.0557	78.12	21.4876
60	0.9803	28.0209	78.13	21.4615
70	0.9802	27.9894	78.14	21.4379
80	0.9801	27.9621	78.14	21.4148
90	0.9801	27.9386	78.15	21.3995
100	0.98	27.9190	78.2	21.3960

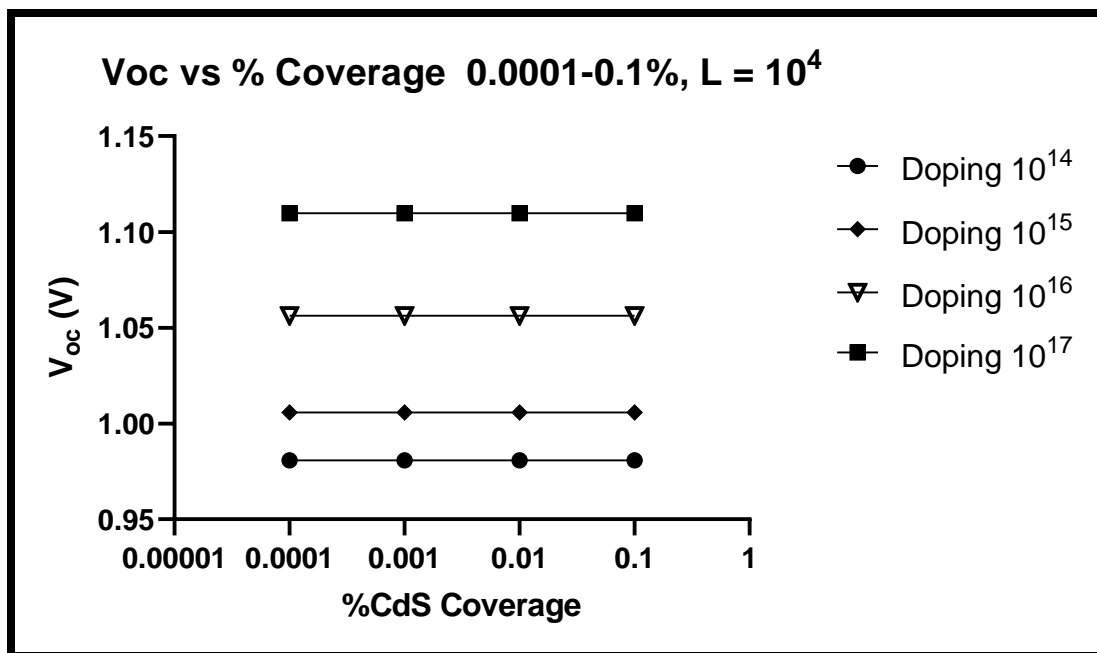


Figure A.17 Voc vs 0.0001-0.1% CdS Coverage Interpore Distance $10\mu\text{m}$

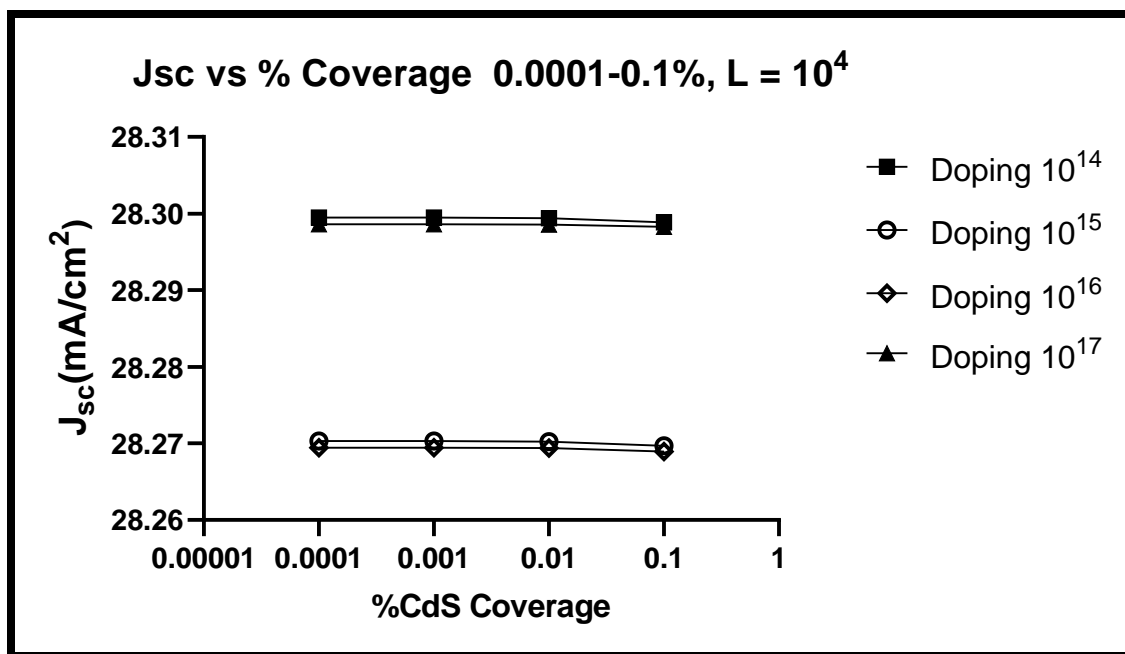


Figure A.18 Jsc vs 0.0001-0.1% CdS Coverage Interpore Distance $10\mu\text{m}$

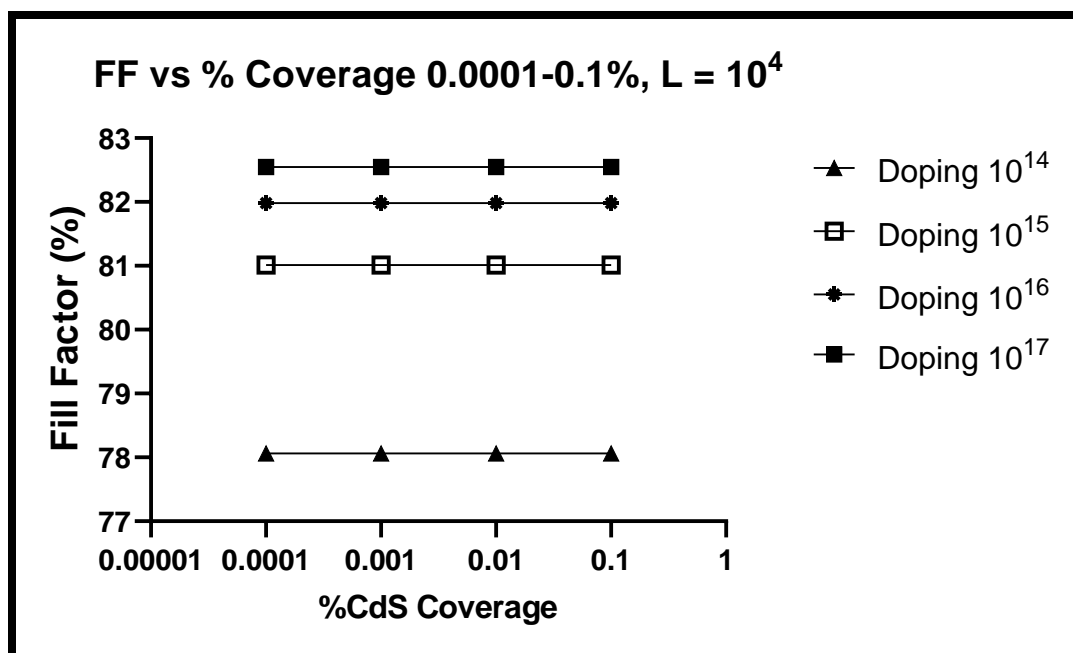


Figure A.19 FF vs 0.0001-0.1% CdS Coverage Interpore Distance $10\mu\text{m}$

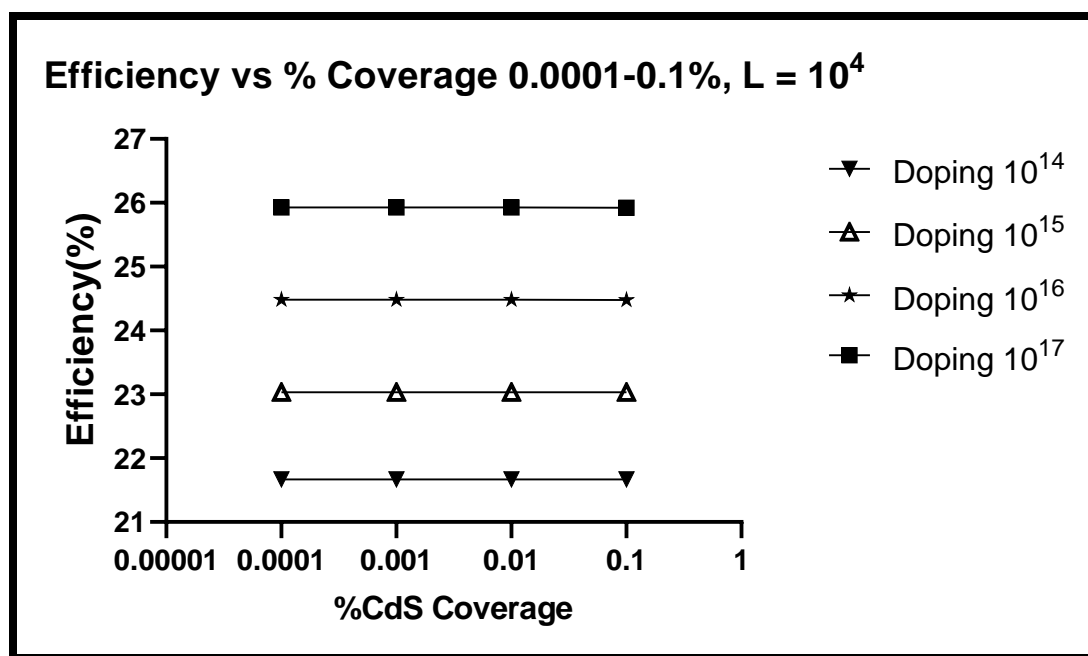


Figure A.20 Efficiency vs 0.0001-0.1% CdS Coverage Interpore Distance $10\mu\text{m}$

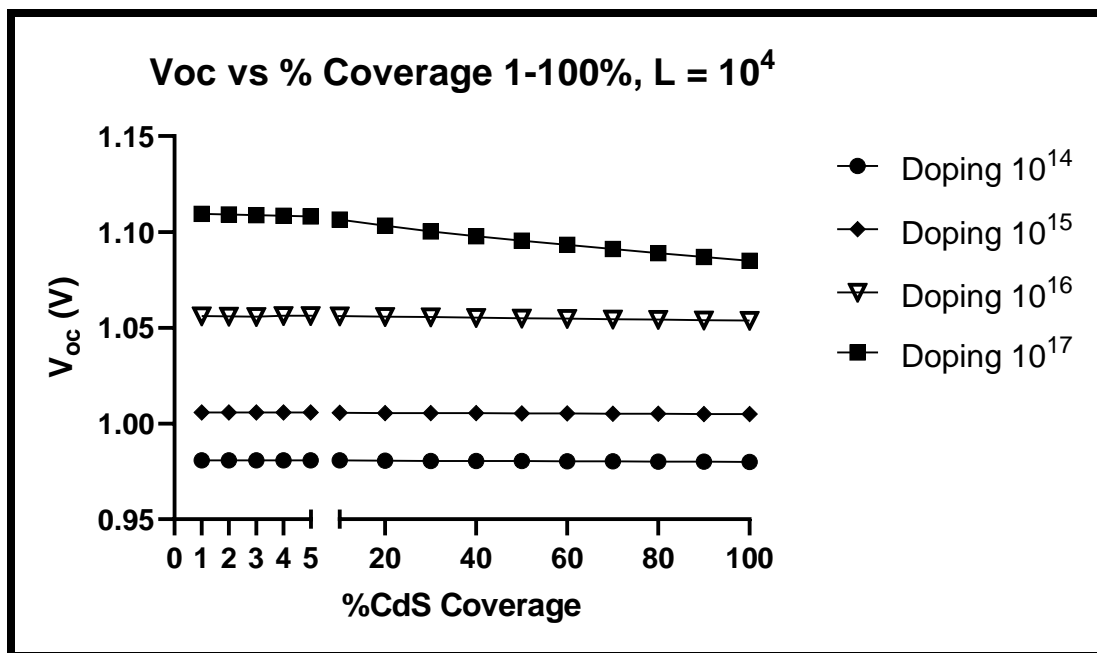


Figure A.21 Voc vs 1-100% CdS Coverage Interpore Distance $10\mu\text{m}$

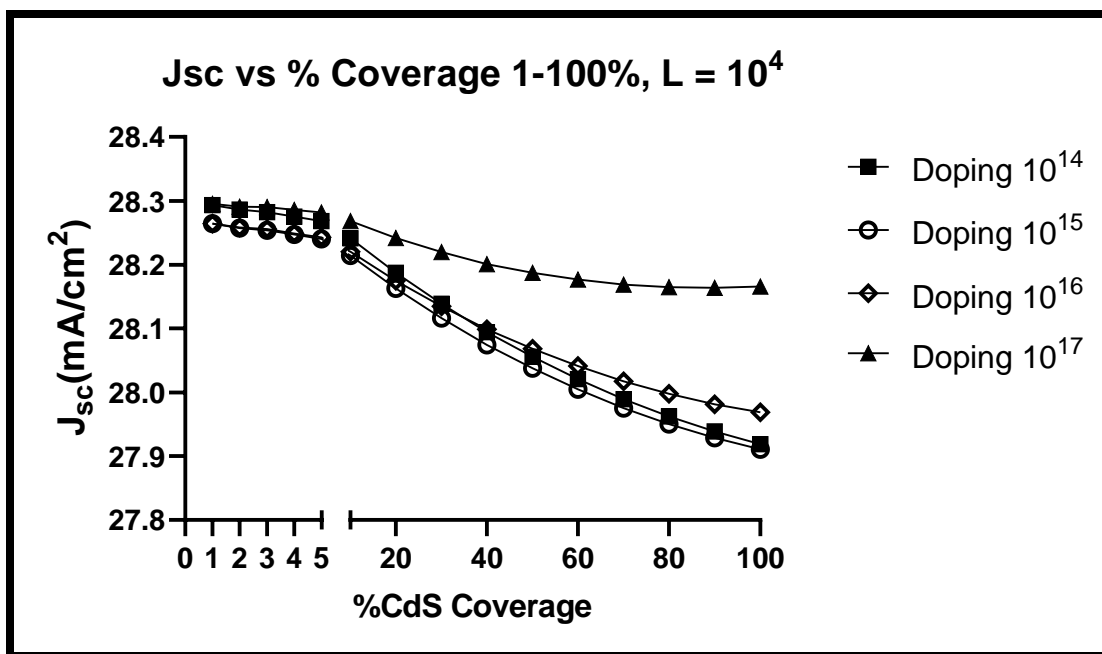


Figure A.22 Jsc vs 1-100% CdS Coverage Interpore Distance $10\mu\text{m}$

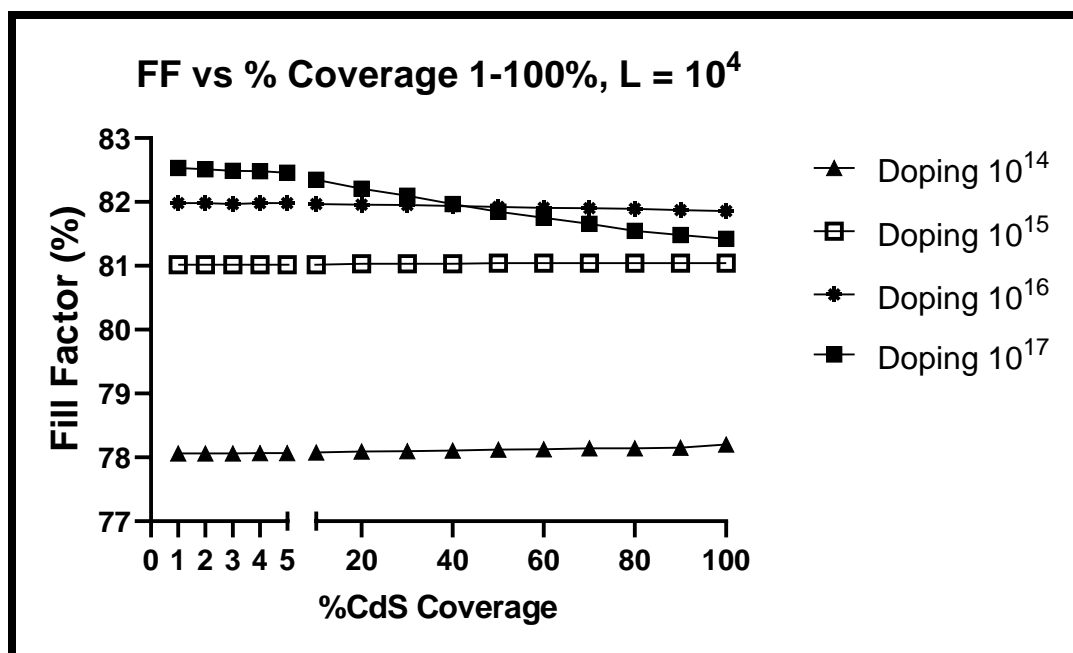


Figure A.23 FF vs 1-100% CdS Coverage Interpore Distance $10\mu\text{m}$

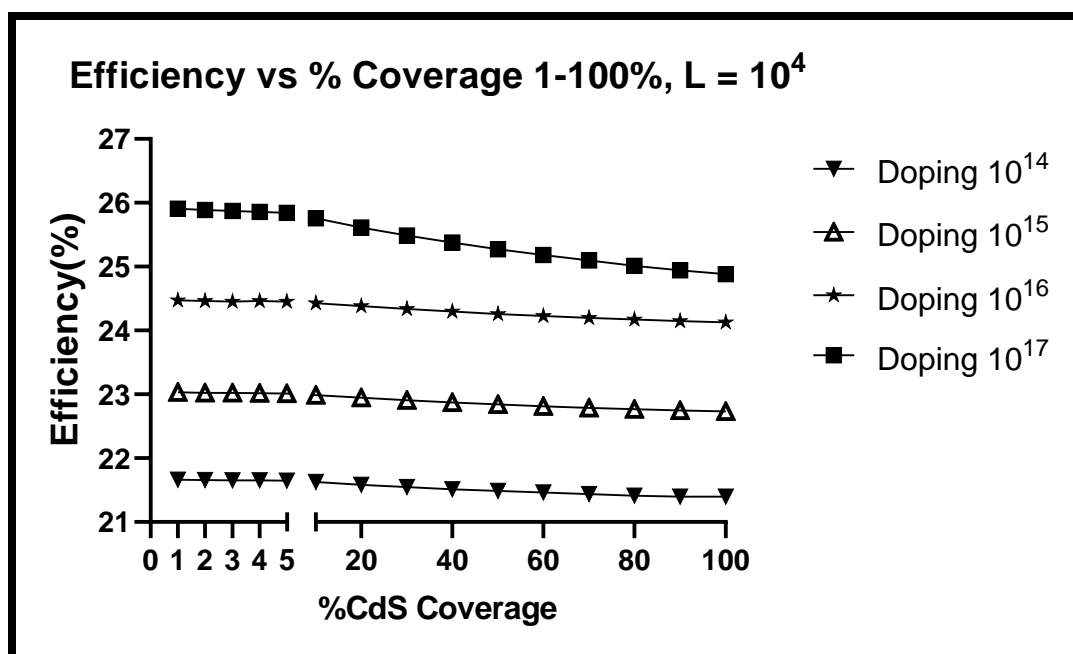


Figure A.24 Efficiency vs 1-100% CdS Coverage Interpore Distance $10\mu\text{m}$

**Table A.13 Effect of CdS Coverage on Voc, Jsc, FF and Efficiency for 10¹⁷ CdTe
doping, Pitch = 10⁵ nm**

%CdS Coverage	Voc	Jsc	FF	Efficiency
0.0001	1.1098	28.2986	82.55	25.9255
0.001	1.1098	28.2986	82.55	25.9255
0.01	1.1098	28.2986	82.55	25.9254
0.1	1.1097	28.2982	82.55	25.9228
1	1.1094	28.2951	82.53	25.9066
2	1.1091	28.2908	82.51	25.8894
3	1.1087	28.2901	82.49	25.8732
4	1.1084	28.2859	82.47	25.8560
5	1.1081	28.2815	82.46	25.8419
10	1.1064	28.2683	82.35	25.7558
20	1.1032	28.2417	82.21	25.6135
30	1.1002	28.2196	82.1	25.4898
40	1.0978	28.2009	81.96	25.3739
50	1.0955	28.1873	81.85	25.2746
60	1.0933	28.1768	81.75	25.1836
70	1.0911	28.1689	81.66	25.0983
80	1.089	28.1647	81.55	25.0125
90	1.087	28.1637	81.48	24.9442
100	1.085	28.1657	81.42	24.8818

Table A.14 Effect of CdS Coverage on Voc, Jsc, FF and Efficiency for 10¹⁶ CdTe**doping, Pitch = 10⁵ nm**

%CdS Coverage	Voc	Jsc	FF	Efficiency
0.0001	1.0563	28.2694	81.98	24.4801
0.001	1.0563	28.2694	81.98	24.4801
0.01	1.0563	28.2694	81.98	24.4800
0.1	1.0563	28.2689	81.98	24.4796
1	1.0561	28.2643	81.98	24.4709
2	1.0559	28.2584	81.97	24.4582
3	1.0557	28.2559	81.97	24.4514
4	1.0562	28.2490	81.98	24.4600
5	1.0562	28.2428	81.98	24.4547
10	1.0561	28.2200	81.97	24.4297
20	1.0558	28.1749	81.96	24.3807
30	1.0555	28.1349	81.95	24.3362
40	1.0553	28.0987	81.93	24.2943
50	1.055	28.0682	81.92	24.2581
60	1.0548	28.0412	81.91	24.2273
70	1.0545	28.0174	81.9	24.1968
80	1.0543	27.9976	81.88	24.1692
90	1.054	27.9814	81.87	24.1455
100	1.0538	27.9688	81.86	24.1270

**Table A.15 Effect of CdS Coverage on Voc, Jsc, FF and Efficiency for 10¹⁵ CdTe
doping, Pitch = 10⁵ nm**

%CdS Coverage	Voc	Jsc	FF	Efficiency
0.0001	1.0057	28.2702	80.97	23.0208
0.001	1.0057	28.2701	80.97	23.0208
0.01	1.0057	28.2701	80.98	23.0236
0.1	1.0057	28.2696	80.98	23.0232
1	1.0057	28.2641	80.98	23.0187
2	1.0057	28.2572	80.98	23.0131
3	1.0057	28.2537	80.98	23.0103
4	1.0057	28.2470	80.98	23.0048
5	1.0057	28.2402	80.98	22.9993
10	1.0056	28.2141	80.99	22.9786
20	1.0055	28.1626	80.99	22.9343
30	1.0055	28.1163	81	22.8994
40	1.0054	28.0740	81.01	22.8655
50	1.0053	28.0376	81.01	22.8336
60	1.0052	28.0048	81.01	22.8047
70	1.0051	27.9753	81.02	22.7812
80	1.0051	27.9500	81.02	22.7606
90	1.005	27.9285	81.02	22.7408
100	1.005	27.9107	81.04	22.7319

**Table A.16 Effect of CdS Coverage on Voc, Jsc, FF and Efficiency for 10¹⁴ CdTe
doping, Pitch = 10⁵ nm**

%CdS Coverage	Voc	Jsc	FF	Efficiency
0.0001	0.9808	28.2980	77.68	21.5599
0.001	0.9808	28.2980	77.68	21.5598
0.01	0.9808	28.2980	77.68	21.5598
0.1	0.9808	28.2974	77.68	21.5594
1	0.9808	28.2918	77.7	21.5606
2	0.9808	28.2848	77.71	21.5581
3	0.9808	28.2810	77.72	21.5580
4	0.9808	28.2741	77.73	21.5555
5	0.9808	28.2671	77.73	21.5502
10	0.9807	28.2399	77.76	21.5355
20	0.9806	28.1862	77.8	21.5034
30	0.9805	28.1377	77.83	21.4725
40	0.9804	28.0933	77.86	21.4447
50	0.9804	28.0548	77.88	21.4209
60	0.9803	28.0201	77.91	21.4004
70	0.9802	27.9886	77.93	21.3796
80	0.9801	27.9614	77.94	21.3594
90	0.9801	27.9379	77.96	21.3470
100	0.98	27.9190	78.2	21.3960

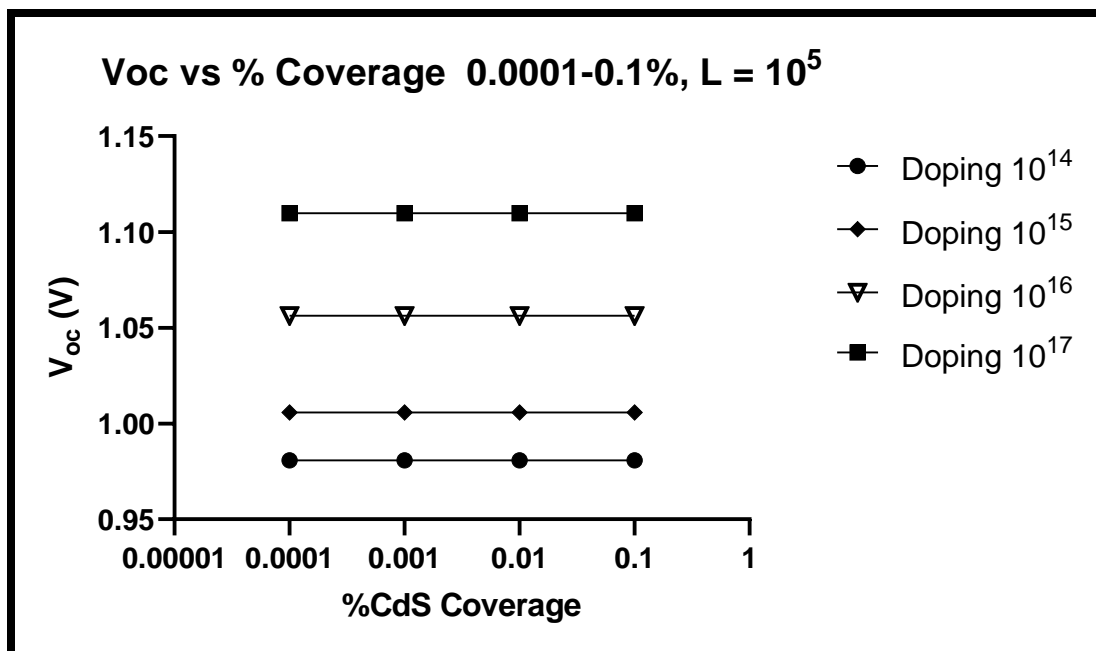


Figure A.25 Voc vs 0.0001-0.1% CdS Coverage Interpore Distance 100 μ m

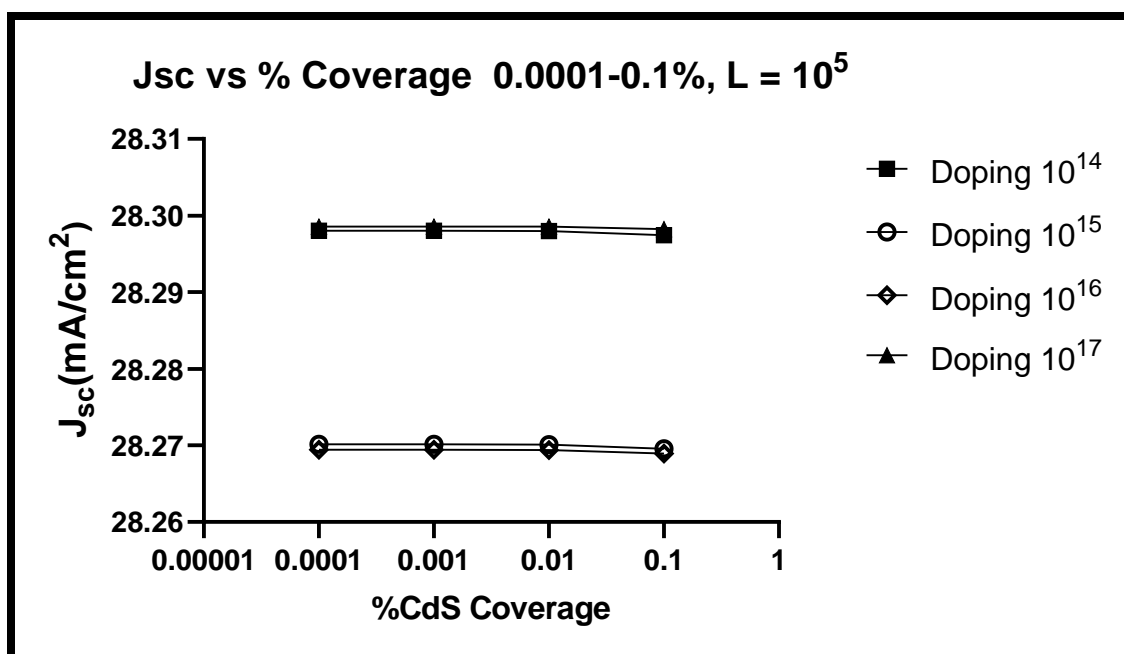


Figure A.26 Jsc vs 0.0001-0.1% CdS Coverage Interpore Distance 100 μ m

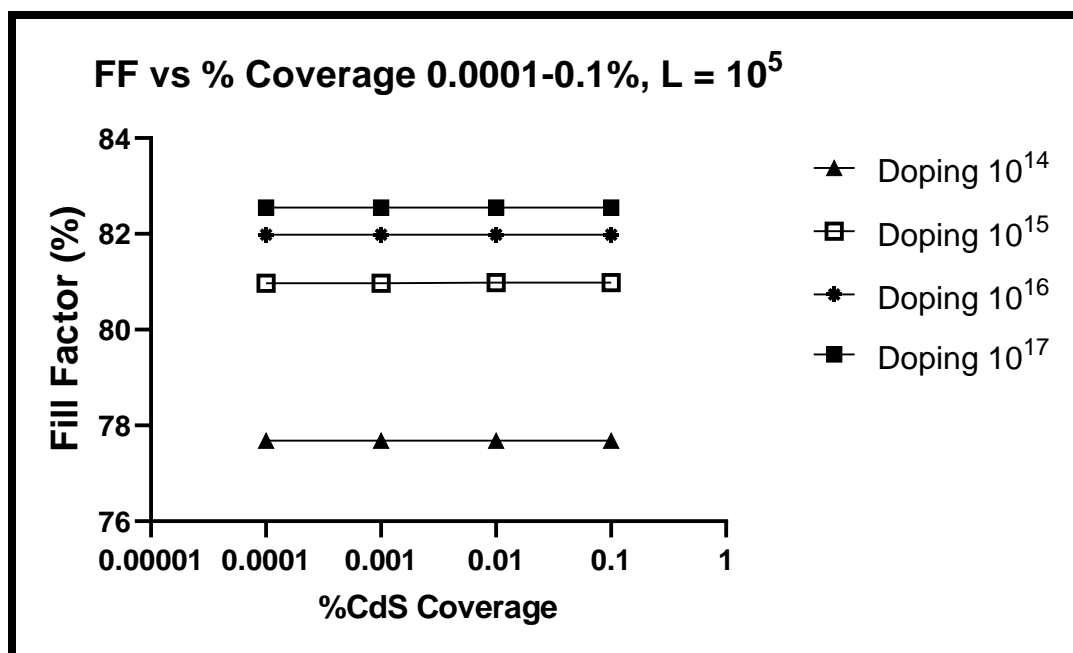


Figure A.27 FF vs 0.0001-0.1% CdS Coverage Interpore Distance 100 μ m

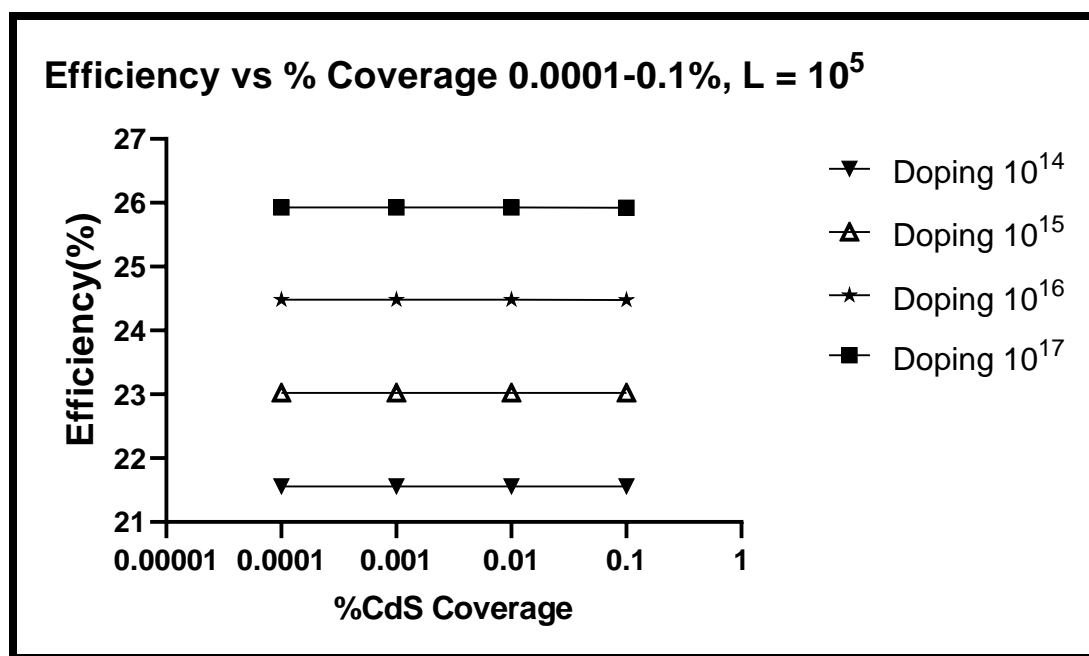


Figure A.28 Efficiency vs 0.0001-0.1% CdS Coverage Interpore Distance 100 μ m

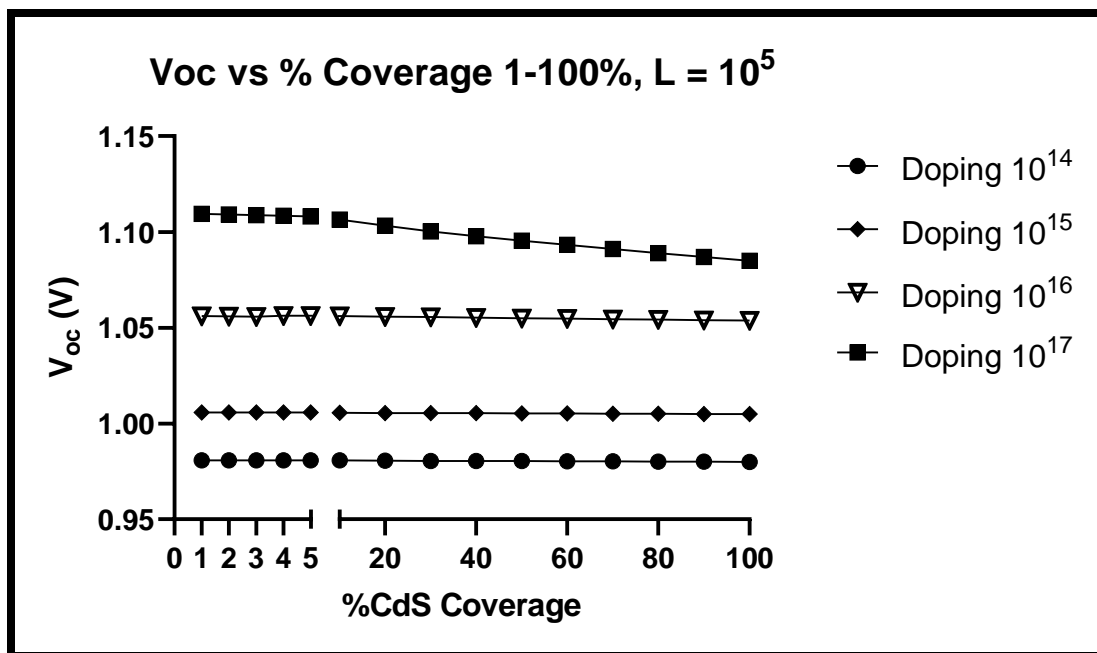


Figure A.29 Voc vs 1-100% CdS Coverage Interpore Distance 100 μ m

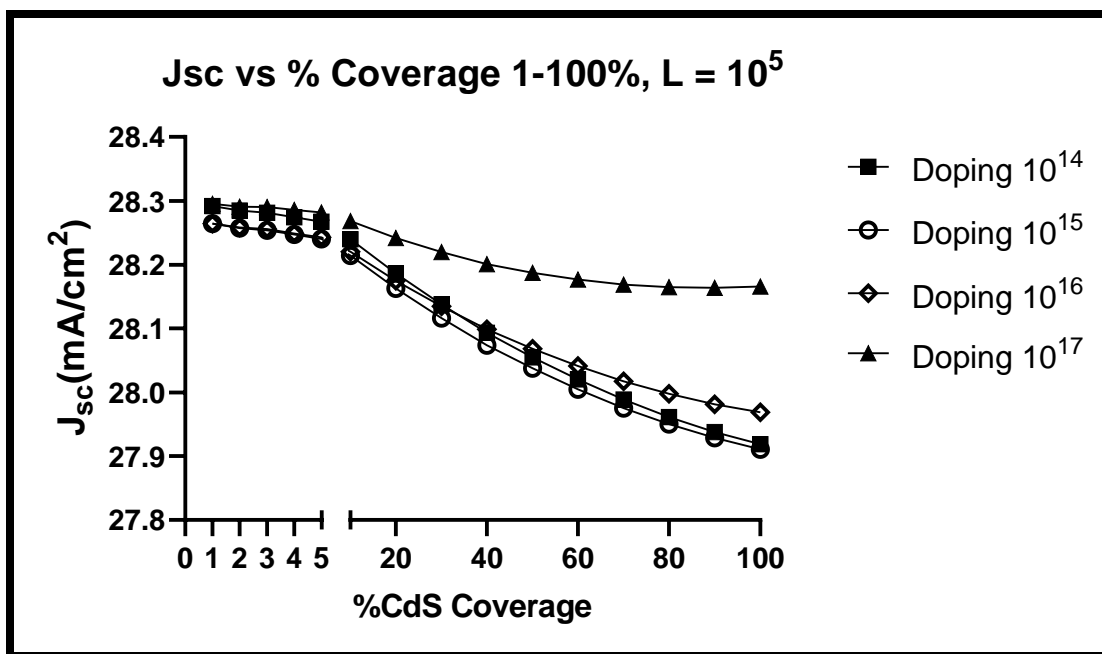


Figure A.30 Jsc vs 1-100% CdS Coverage Interpore Distance 100 μ m

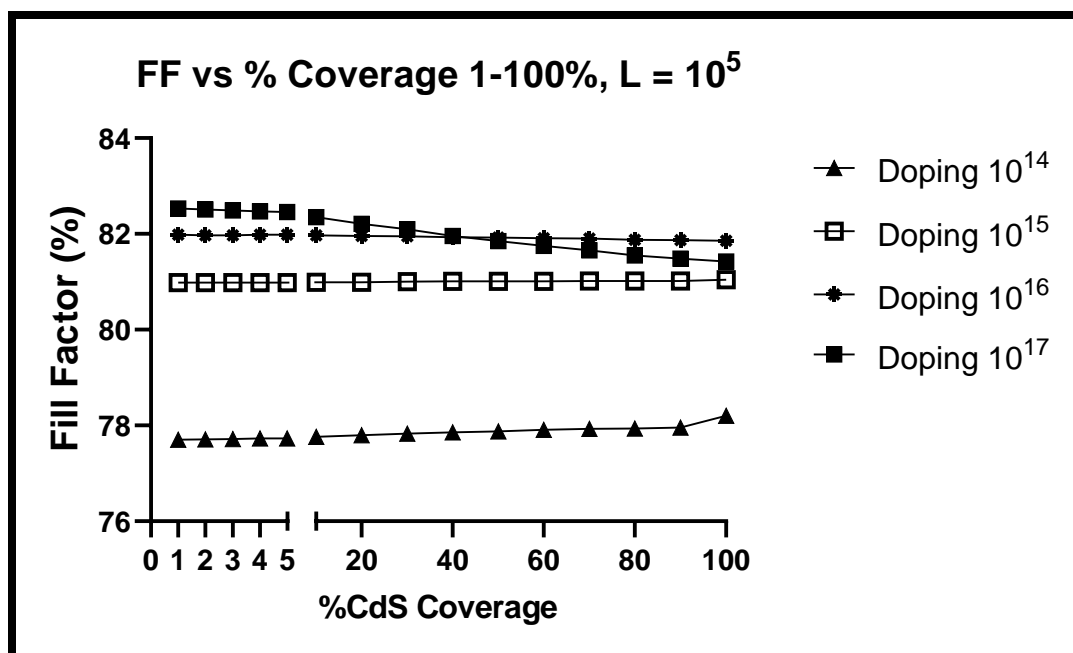


Figure A.31 FF vs 1-100% CdS Coverage Interpore Distance $100\mu\text{m}$

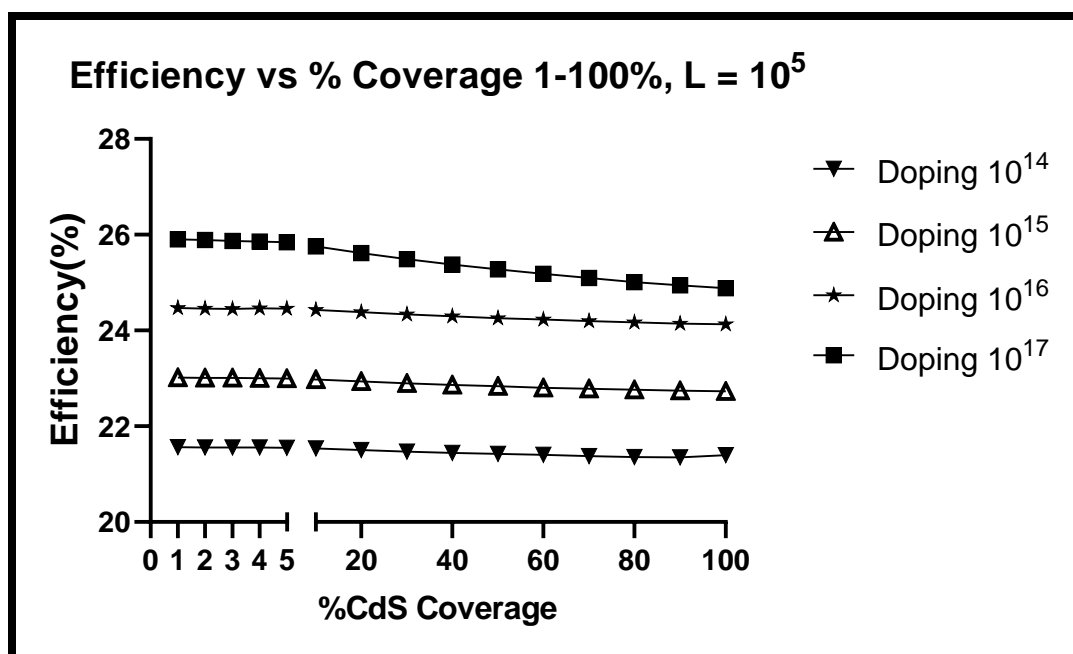


Figure A.32 Efficiency vs 1-100% CdS Coverage Interpore Distance $100\mu\text{m}$

Table A.17 Effect of CdS Coverage on Voc, Jsc, FF and Efficiency for 10¹⁷ CdTe**doping, Pitch = 10⁶ nm**

%CdS Coverage	Voc	Jsc	FF	Efficiency
0.0001	1.1098	28.2984	82.51	25.9127
0.001	1.1098	28.2984	82.51	25.9127
0.01	1.1098	28.2984	82.51	25.9127
0.1	1.1097	28.2981	82.51	25.9101
1	1.1094	28.2949	82.5	25.8971
2	1.1091	28.2906	82.48	25.8798
3	1.1087	28.2899	82.46	25.8636
4	1.1084	28.2857	82.44	25.8465
5	1.1081	28.2814	82.43	25.8324
10	1.1064	28.2682	82.32	25.7463
20	1.1032	28.2416	82.18	25.6041
30	1.1002	28.2195	82.07	25.4803
40	1.0978	28.2008	81.94	25.3676
50	1.0955	28.1871	81.83	25.2683
60	1.0933	28.1766	81.72	25.1743
70	1.0911	28.1688	81.64	25.0920
80	1.089	28.1646	81.53	25.0063
90	1.087	28.1636	81.46	24.9380
100	1.085	28.1657	81.42	24.8818

Table A.18 Effect of CdS Coverage on Voc, Jsc, FF and Efficiency for 10¹⁶ CdTe**doping, Pitch = 10⁶ nm**

%CdS Coverage	Voc	Jsc	FF	Efficiency
0.0001	1.0563	28.2693	81.95	24.4710
0.001	1.0563	28.2693	81.95	24.4710
0.01	1.0563	28.2692	81.95	24.4709
0.1	1.0563	28.2688	81.95	24.4705
1	1.0561	28.2641	81.94	24.4589
2	1.0559	28.2582	81.94	24.4492
3	1.0557	28.2557	81.94	24.4424
4	1.0562	28.2488	81.94	24.4480
5	1.0562	28.2427	81.94	24.4426
10	1.0561	28.2199	81.94	24.4206
20	1.0558	28.1748	81.93	24.3717
30	1.0555	28.1347	81.92	24.3271
40	1.0553	28.0986	81.91	24.2883
50	1.055	28.0681	81.9	24.2521
60	1.0548	28.0411	81.89	24.2212
70	1.0545	28.0173	81.88	24.1908
80	1.0543	27.9975	81.86	24.1633
90	1.054	27.9813	81.85	24.1395
100	1.0538	27.9688	81.86	24.1270

**Table A.19 Effect of CdS Coverage on Voc, Jsc, FF and Efficiency for 10¹⁵ CdTe
doping, Pitch = 10⁶ nm**

%CdS Coverage	Voc	Jsc	FF	Efficiency
0.0001	1.0058	28.2687	80.6	22.9167
0.001	1.0058	28.2686	80.6	22.9167
0.01	1.0058	28.2686	80.6	22.9166
0.1	1.0058	28.2681	80.6	22.9162
1	1.0057	28.2626	80.62	22.9152
2	1.0057	28.2559	80.63	22.9126
3	1.0057	28.2524	80.64	22.9126
4	1.0057	28.2457	80.64	22.9072
5	1.0057	28.2389	80.65	22.9045
10	1.0057	28.2129	80.67	22.8890
20	1.0056	28.1614	80.71	22.8563
30	1.0055	28.1152	80.73	22.8222
40	1.0054	28.0730	80.76	22.7942
50	1.0053	28.0366	80.77	22.7652
60	1.0052	28.0039	80.79	22.7420
70	1.0052	27.9745	80.81	22.7237
80	1.0051	27.9492	80.82	22.7038
90	1.005	27.9277	80.83	22.6869
100	1.005	27.9107	81.04	22.7319

Table A.20 Effect of CdS Coverage on Voc, Jsc, FF and Efficiency for 10¹⁴ CdTe**doping, Pitch = 10⁶ nm**

%CdS Coverage	Voc	Jsc	FF	Efficiency
0.0001	0.9809	28.2836	73.88	20.4968
0.001	0.9809	28.2836	73.88	20.4968
0.01	0.9809	28.2836	73.9	20.5023
0.1	0.9809	28.2832	73.95	20.5159
1	0.9808	28.2781	74.1	20.5517
2	0.9808	28.2714	74.2	20.5746
3	0.9808	28.2679	74.27	20.5915
4	0.9808	28.2612	74.33	20.6032
5	0.9808	28.2544	74.39	20.6149
10	0.9807	28.2278	74.6	20.6515
20	0.9806	28.1751	74.9	20.6938
30	0.9805	28.1274	75.14	20.7228
40	0.9804	28.0837	75.34	20.7436
50	0.9804	28.0458	75.51	20.7623
60	0.9803	28.0115	75.67	20.7788
70	0.9802	27.9805	75.82	20.7948
80	0.9801	27.9537	75.95	20.8084
90	0.9801	27.9307	76.08	20.8268
100	0.98	27.9190	78.2	21.3960

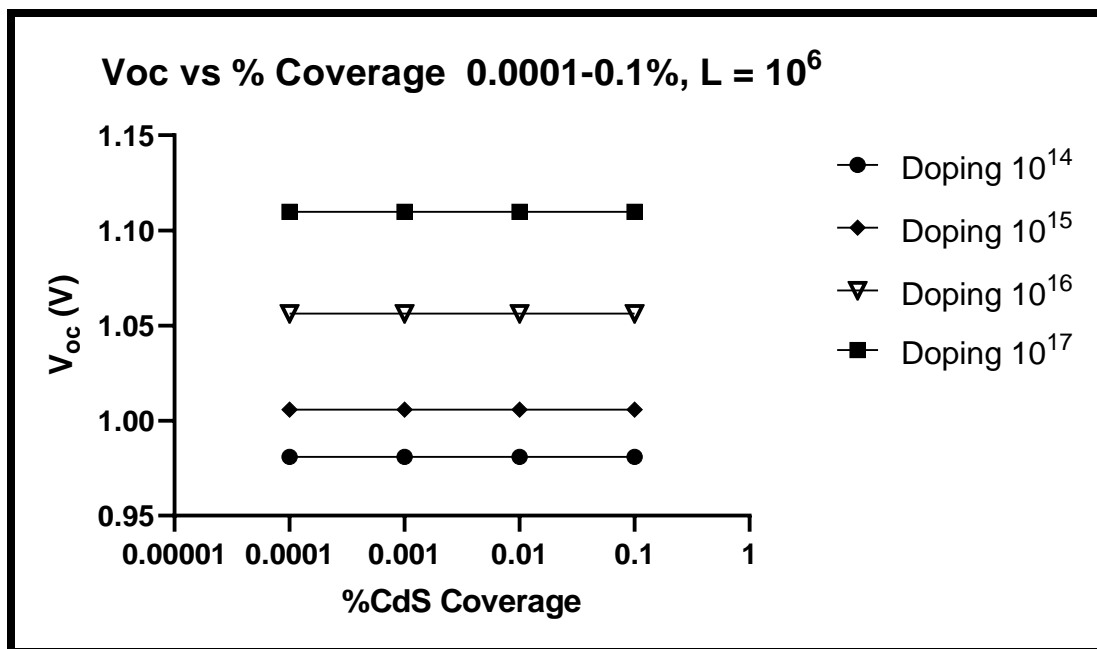


Figure A.33 Voc vs 0.0001-0.1% CdS Coverage Interpore Distance 1mm

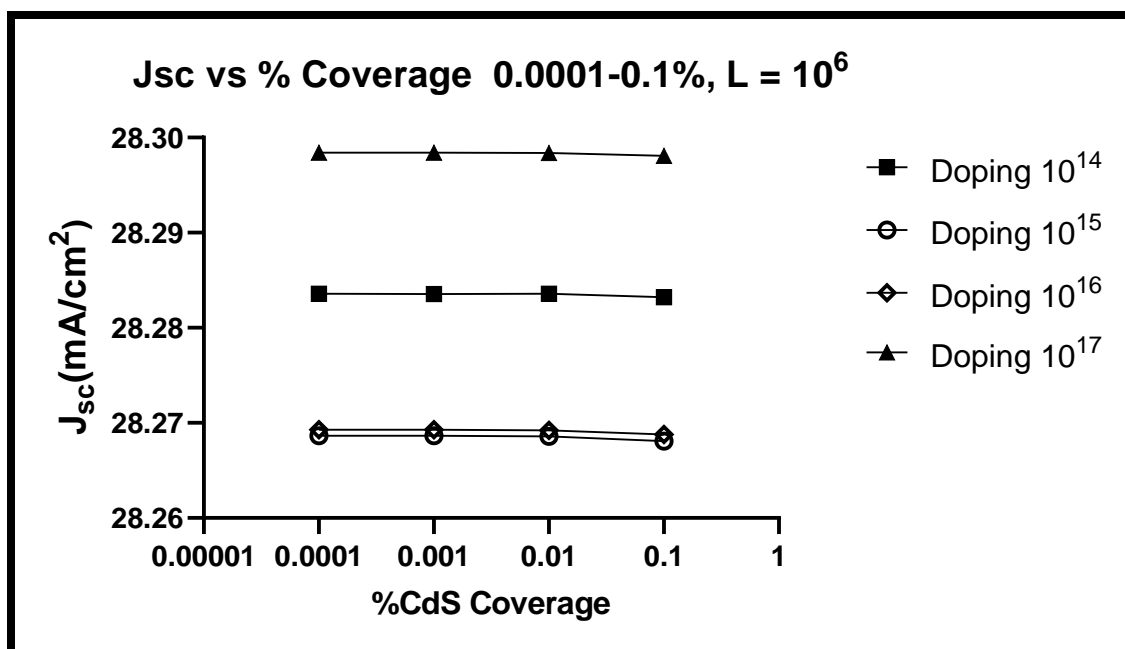


Figure A.34 Jsc vs 0.0001-0.1% CdS Coverage Interpore Distance 1mm

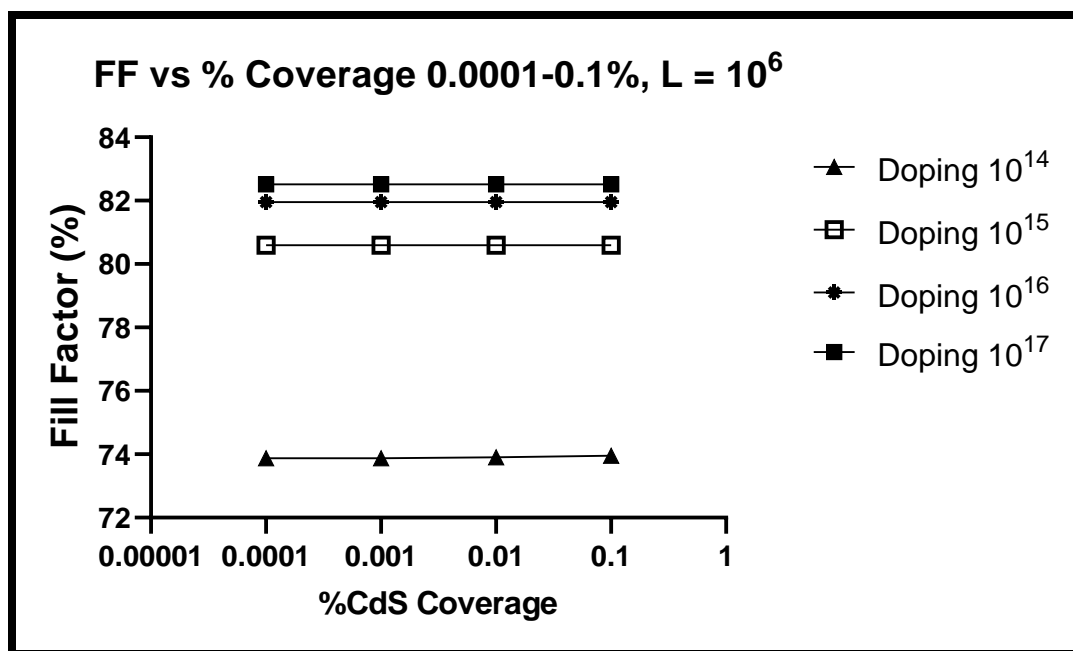


Figure A.35 FF vs 0.0001-0.1% CdS Coverage Interpore Distance 1mm

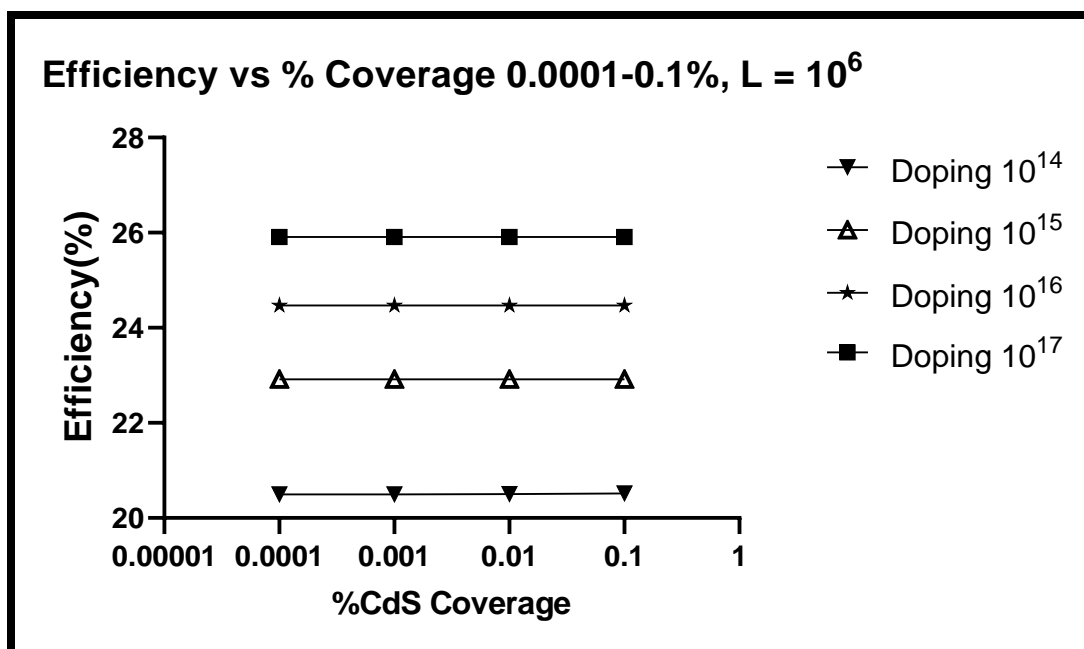


Figure A.36 Efficiency vs 0.0001-0.1% CdS Coverage Interpore Distance 1mm

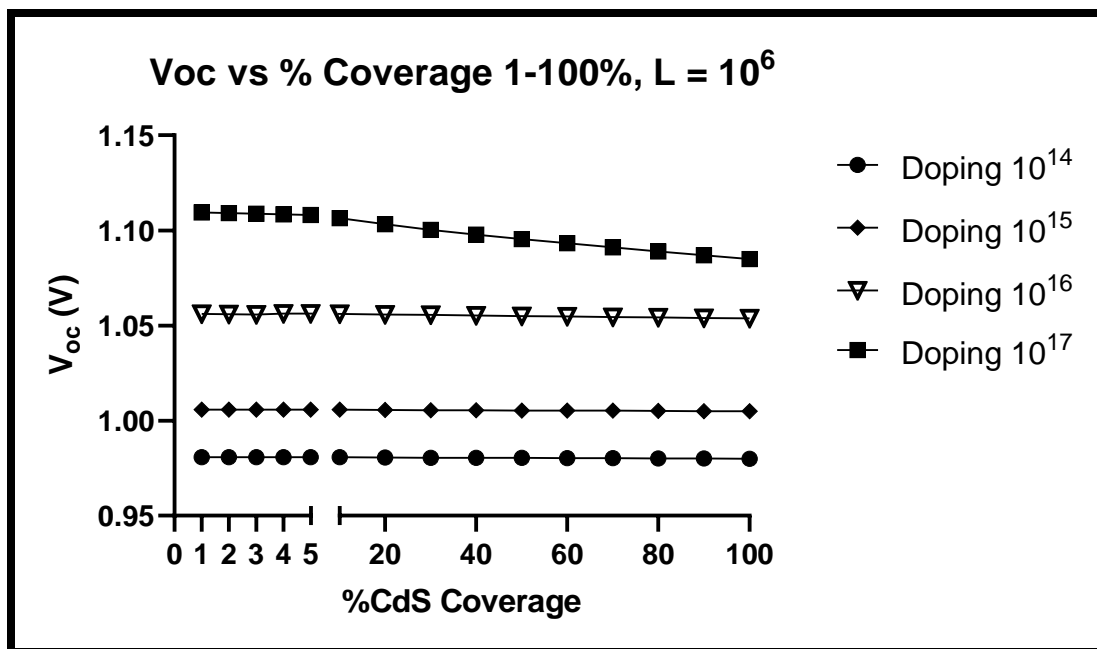


Figure A.37 Voc vs 1-100% CdS Coverage Interpore Distance 1mm

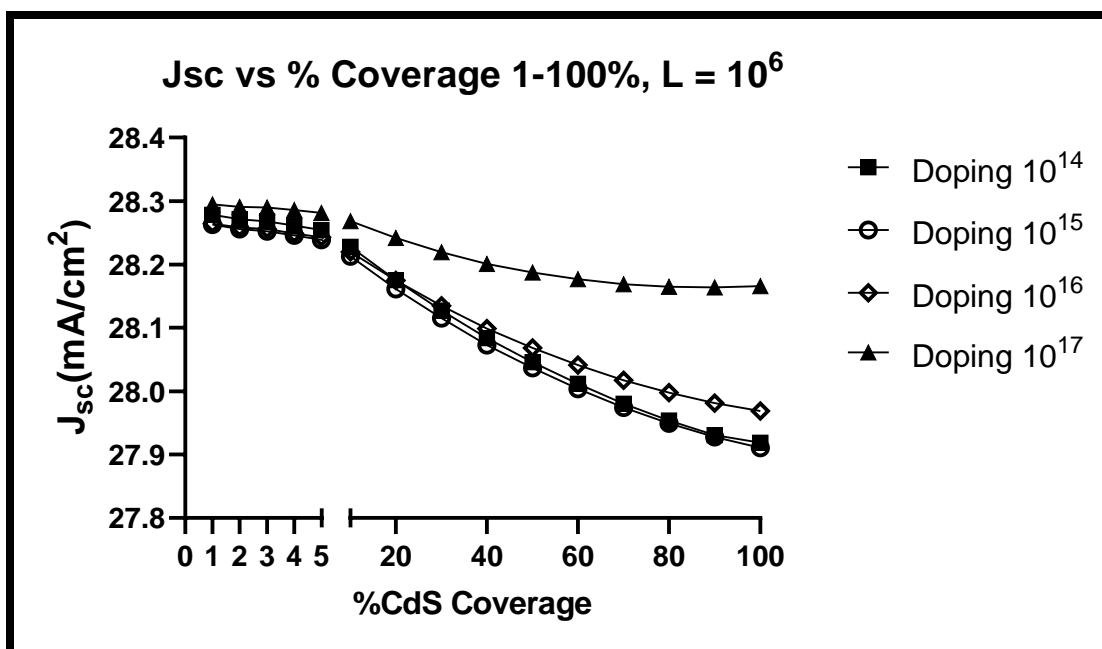


Figure A.38 Jsc vs 1-100% CdS Coverage Interpore Distance 1mm

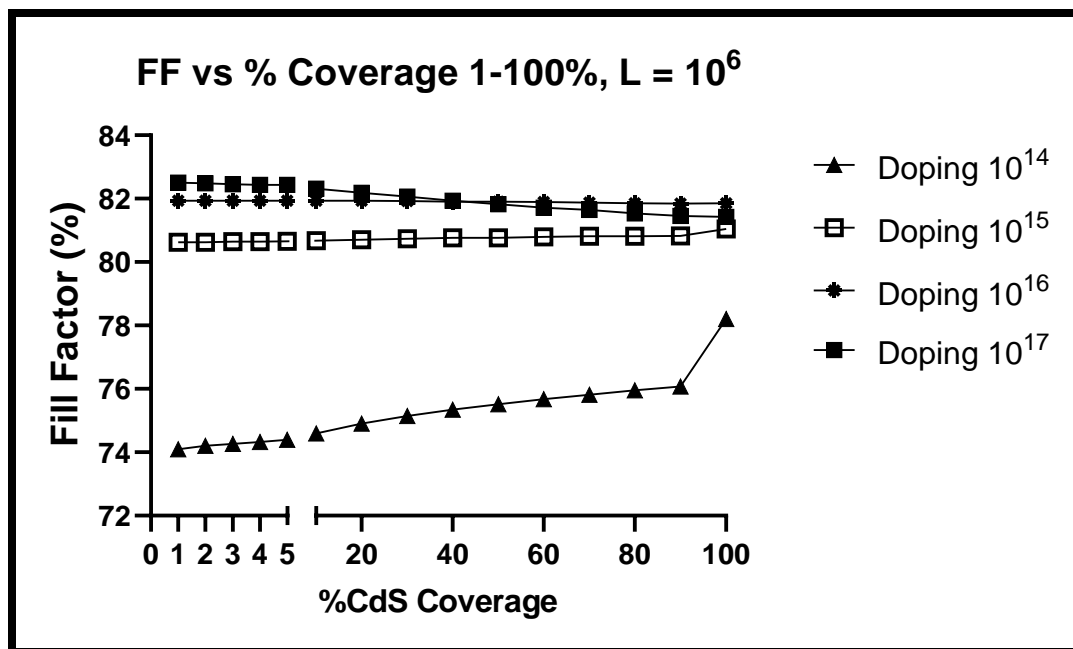


Figure A.39 FF vs 1-100% CdS Coverage Interpore Distance 1mm

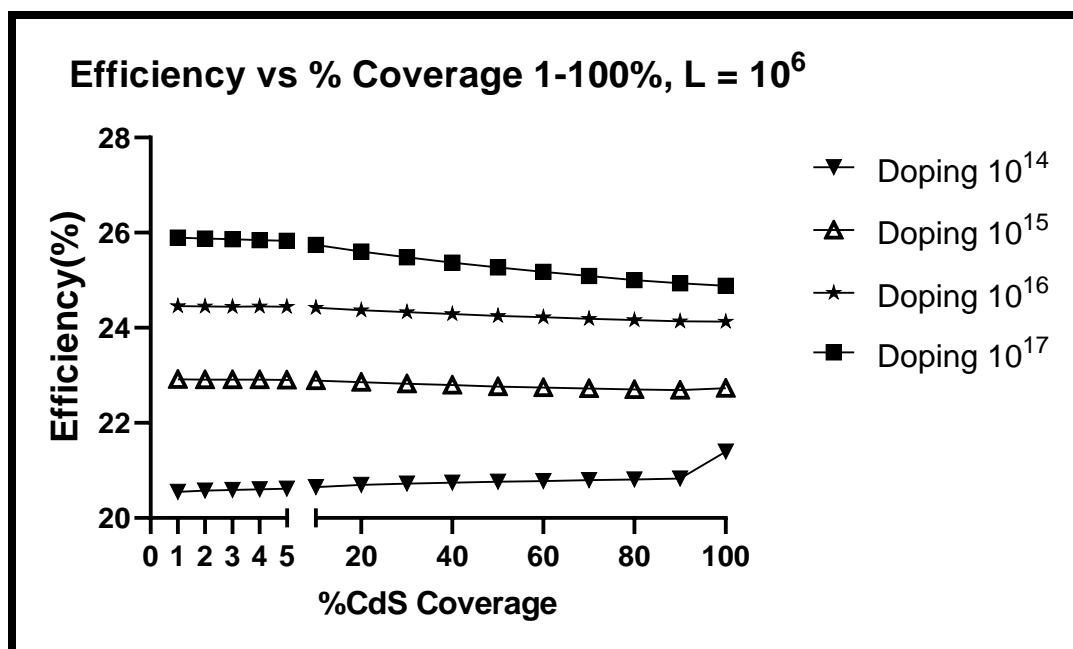


Figure A.40 Efficiency vs 1-100% CdS Coverage Interpore Distance 1mm

Table A.21 Effect of CdS Coverage on Voc, Jsc, FF and Efficiency for 10¹⁷ CdTe**doping, Pitch = 10⁷ nm**

%CdS Coverage	Voc	Jsc	FF	Efficiency
0.0001	1.1098	28.2966	82.17	25.8043
0.001	1.1098	28.2966	82.17	25.8043
0.01	1.1098	28.2966	82.17	25.8043
0.1	1.1098	28.2963	82.18	25.8072
1	1.1095	28.2932	82.17	25.7943
2	1.1091	28.2889	82.16	25.7779
3	1.1088	28.2883	82.15	25.7672
4	1.1084	28.2841	82.14	25.7509
5	1.1081	28.2798	82.13	25.7369
10	1.1064	28.2666	82.03	25.6542
20	1.1032	28.2401	81.92	25.5218
30	1.1002	28.2181	81.83	25.4046
40	1.0978	28.1994	81.71	25.2952
50	1.0955	28.1859	81.61	25.1992
60	1.0933	28.1754	81.52	25.1116
70	1.0912	28.1676	81.45	25.0349
80	1.0891	28.1635	81.35	24.9524
90	1.087	28.1625	81.29	24.8850
100	1.085	28.1657	81.42	24.8818

Table A.22 Effect of CdS Coverage on Voc, Jsc, FF and Efficiency for 10¹⁶ CdTe**doping, Pitch = 10⁷ nm**

%CdS Coverage	Voc	Jsc	FF	Efficiency
0.0001	1.0564	28.2677	81.59	24.3644
0.001	1.0564	28.2677	81.59	24.3644
0.01	1.0564	28.2676	81.59	24.3643
0.1	1.0563	28.2672	81.59	24.3617
1	1.0561	28.2626	81.6	24.3561
2	1.0559	28.2567	81.61	24.3494
3	1.0557	28.2543	81.61	24.3427
4	1.0562	28.2474	81.62	24.3512
5	1.0562	28.2412	81.63	24.3489
10	1.0561	28.2185	81.64	24.3300
20	1.0558	28.1735	81.66	24.2903
30	1.0556	28.1336	81.67	24.2542
40	1.0553	28.0975	81.67	24.2162
50	1.0551	28.0670	81.67	24.1853
60	1.0548	28.0401	81.68	24.1583
70	1.0545	28.0163	81.68	24.1309
80	1.0543	27.9966	81.68	24.1093
90	1.0541	27.9805	81.68	24.0909
100	1.0538	27.9688	81.86	24.1270

Table A.23 Effect of CdS Coverage on Voc, Jsc, FF and Efficiency for 10¹⁵ CdTe**doping, Pitch = 10⁷ nm**

%CdS Coverage	Voc	Jsc	FF	Efficiency
0.0001	1.0059	28.2536	76.91	21.8581
0.001	1.0059	28.2536	76.92	21.8609
0.01	1.0059	28.2536	76.93	21.8638
0.1	1.0059	28.2533	76.98	21.8777
1	1.0058	28.2484	77.13	21.9143
2	1.0058	28.2419	77.22	21.9349
3	1.0058	28.2387	77.29	21.9523
4	1.0058	28.2322	77.35	21.9643
5	1.0058	28.2256	77.4	21.9733
10	1.0057	28.2003	77.61	22.0110
20	1.0056	28.1499	77.84	22.0346
30	1.0055	28.1044	78.07	22.0618
40	1.0055	28.0629	78.26	22.0828
50	1.0054	28.0271	78.43	22.1003
60	1.0053	27.9949	78.58	22.1150
70	1.0052	27.9659	78.72	22.1292
80	1.0051	27.9411	78.85	22.1440
90	1.0051	27.9201	78.97	22.1609
100	1.005	27.9107	81.04	22.7319

Table A.24 Effect of CdS Coverage on Voc, Jsc, FF and Efficiency for 10¹⁴ CdTe**doping, Pitch = 10⁷ nm**

%CdS Coverage	Voc	Jsc	FF	Efficiency
0.0001	0.9809	28.1345	40.95	11.3010
0.001	0.9809	28.1347	40.99	11.3121
0.01	0.9809	28.1353	41.09	11.3400
0.1	0.9809	28.1367	41.42	11.4316
1	0.9809	28.1372	42.49	11.7272
2	0.9808	28.1340	43.15	11.9067
3	0.9808	28.1331	43.66	12.0471
4	0.9808	28.1286	44.1	12.1666
5	0.9808	28.1238	44.49	12.2720
10	0.9808	28.1048	45.68	12.5918
20	0.9806	28.0627	48.14	13.2473
30	0.9805	28.0231	50.07	13.7576
40	0.9805	27.9861	51.71	14.1894
50	0.9804	27.9541	53.18	14.5746
60	0.9803	27.9251	54.26	14.8537
70	0.9802	27.8989	55.55	15.1910
80	0.9802	27.8767	56.76	15.5095
90	0.9801	27.8578	57.89	15.8060
100	0.98	27.9190	78.2	21.3960

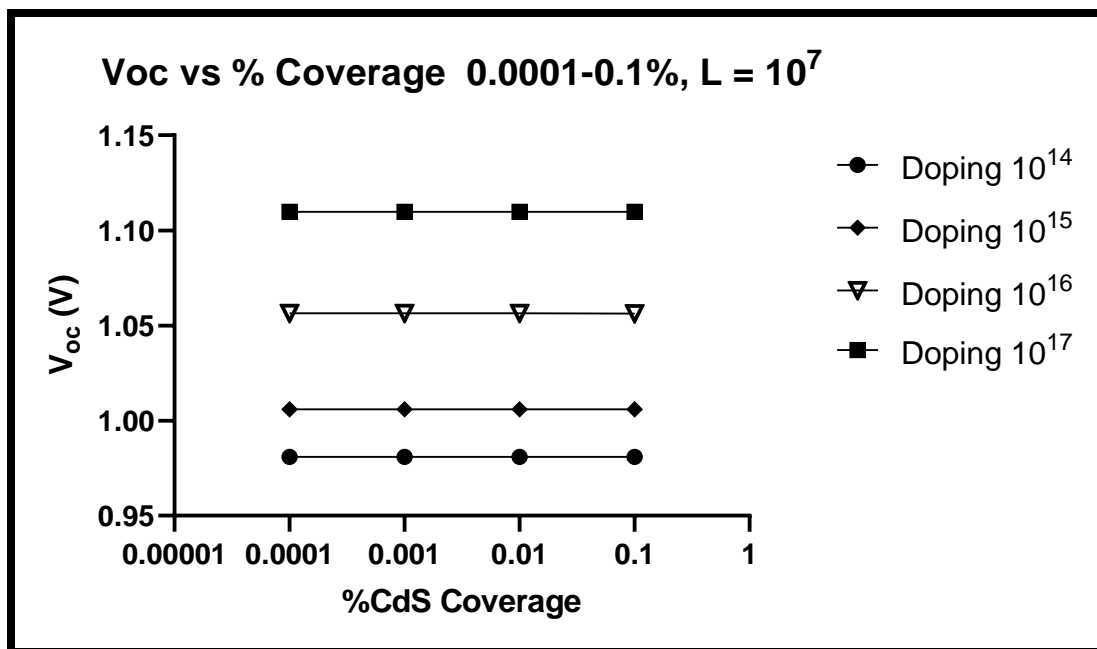


Figure A.41 Voc vs 0.0001-0.1% CdS Coverage Interpore Distance 10mm

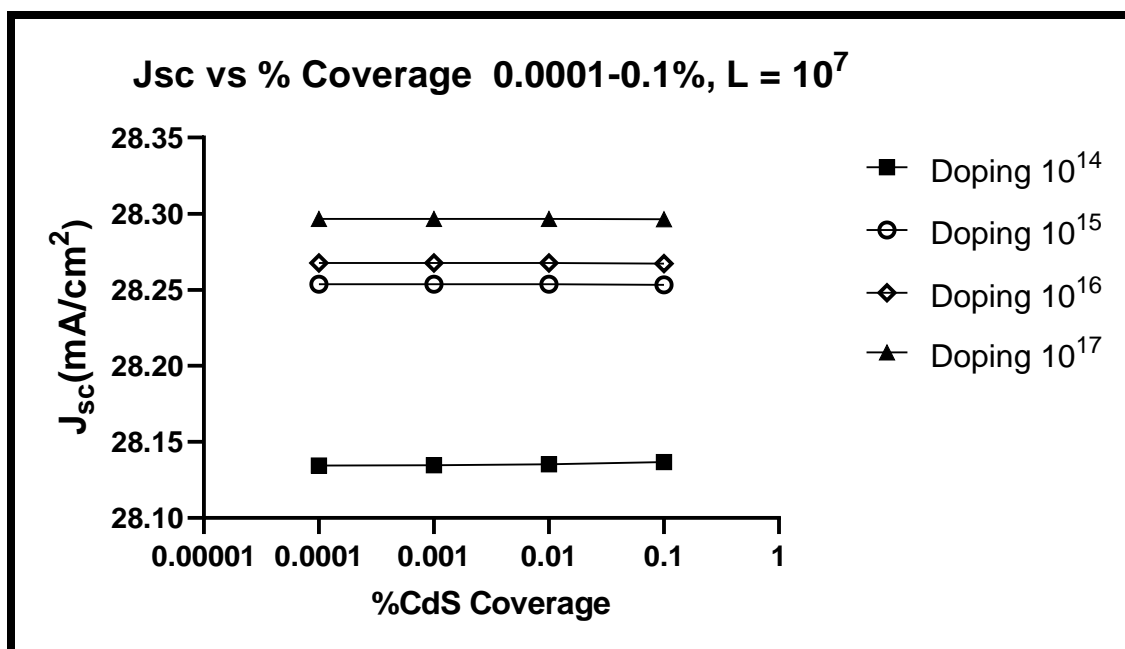


Figure A.42 Jsc vs 0.0001-0.1% CdS Coverage Interpore Distance 10mm

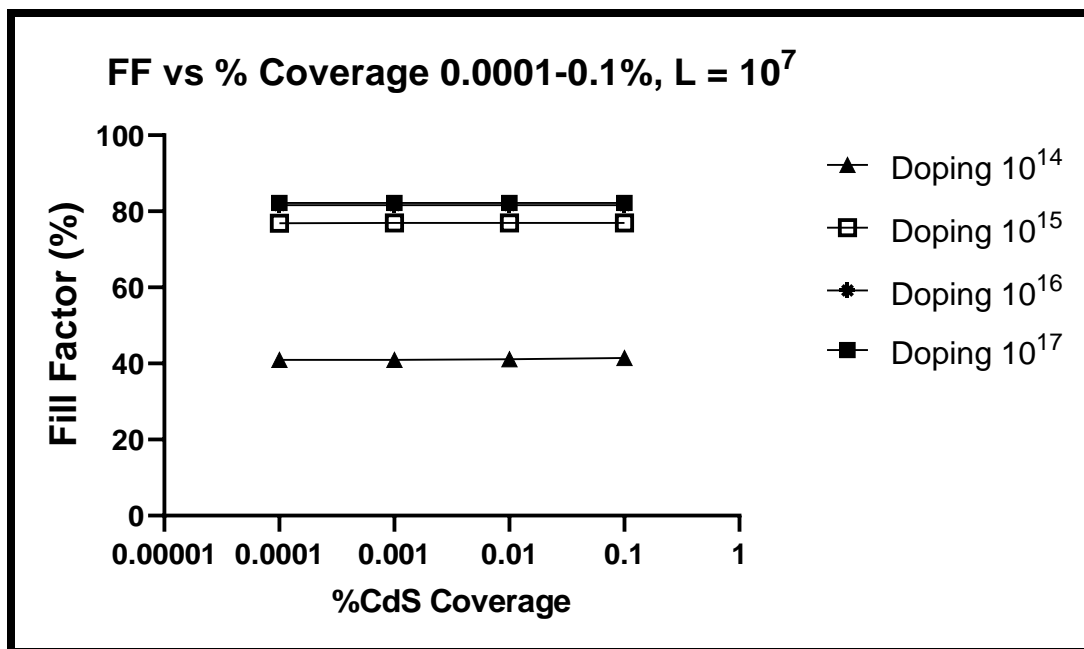


Figure A.43 FF vs 0.0001-0.1% CdS Coverage Interpore Distance 10mm

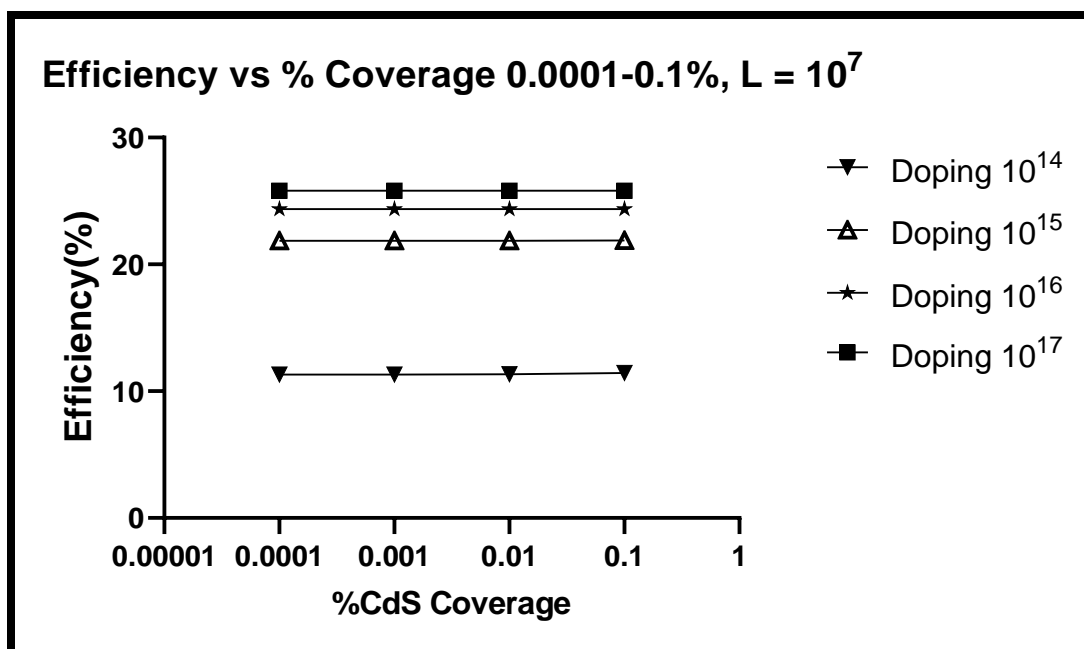


Figure A.44 Efficiency vs 0.0001-0.1% CdS Coverage Interpore Distance 10mm

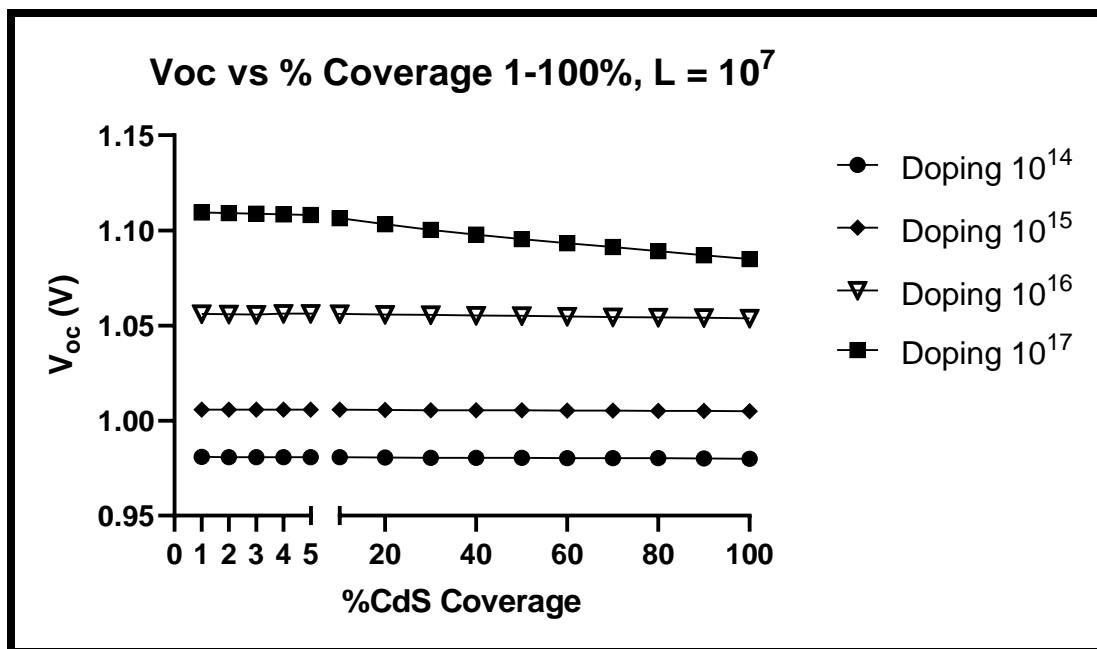


Figure A.45 Voc vs 1-100% CdS Coverage Interpore Distance 10mm

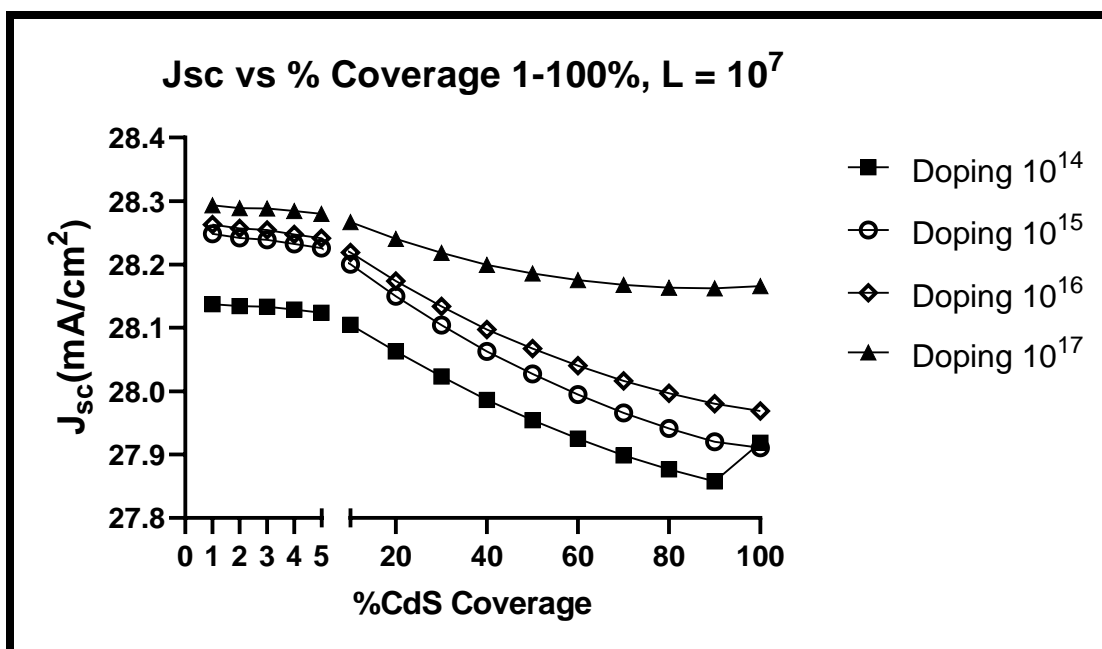


Figure A.46 Jsc vs 1-100% CdS Coverage Interpore Distance 10mm

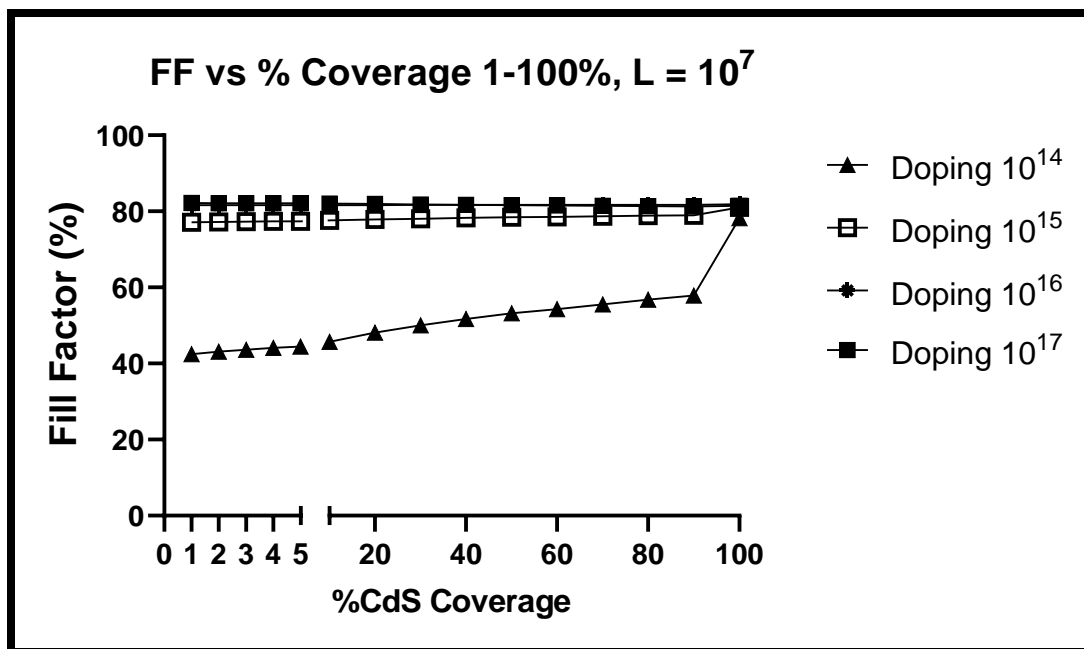


Figure A.47 FF vs 1-100% CdS Coverage Interpore Distance 10mm

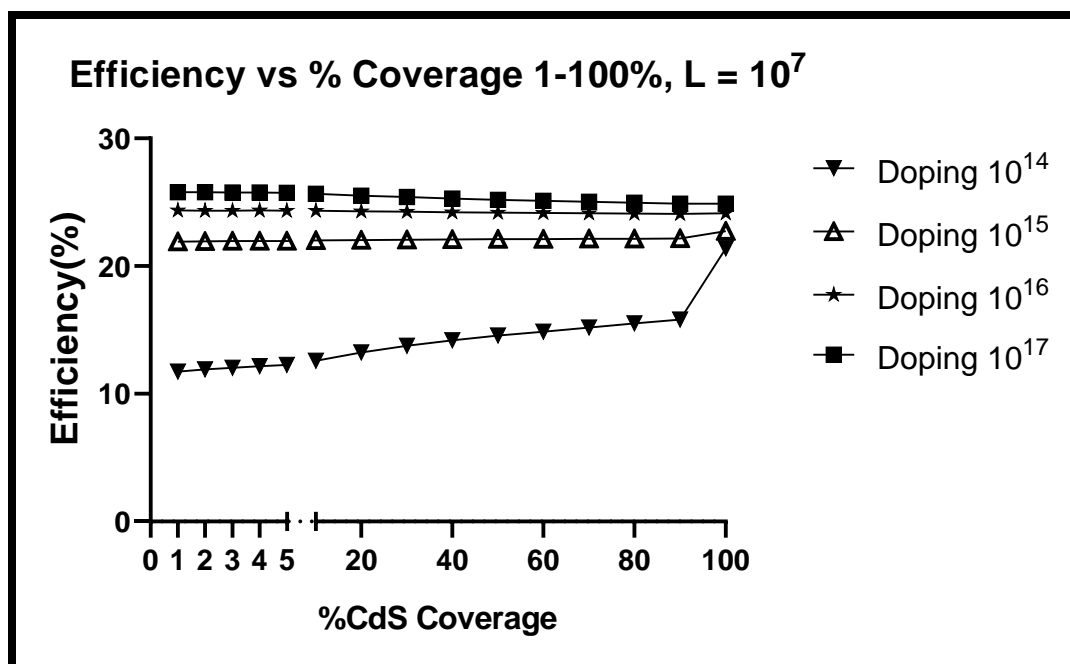


Figure A.48 Efficiency vs 1-100% CdS Coverage Interpore Distance 10mm

**Table A.25 Effect of CdS Coverage on Voc, Jsc, FF and Efficiency for 10¹⁷ CdTe
doping, Pitch = 10⁸ nm**

%CdS Coverage	Voc	Jsc	FF	Efficiency
0.0001	1.1101	28.2787	78.78	24.7308
0.001	1.1101	28.2787	78.79	24.7339
0.01	1.1101	28.2788	78.8	24.7371
0.1	1.1101	28.2787	78.84	24.7496
1	1.1097	28.2762	78.96	24.7761
2	1.1094	28.2722	79.02	24.7848
3	1.109	28.2718	79.07	24.7912
4	1.1087	28.2678	79.11	24.7935
5	1.1083	28.2637	79.14	24.7904
10	1.1066	28.2513	79.24	24.7727
20	1.1033	28.2256	79.33	24.7044
30	1.1002	28.2043	79.42	24.6443
40	1.0979	28.1862	79.45	24.5863
50	1.0957	28.1731	79.48	24.5349
60	1.0935	28.1631	79.51	24.4862
70	1.0913	28.1558	79.54	24.4398
80	1.0892	28.1520	79.54	24.3895
90	1.0871	28.1514	79.58	24.3542
100	1.085	28.1657	81.42	24.8818

Table A.26 Effect of CdS Coverage on Voc, Jsc, FF and Efficiency for 10¹⁶ CdTe**doping, Pitch = 10⁸ nm**

%CdS Coverage	Voc	Jsc	FF	Efficiency
0.0001	1.0566	28.2515	78.01	23.2864
0.001	1.0566	28.2515	78.02	23.2894
0.01	1.0566	28.2515	78.03	23.2924
0.1	1.0566	28.2513	78.07	23.3041
1	1.0564	28.2472	78.21	23.3381
2	1.0562	28.2417	78.3	23.3560
3	1.056	28.2395	78.36	23.3677
4	1.0565	28.2328	78.42	23.3911
5	1.0565	28.2269	78.47	23.4011
10	1.0563	28.2049	78.66	23.4350
20	1.056	28.1609	78.93	23.4721
30	1.0558	28.1217	79.13	23.4944
40	1.0555	28.0863	79.3	23.5085
50	1.0553	28.0564	79.44	23.5205
60	1.055	28.0300	79.57	23.5302
70	1.0547	28.0067	79.69	23.5393
80	1.0545	27.9874	79.8	23.5512
90	1.0542	27.9717	79.9	23.5607
100	1.0538	27.9688	81.86	24.1270

**Table A.27 Effect of CdS Coverage on Voc, Jsc, FF and Efficiency for 10¹⁵ CdTe
doping, Pitch = 10⁸ nm**

%CdS Coverage	Voc	Jsc	FF	Efficiency
0.0001	1.0061	28.1001	43.55	12.3122
0.001	1.0061	28.1003	43.59	12.3236
0.01	1.0061	28.1009	43.7	12.3550
0.1	1.0061	28.1023	44.05	12.4546
1	1.0061	28.1031	45.17	12.7716
2	1.006	28.1001	45.87	12.9668
3	1.006	28.0994	46.4	13.1164
4	1.006	28.0951	46.21	13.0607
5	1.006	28.0905	46.67	13.1885
10	1.0059	28.0727	48.45	13.6815
20	1.0058	28.0328	51.01	14.3825
30	1.0057	27.9953	53	14.9221
40	1.0057	27.9605	54.69	15.3788
50	1.0056	27.9306	56.19	15.7821
60	1.0055	27.9038	57.55	16.1469
70	1.0054	27.8797	58.53	16.4061
80	1.0053	27.8594	59.75	16.7342
90	1.0053	27.8426	60.89	17.0432
100	1.005	27.9107	81.04	22.7319

Table A.28 Effect of CdS Coverage on Voc, Jsc, FF and Efficiency for 10¹⁴ CdTe**doping, Pitch = 10⁸ nm**

%CdS Coverage	Voc	Jsc	FF	Efficiency
0.0001	0.9809	5.844030	28.26	1.6200
0.001	0.9809	5.850514	28.26	1.6218
0.01	0.9809	5.871115	28.26	1.6275
0.1	0.9809	5.937216	28.25	1.6452
1	0.9809	6.156327	28.23	1.7047
2	0.9808	6.297037	28.22	1.7429
3	0.9808	6.409457	28.21	1.7734
4	0.9808	6.507338	28.2	1.7998
5	0.9808	6.596065	28.19	1.8237
10	0.9808	6.968813	28.16	1.9247
20	0.9807	7.573626	28.08	2.0856
30	0.9806	8.113594	28	2.2277
40	0.9805	8.632146	27.91	2.3623
50	0.9804	9.146975	27.81	2.4939
60	0.9803	9.668021	27.7	2.6253
70	0.9802	10.202180	27.58	2.7580
0	0.9802	10.758009	19.31	2.0362
90	0.9801	11.337253	20.13	2.2368
100	0.9800	27.91899200	78.2	21.3960

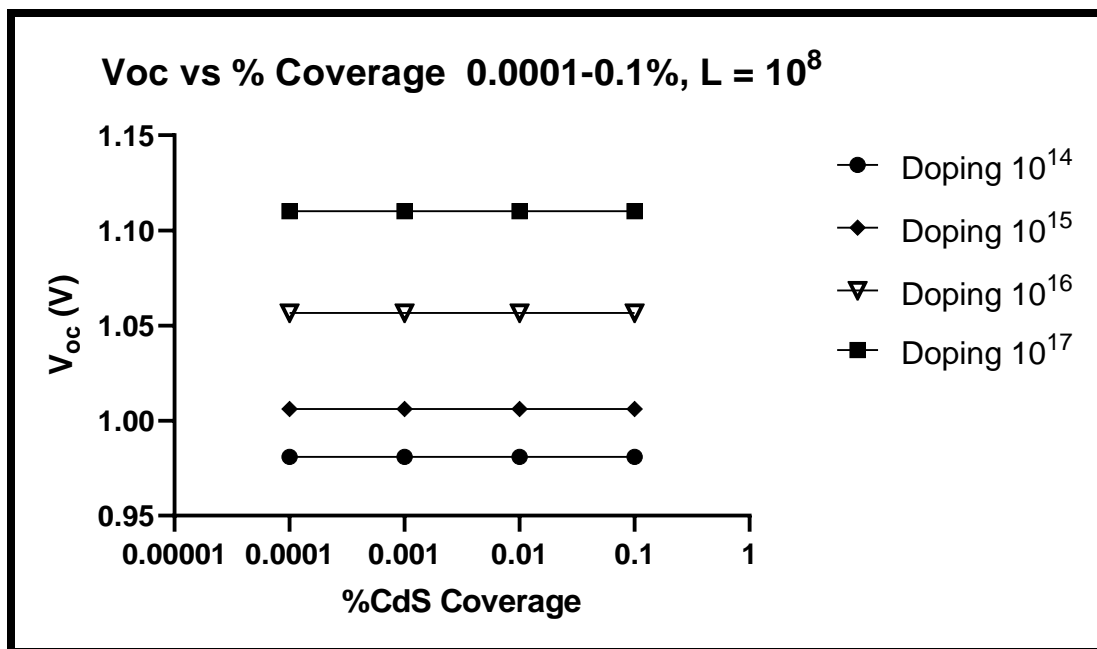


Figure A.49 Voc vs 0.0001-0.1% CdS Coverage Interpore Distance 100mm

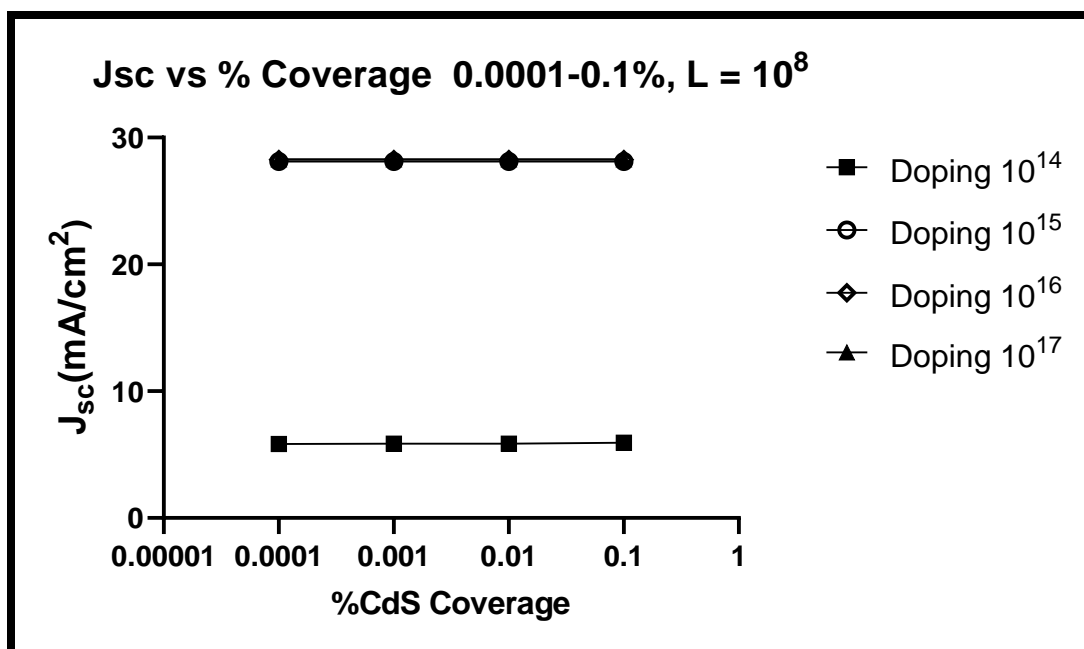


Figure A.50 Jsc vs 0.0001-0.1% CdS Coverage Interpore Distance 100mm

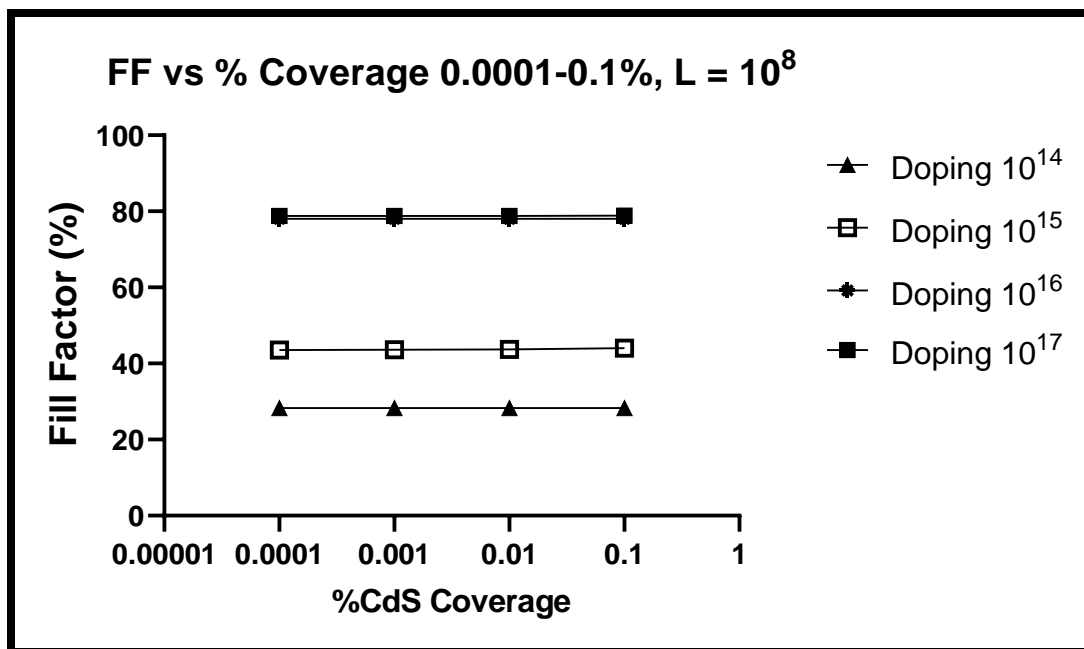


Figure A.51 FF vs 0.0001-0.1% CdS Coverage Interpore Distance 100mm

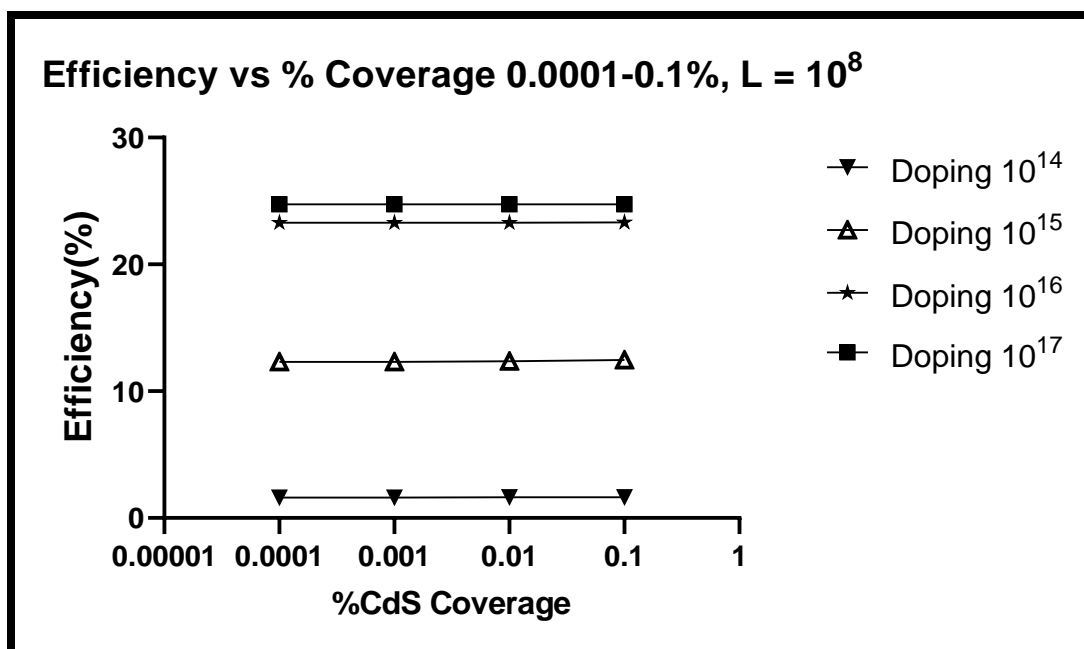


Figure A.52 Efficiency vs 0.0001-0.1% CdS Coverage Interpore Distance 100mm

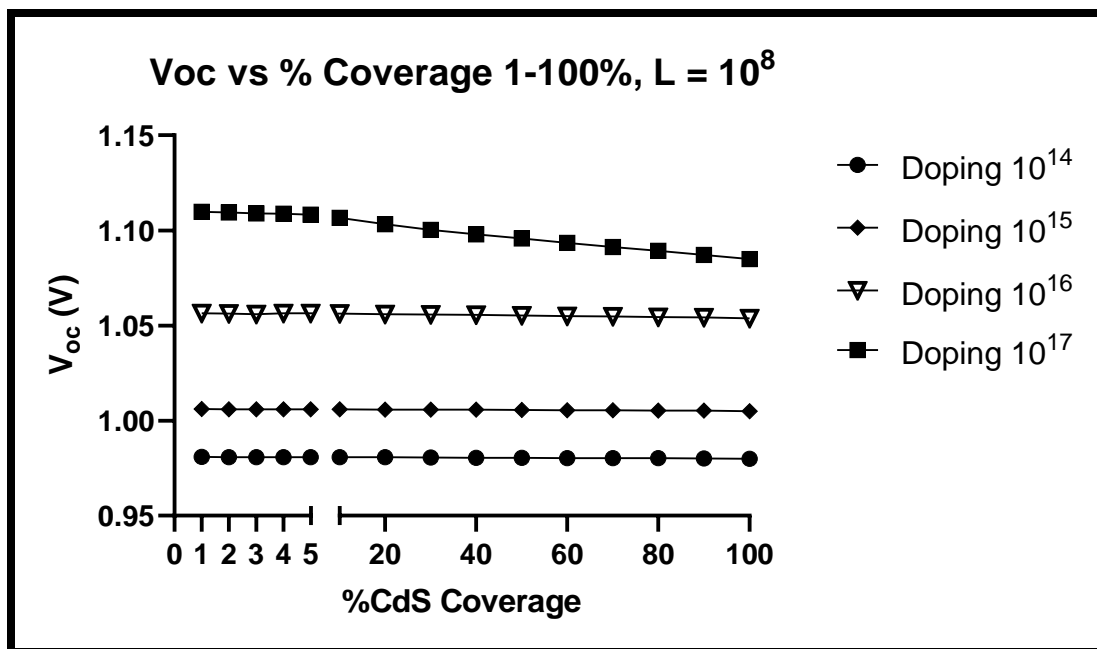


Figure A.53 Voc vs 1-100% CdS Coverage Interpore Distance 10mm

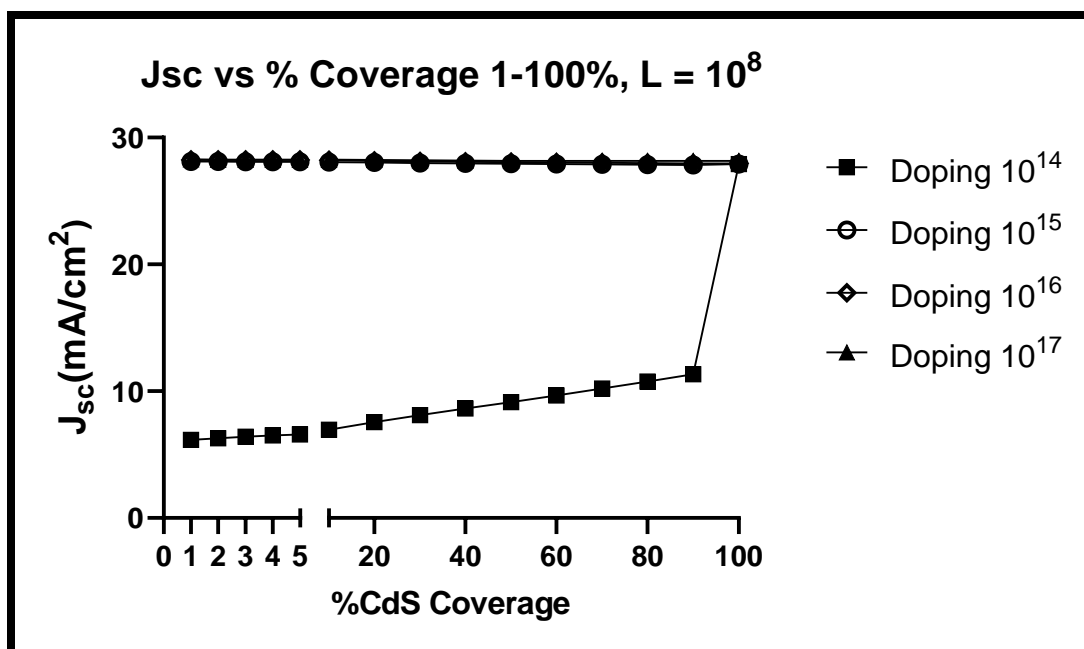


Figure A.54 Jsc vs 1-100% CdS Coverage Interpore Distance 10mm

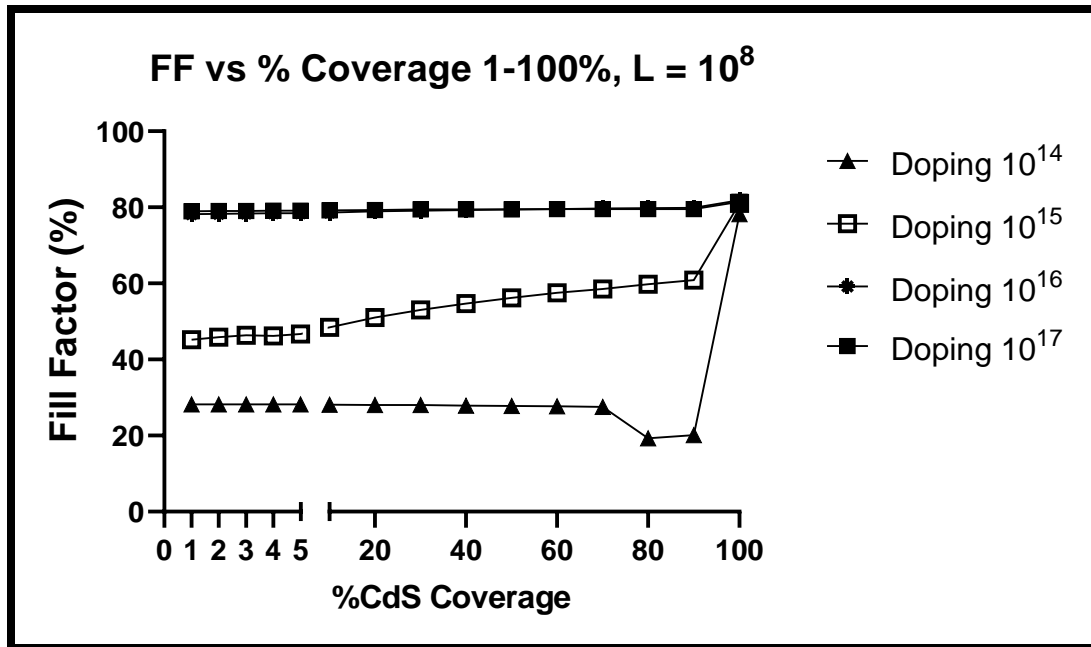


Figure A.55 FF vs 1-100% CdS Coverage Interpore Distance 100mm

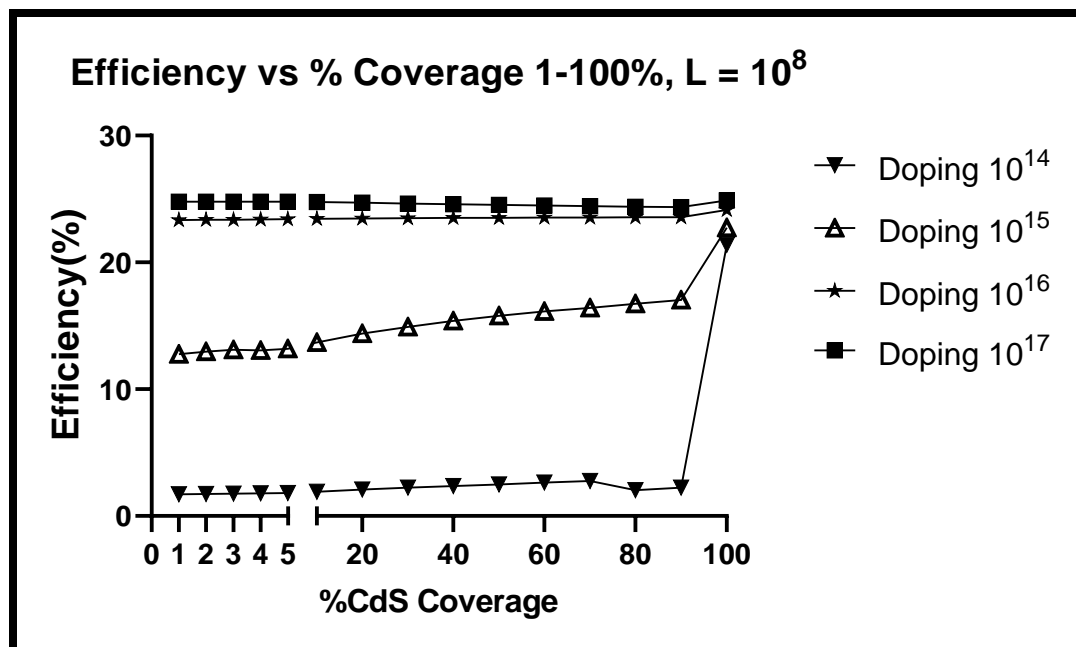


Figure A.56 Efficiency vs 1-100% CdS Coverage Interpore Distance 100mm

REFERENCES

- [1]. D. M. Chapin, C.S.F., and G. L. Pearson, A New Silicon p-n Junction Photocell for Converting Solar Radiation into Electrical Power. *J. Appl. Phys.*, 1954. 25: p. 676.
- [2]. D. C. Reynolds, G.L., L. L. Antes, and R. E. Marburger, Photovoltaic Effect in Cadmium Sulfide. *Phys. Rev.*, 1954. 96: p. 533.
- [3]. Climate Central. world-passes-400-ppm-threshold-permanently, 2016.
- [4]. Paul Denholm and Robert M Margolis. Land-use requirements and the per-capita solar footprint for photovoltaic generation in the united states. *Energy Policy*, 36(9):3531–3543, 2008.
- [5]. Shayle Kann. The state of solar, May 2016. GreenTech Media.
- [6]. Michael Woodhouse, Rebecca Jones-Albertus, David Feldman, Ran Fu, Kelsey Horowitz, Donald Chung, Dirk Jordan, and Sarah Kurtz. On the path to sunshot: The role of advancements in solar photovoltaic efficiency, reliability, and costs. Technical report, NREL (National Renewable Energy Laboratory), Golden, CO (United States), 2016.
- [7]. First Solar. First solar technology update, 2016.
- [8]. On the path to sunshot: The role of advancements in solar photovoltaic efficiency, reliability, and costs. Technical report, NREL (National Renewable Energy Laboratory), Golden, CO (United States), 2016.
- [9]. Antonio Luque and Steven Hegedus. Handbook of photovoltaic science and engineering. John Wiley & Sons, 2011.
- [10]. J Britt and C Ferekides. Thin-film CdS/CdTe solar cell with 15.8% efficiency. *Applied Physics Letters*, 62(22):2851–2852, 1993.

- [11]. First Solar. first solar global installation, 2015.
- [12]. Khagendra P Bhandari, Jennifer M Collier, Randy J Ellingson, and Defne S Apul. Energy payback time (epbt) and energy return on energy invested (eroi) of solar photovoltaic systems: A systematic review and meta-analysis. *Renewable and Sustainable Energy Reviews*, 47:133–141, 2015.
- [13]. J. J. Loferski, "Theoretical Considerations Governing the Choice of the Optimum Semiconductor for Photovoltaic Solar Energy Conversion," *Journal of Applied Physics*, vol. 27, no. 7, pp. 777-784, 1956.
- [14]. H. M. Dang, V. P. Singh, S. Guduru, and J. T. Hastings, “Embedded Nanowire Window Layers for Enhancing Quantum Efficiency in Window-Absorber type solar cells”, *Solar Energy Materials and Solar Cells*, 144 (2016) 641-651.
- [15]. J. M. Burst et al, “CdTe solar cells with open circuit voltage breaking the 1 V barrier”, *Nature Energy* 1, 16015 (2016), March 2016.
- [16]. K. Ernst, A. Belaidi, R. Konenkamp 18 (2003) 475-479.
- [17]. R. Konenkamp , L. Dloczik, K. Ernst and C. Olesch, *Physica E*, 14,(2002) 219-23.
- [18]. M. Green, *Solid-State Electron*.1981, 24, 788.
- [19]. S.M. Sze, K. K. N., “Physics of semiconductor devices” (2007).
- [20]. Tighineanu, A.; Ruff, T.; Albu, S.; Hahn, R.; Schmuki, P. Conductivity of TiO₂ nanotubes: Influence of annealing time and temperature. *Chem. Phys. Lett.* 2010, 494, 260–263.
- [21]. A.W. Czandema, C.N.R. Rao, J.M. Honig, *Trans. Faraday Soc.* 54 (1958) 1069.

- [22]. L. Forro, O. Chauvet, D. Emin, L. Zuppiroli, H. Berger, F. Levy, J. Appl. Phys. 75(1993) 633.
- [23] V. Zwillling, M. Aucouturier, E. Darque-Ceretti Anodic oxidation of titanium and TA6V alloy in chromic media. An electrochemical approach *Electrochim. Acta*, 45 (1999), pp. 921-929.
- [24] Zhao J, Wang X, Chen R et al (2005) Fabrication of Titanium oxide nanotubes arrays by anodic oxidation. *Solid State Commun* 134: 705-710.
- [25] O'Sullivan, J. P; Wood G. C. *Proc. R. Soc. London, ser. A* 1970, 317, 511.
- [26] Roy P, Berger S, Schmuki P (2011) TiO₂ nanotubes: synthesis and applications. *Angew Chem Int Ed* 50(13):2904-2939.
- [27] Macak JM, Tsuchiya H, Ghicov A et al (2007) TiO₂ nanotubes: self-organized electrochemical formation, properties and applications. *Curr Opinion Solid State Matter Sci* 11 (1-2): 3-18.
- [28]. Gong D, Grimes CA, Varghese OK et al (2001) Titanium oxide nanotube arrays prepared by anodic oxidation. *J Mater Res* 16(12):3331–3334.
- [29]. Mor GK, Varghese OK, Paulose M et al (2003) Fabrication of tapered, conical shaped titania nanotubes. *J Mater Res* 18(11):2588–2593.
- [30]. Varghese OK, Gong D, Paulose M et al (2003) Extreme changes in the electrical resistance of titania nanotubes with hydrogen exposure. *Adv Mater* 15(7–8):624–627.

- [31]. Cai Q, Paulose M, Varghese OK et al (2005) The effect of electrolyte composition on the fabrication of self-organized titanium oxide nanotube arrays by anodic oxidation. *J Mater Res* 20(1):230–236.
- [32]. Paulose M, Prakasam HE, Varghese OK et al (2007) TiO₂ nanotube arrays of 1000 μm length by anodization of titanium foil: phenol red diffusion. *J Phys Chem C* 111(41):14992–14997.
- [33]. Albu SP, Ghicov A, Aldabergenova S et al (2008) Formation of double walled TiO₂ nanotubes and robust Anatase membranes. *Adv Mater* 20(21): 4135–4139.
- [34]. N. K. Allam and C. A. Grimes, *J. Phys. Chem. C*, 2007, 111, 13028–13032.
- [35]. N. K. Allam, K. Shankar and C. A. Grimes, *J. Mater. Chem.*, 2008, 18, 2341–2346.
- [36]. X. Chen, M. Schriver, T. Suen and S. S. Mao, *Thin Solid Films*, 2007, 515, 8511–8514.
- [37]. J. P. Frayret, R. Pointeau and A. Caprani, *Electrochim. Acta*, 1981, 26, 1783–1788.
- [38]. Paulose M, Shankar K, Yoriya S et al (2006) Anodic growth of highly ordered TiO₂ nanotube arrays to 134 μm in length. *J Phys Chem B* 110(33):16179–16184.
- [39]. Raja KS, Gandhi T, Misra M (2007) Effect of water content of ethylene glycol as electrolyte for synthesis of ordered titania nanotubes. *Electrochem Commun* 9(5):1069–1076.
- [40]. Tsui, L.-k.; Zangari, G., Water content in the anodization electrolyte affects the electrochemical and electronic transport properties of TiO₂ nanotubes:

- a study by electrochemical impedance spectroscopy. *Electrochimica Acta*, 2014, 121, 203-209.
- [41]. Lockman Z, Sreekantan S, Ismail S et al (2010) Influence of anodisation voltage on the dimension of titania nanotubes. *J Alloys Compd* 503(2):359–364.
- [42]. Y. Alivov, M. Pandikunta, S. Nikishin, and Z. Fan, "The anodization voltage influence on the properties of TiO₂ nanotubes grown by electrochemical oxidation," *Nanotechnology*, vol. 20, no. 22, p. 225602, 2009.
- [43]. Allam NK, Grimes CA (2008) Effect of cathode material on the morphology and photoelectrochemical properties of vertically oriented TiO₂ nanotube arrays. *Solar Energy Mater Solar Cells* 92:1468–1475.
- [44]. Sreekantan S, Saharudin KA, Wei LC (2011) Formation of TiO₂ nanotubes via anodization and potential applications for photo-catalysts, biomedical materials, and photoelectrochemical cell. *IOP Conf Series: Mater Sci Eng* 21:012002. doi:10.1088/1757-899X/21/1/012002.
- [45]. P. Roy, S. Berger, P. Schmuki, TiO₂ nanotubes: synthesis and applications, *Angew.Chem. Int. Ed.* 50 (2011) 2904.
- [46]. Chu, S. Z.; Wada, K.; Inoue, S.; Isogai, M.; Yasumori, A. *AdV.Mater.* 2005, 17, 2115-2119.
- [47]. R. V. Chernozem, M. A. Surmeneva, and R. A. Surmenev, "Influence of anodization time and voltage on the parameters of TiO₂ nanotubes," *IOP*

Conference Series: Materials Science and Engineering, vol. 116, Article ID 012025, 2016.

- [48]. Watcharenwong, A., Chanmanee, W., de Tacconi, N.R., Chenthamarakshan, C.R., Kajitvichyanukul, P. and Rajeshwar, K. (2007). Self-organized TiO₂ nanotube arrays by anodization of Ti substrate: Effect of anodization time, voltage and medium composition on oxide morphology and photoelectrochemical response. *J. Mater Res.*, 22(11): 3186–95.
- [49]. Wang J, Lin Z (2009) Anodic formation of ordered TiO₂ nanotube arrays: effects of electrolyte temperature and anodization potential. *J Phys Chem C* 113(10):4026–4030.
- [50]. Sulka GD, Kapusta-Kołodziej J, Brzózka A et al (2013) Anodic growth of TiO₂ nanopore arrays at various temperatures. *Electrochim Acta* 104:526–535.
- [51]. Sulka GD, Kapusta-Kołodziej J, Brzózka A et al (2013) Anodic growth of TiO₂ nanopore arrays at various temperatures. *Electrochim Acta* 104:526–535.
- [52]. Sun KC, Chen YC, Kuo MY et al (2011) Synthesis and characterization of highly ordered TiO₂ nanotube arrays for hydrogen generation via water splitting. *Mater Chem Phys* 129:35–39.
- [53]. Cai Q, Paulose M, Varghese OK et al (2005) The effect of electrolyte composition on the fabrication of self-organized titanium oxide nanotube arrays by anodic oxidation. *J Mater Res* 20(1):230–236.

- [54]. SCAPS Manual
<https://users.elis.ugent.be/ELISgroups/solar/projects/scaps/SCAPS%20manual%20most%20recent.pdf>
- [55]. H.J. Pauwels, G. Vanhoute, Influence of interface states and energy barriers on efficiency of heterojunction solar-cells, *J. Phys. D-Appl. Phys.*, 11 (1978) 649-667.
- [56]. H. Sopha, L. Hromadko, K. Nechvilova, J.M. Macak; Effect of electrolyte age and potential changes on the morphology of TiO₂ nanotubes *J. Electroanal. Chem.*, 759 (2015), pp. 122-128.
- [57]. Vahabzadeh, P.J., Gilani, N., Ebrahimian, P.A.: The effect of the anodization voltage on the geometrical characteristics and photocatalytic activity of TiO₂ nanotube arrays. *Nano Struct Nano Objects* 8, 7–14 (2016).
- [58]. H. Dang, V. P. Singh, S. Guduru, J. Bowie, D. Cambron, "Electro optical characterization of n-CdS nanowires/p-CdTe heterojunction solar cell devices", 2014 IEEE 40th Photovoltaic Specialist Conference (PVSC); IEEE, pp. 1601-1606, 2014.
- [59]. H.M. Dang, Vijay Singh, Suresh Rajaputra, Sai Guduru, Sai Guduru, Jianhao Chen, Bhavananda Nadimpally, "Cadmium sulfide nanowire arrays for window layer applications in solar cells", *Solar Energy Materials and Solar Cells*, 26, 184-191, 2014.
- [60]. V.P. Singh, D.L. Linam, D.W. Dils, J.C. McClure, G.B. Lush, "Electro-optical characterization and modeling of thin film CdS-CdTe heterojunction solar cells", *Solar Energy Materials and Solar Cells*, Vol. 63, pp 445-466, 2000.

[61]. Press Release, First Solar, 26 July 2011.

[62]. Press Release, First Solar, Feb 2016.

VITA

Deepak Kumar was born in Jamshedpur, India. He earned his bachelor's degree in Electronics Engineering in 2013 from Birsa Institute of Technology, Sindri, India. He got enrolled for the Master of Science Program in electrical engineering at the University of Kentucky in Fall 2017. He, during this program, worked as a researcher in the field of nanotechnology on enhancing the performance of nanostructured CdS- CdTe solar cells.

Deepak Kumar